Computermodellering van stentimplantaties in kransslagadervertakkingen

Computer Modelling of Coronary Bifurcation Stenting

Peter Mortier

Promotoren: prof. dr. ir. P. Verdonck, prof. dr. ir. B. Verhegghe
Proefschrift ingediend tot het behalen van de graad van
Doctor in de Ingenieurswetenschappen: Biomedische Ingenieurstechnieken

Vakgroep Civiele Techniek
Voorzitter: prof. dr. ir. J. De Rouck
Faculteit Ingenieurswetenschappen
Academiejaar 2009 - 2010

UNIVERSITEIT GENT

ISBN 978-90-8578-345-9
NUR 954
Wettelijk depot: D/2010/10.500/21

Supervisors:

prof. dr. ir. Pascal Verdonck
prof. dr. ir. Benedict Verhegghe

Examination Committee:

prof. dr. ir. R. Verhoeven (chairman)	Ghent University
prof. dr. ir. P. Segers (secretary)	Ghent University
dr. ir. M. De Beule	Ghent University
prof. dr. ir. J. Degrieck	Ghent University
dr. ir. F. Gijsen	Erasmus MC Rotterdam (NL)
prof. dr. eng. G. Holzapfel	Graz University of Technology (AT)
prof. dr. Y. Taeymans	Ghent University Hospital
prof. dr. ir. P. Verdonck	Ghent University
prof. dr. ir. B. Verhegghe	Ghent University

Research lab:

Biofluid, Tissue and Solid Mechanics for Medical Applications
Institute Biomedical Technology
Ghent University
De Pintelaan 185 - Blok B
B-9000 Gent
Belgium

This research was funded by a BOF (Bijzonder Onderzoeksfonds) grant (01D22606).

Acknowledgements

The most important support, advice, and encouragement is that given at the beginning when the future is uncertain and can only be appreciated in hindsight.
—James Lewis Squire Jr.

Many people have contributed in direct and indirect ways to this work. The list of names that I want to mention is quite long and some people may find this suspicious. But yes, all these people contributed and it's not because I have to mention them, it's because I want to.

Benedict, my appreciation for your work and long-term oriented way of working has grown over the years. The fundamental tools you are creating significantly raised the level of my work. Thanks to your technical expertise and of course, the fact that you always immediately were there whenever I had a problem, I dared to address more challenging questions than I would have done on my own. Pascal, you gave me the freedom to address the topic I wanted to study: the fascinating field of bifurcation stenting. Thank you! To Patrick: I very much appreciated your regular com(pli)ments on my work.

During my PhD, I had the opportunity to travel to many places and to meet numerous interesting scientists, but I will never forget the time I spent in Graz where I had the chance to experience the hospitality of Prof. Gerhard Holzapfel. I had a great time there, also thanks to his co-workers: David, Dimitrios, Thomas and Gerhard.

A special thanks also to the medical doctors who supported this research. In particular, Prof. Yves Taeymans, for providing us with the latest stent samples and angiographic data, the medical doctors from the Cardiovascular Center Aalst, for introducing our research at the European Bifurcation Club.

One of the most exciting parts of my research was the investigation and optimization of a new bifurcation stent. I got this chance thanks to Jan Weber, who saw the possibilities of our research. Jan, thanks for this.

I would like to thank all the former and current bioMMeda-colleagues for the nice PhD-time I had, but some of them deserve a special thanks. Matthieu,

you introduced me into an exciting research field that keeps on fascinating me. Above all, it was a real pleasure to work with you and I hope we can continue doing this for many more years. Thanks mate! I would also like to mention Denis, for the scaled scans and the useful comments, Gianluca, for the interesting discussions and the extremely nice bifurcations, and Sofie, for reminding me to get a coffee around 10 am and for helping me with my basic pyFormex questions.

Mum and dad, you have done everything so that I had the freedom to go in the direction I wanted. I am very grateful for that and will never forget your efforts. Davine, you are a wonderful girlfriend. Thanks for your continuous support, for your understanding, and for just being there. With your positive energy, you make me happy every single day!

Gent, January 2010

Peter

Contents

Dutch Summary **i**

English Summary **vii**

1 Introduction **1**
1.1 Anatomy, physiology and pathology of coronary bifurcations . 2
1.1.1 Healthy coronary bifurcations 2
1.1.2 Bifurcation lesions 5
1.2 Treatment techniques 7
1.2.1 Stent placement 8
1.2.2 Stenting bifurcation lesions 12
1.2.2.1 Provisional stenting 14
1.2.2.2 T stenting 17
1.2.2.3 The crush technique 17
1.2.2.4 Culotte stenting 18
1.2.2.5 V stenting and simultaneous kissing stents technique 19
1.2.2.6 Skirt technique 19
1.2.2.7 Y stenting 19
1.2.2.8 Clinical outcomes 20
1.2.3 Dedicated bifurcation stents 22
1.2.3.1 Antares Coronary Stent System 22
1.2.3.2 Axxess Bifurcation Stent System 24
1.2.3.3 Multi-Link Frontier 25
1.2.3.4 Nile Croco 26
1.2.3.5 Petal 27
1.2.3.6 Sideguard 28
1.2.3.7 SideKick 28
1.2.3.8 Stentys Coronary Bifurcation Stent 29
1.2.3.9 Tryton Side-Branch Stent 30
1.2.3.10 Twin-Rail 31
1.2.3.11 Conclusions 32
1.3 Bifurcation stent research 33

1.3.1 Bench testing 33
1.3.1.1 Bench testing techniques 33
1.3.1.2 Applications 34
1.3.2 Finite element analysis 35
1.3.3 Conclusions 37
1.4 Aim of the doctoral research 38
1.5 Organisation of the dissertation 38

2 Advances in finite element stent modelling 41
2.1 Uniformity of balloon-expandable stent deployment 42
2.1.1 Introduction 42
2.1.2 Materials and methods 43
2.1.2.1 Balloon and stent geometry 43
2.1.2.2 Constitutive models 43
2.1.2.3 Boundary conditions 44
2.1.2.4 Discretization 45
2.1.2.5 Finite element simulations 45
2.1.3 Results and discussion 48
2.1.3.1 Validation of the reference model 48
2.1.3.2 Influence of the balloon length 48
2.1.3.3 Influence of the folding pattern 52
2.1.3.4 Influence of small positioning inaccuracies . . 53
2.1.4 Limitations 53
2.1.5 Conclusions 54
2.2 Automation of pre-processing 55
2.2.1 Introduction 55
2.2.2 Materials and methods 55
2.2.3 Results and discussion 57
2.2.4 Conclusion 61

3 Accuracy of finite element analysis of side branch access during provisional stenting 63
3.1 Introduction 63
3.2 Materials and methods 65
3.2.1 Geometry 65
3.2.2 Constitutive behaviour 66
3.2.3 Simulation details 67
3.2.4 Postprocessing 69
3.2.5 Discretization 69
3.3 Results and discussion 70
3.3.1 Validation of balloon models 70
3.3.2 Side branch access 70
3.3.3 Stent distortion in the MB 72
3.3.4 Study limitations 75
3.4 Conclusion 76

4 Virtual stent insertion in a patient-specific coronary bifurcation 77
4.1 Introduction . . . 77
4.2 Materials and methods . . . 79
4.2.1 Arterial model . . . 79
4.2.1.1 Geometry . . . 79
4.2.1.2 Arterial tissue . . . 79
4.2.1.3 Fiber orientation . . . 82
4.2.2 Stent models . . . 83
4.2.3 Balloon model . . . 84
4.2.4 Numerical simulations . . . 86
4.3 Results and discussion . . . 89
4.3.1 Verification of the implemented arterial model . . . 89
4.3.2 Comparison of the second generation DES . . . 89
4.4 Conclusion . . . 95

5 Geometrical stent analysis 97
5.1 Stent cell size . . . 97
5.1.1 Introduction . . . 97
5.1.2 Materials and methods . . . 98
5.1.2.1 Investigated stents . . . 98
5.1.2.2 Micro-CT . . . 99
5.1.2.3 Cell circumference determination . . . 100
5.1.2.4 Calculation of ostium circumference . . . 100
5.1.3 Results . . . 100
5.1.3.1 Cell circumference . . . 100
5.1.3.2 Ostium circumference . . . 101
5.1.4 Discussion . . . 102
5.1.5 Limitations . . . 106
5.1.6 Conclusion . . . 106
5.2 Strut density . . . 107
5.2.1 Introduction . . . 107
5.2.2 Materials and methods . . . 108
5.2.3 Results and discussion . . . 110
5.2.4 Limitations . . . 112
5.2.5 Conclusions . . . 113

6 Virtual investigation of a novel provisional bifurcation stent system 115
6.1 Introduction . . . 115
6.1.1 Current limitations of provisional stenting . . . 115
6.1.2 Dedicated bifurcation stent design . . . 116
6.1.3 Bifurcation stenting procedure . . . 117
6.1.4 Objectives . . . 118
6.2 Materials and methods . . . 118

6.2.1 Geometrical models 118
6.2.1.1 Stent 118
6.2.1.2 Balloon 118
6.2.1.3 Arterial bifurcation 119
6.2.2 Constitutive models 119
6.2.2.1 Stent 119
6.2.2.2 Balloons 120
6.2.2.3 Arterial wall 120
6.2.3 Discretization 121
6.2.4 Simulation steps 121
6.2.5 Finite element simulations 122
6.2.6 Postprocessing 124
6.3 Validation of the finite element simulations 126
6.3.1 Validation of free balloon expansion 126
6.3.1.1 Non-compliant 72D PEBAX balloon 127
6.3.1.2 Compliant 63D PEBAX balloon 127
6.3.1.3 Non-compliant 72D PEBAX bulge balloon . 128
6.3.2 Validation of free stent expansion 129
6.3.3 In vitro validation of the complete bifurcation stenting procedure 129
6.4 Strut protrusion: compliant versus bulge balloon 129
6.5 Parametric analyses 131
6.5.1 Stent geometry 131
6.5.2 Balloon pressure 132
6.5.3 Balloon size 132
6.5.4 Balloon compliance 133
6.5.5 Impact of vessel anatomy 133
6.5.6 Quantification 133
6.6 Mechanism of strut protrusion 135
6.7 Positioning inaccuracies 135
6.7.1 Impact of balloon misplacement 135
6.7.2 Impact of stent misplacement 136
6.8 Limitations 137
6.9 Conclusions 137

7 Stent design guidelines and final remarks 139
7.1 Conclusion 139
7.2 Future work 141

Bibliography 156

Publications 175

Abbreviations and Symbols 177

Samenvatting

Hoofdstuk 1: Introductie

De voornaamste doodsoorzaak in Westerse landen zijn de hart- en vaatziekten. Ze veroorzaken jaarlijks 48% van de sterfgevallen in Europa [1]. Vernauwingen (stenosen) van de coronaire slagaders of kransslagaders die het hart van zuurstofrijk bloed voorzien liggen aan de basis van een belangrijk deel van deze sterfgevallen. Deze vernauwingen zijn een ophoping van lipoïden, cholesterol,... Een uitgesproken vernauwing van een kransslagader kan voor zuurstoftekort zorgen in een deel van het hart - stroomafwaarts van de stenose - met een hartaanval als gevolg. Het heropenen van deze stenosen in één enkel bloedvat is heel wat vereenvoudigd door de ontwikkeling van stents (cilindrische, meestal metalen structuren die in de arterie worden ingebracht, ook soms hartveertje genoemd). Via een kleine incisie in de lies of in de arm wordt de stent met een katheter ter plaatse gebracht en ontplooid via het opblazen van een ballon. De stent duwt de vernauwing open en de bloedtoevoer wordt hersteld. Deze minimaal invasieve ingreep vormt in veel gevallen een zeer degelijk alternatief voor de invasieve overbruggings- of bypass operaties, waarbij een vaatomlegging het afgesloten of vernauwd gedeelte van de arterie overbrugt. In 2004 werden in Europa dan ook meer dan 770000 stents geplaatst [2].

De eerste generatie stents gaf in 20-30% van de gevallen aanleiding tot hervernauwing of restenosis van het gestente bloedvat. Door de introductie van stents die medicijnen afgeven aan de vaatwand werd het optreden van hervernauwing gereduceerd tot minder dan 10% voor niet-vertakte bloedvaten.

Men heeft echter vastgesteld dat vaatwandvernauwingen hoofdzakelijk voorkomen op specifieke plaatsen, namelijk ter hoogte van vertakkingen (bifurcaties) en bochten [3] en dit wordt onder andere in verband gebracht met de daar voorkomende wijzigingen in de bloedstroming. Ondanks de behoorlijke resultaten van de stenting procedures voor niet-vertakte bloedvaten blijft het stenten van coronaire bifurcaties een belangrijk klinisch probleem. Restenosis treedt op in 15% van de gevallen [4] en het mogelijks optreden

van bloedklonters (thrombose) is een bijkomend probleem. Er zijn reeds heel wat technieken bedacht waarbij stents ontworpen voor niet-vertakte bloedvaten worden geplaatst ter hoogte van bifurcaties (bijvoorbeeld T-stenting, V-stenting, culotte stenting,...) maar al deze technieken hebben belangrijke beperkingen en zijn vaak complex om toe te passen in de klinische praktijk [5]. De kostprijs van deze technieken loopt ook vaak erg hoog op aangezien meerdere stents en ballonnen noodzakelijk zijn.

Er is duidelijk nood aan stents, specifiek ontworpen voor bifurcaties, die de complexiteit van deze ingrepen reduceert. Aangezien de markt voor dergelijke producten aanzienlijk is, gaan dan ook heel wat bedrijven op zoek naar de ideale 'bifurcatie-stent'. Het gebruik van deze producten is tot op heden beperkt. Heel veel van deze producten zitten nog in een ontwikkelingsfase en enkele van de producten die reeds op de markt zijn gekomen hadden een beperkte gebruiksvriendelijkheid.

De traditionele aanpak om deze technieken en producten te bestuderen en te optimaliseren bestaat erin stents te implanteren in vertakte silicone buisjes en de optredende stentvervormingen daarna te visualiseren met behulp van micro-CT (Computed Tomography) [6]. Op deze manier zijn reeds heel wat interessante studies uitgevoerd, maar deze aanpak is tijdrovend en vereist het gebruik van zeer veel (dure) stents. Bovendien laat deze onderzoeksmethode enkel toe om reeds geproduceerde stents te bestuderen.

Tijdens dit doctoraatsonderzoek werd naast de traditionele experimentele aanpak ook gebruik gemaakt van innovatieve eindige elementen simulaties om de problematiek van bifurcatie stenting te bestuderen. Deze techniek levert extra informatie ten opzichte van in-vitro tests, zoals spanningen en rekken in de stent en de bloedvatwand. Bovendien laten deze simulaties toe heel wat parameters te bestuderen vooraleer over te gaan tot fabricatie. Deze aanpak heeft dan ook het potentieel om innovatieve stents te ontwerpen en de tijd om het product op de markt te brengen drastisch te reduceren.

Het doctoraatsonderzoek had tot doel om:

- inzicht te krijgen in de beperkingen van de huidige stents en technieken voor het behandelen van vernauwingen ter hoogte van coronaire bifurcaties.
- inzicht te verwerven in de nodige ontwerpparameters voor een ideale bifurcatie stent.
- richtlijnen te verstrekken aan artsen omtrent stentselectie.
- simulatiestrategieën te ontwikkelen die toelaten om nieuwe stents te onderzoeken en te optimaliseren.

Hoofdstuk 2: Innovatieve eindige elementen simulaties van stents

Het is van groot belang realistische basismodellen te ontwikkelen van ballonopblaasbare stents vooraleer over te gaan tot het simuleren van stentimplantaties ter hoogte van bifurcaties. Daarom is in eerste instantie een model ontwikkeld dat toelaat om de vrije stentexpansie te bestuderen. Dit model toont een zeer goede overeenkomst met zowel kwalitatieve als kwantitatieve experimentele data en vormt dus een goede basis om het mechanische gedrag van ballonopblaasbare stents te bestuderen en te optimaliseren. Een huidige beperking van deze stents is dat ze niet altijd uniform ontplooien, dit zowel in de lengterichting als in de omtreksrichting. Nochtans is een uniforme expansie gewenst aangezien dit de beschadiging van endotheelcellen reduceert en leidt tot een uniforme afgifte van medicijn. De resultaten van een parameterstudie op basis van het gevalideerde model tonen aan dat zowel de ballonlengte als de opplooivorm van de ballon een grote impact hebben op de uniformiteit van de stentexpansie. Een verminderde ballonlengte leidt tot een uniformere expansie in de lengterichting, terwijl het verhogen van het aantal plooien in de opgevouwen ballon de uniformiteit in de omtreksrichting positief beïnvloedt.

Naast het ontwikkelen van accurate computermodellen van stents is ook het versnellen en automatiseren van de opbouw van deze modellen van belang om vele verschillende stents en implantatieprocedures efficiënt te kunnen onderzoeken. Zo is het bijvoorbeeld tijdrovend om een computermodel van een stent op te bouwen op basis van een beschikbaar exemplaar van deze stent. De typische procedure om dit te doen bevat een aantal tijdsrovende stappen, zoals het opmeten van de exacte stent- en strutafmetingen en het natekenen van de opgemeten geometrie met CAD (Computer Aided Design) software. In dit hoofdstuk wordt een alternatieve methode voorgesteld die toelaat om op basis van micro-CT beelden op een quasi automatische manier over te gaan naar een stentmodel dat gebruikt kan worden voor eindige elementen simulaties. De efficiëntie en nauwkeurigheid van de ontwikkelde procedure wordt aangetoond voor de Multi-Link Vision stent.

Hoofdstuk 3: Eindige elementen analyse van de toegang tot de zijtak na het plaatsen van een stent in de hoofdtak

Dit hoofdstuk bespreekt een veel toegepaste techniek voor het behandelen van vernauwingen ter hoogte van coronaire bifurcaties, namelijk het plaatsen van een stent in de hoofdtak, gevolgd door het opblazen van een ballon die zich gedeeltelijk in de hoofd- en zijtak bevindt (en dus doorheen de zijkant van de reeds ontplooide stent gaat). Het opblazen van deze ballon heeft tot doel de toegang tot de zijtak te verbeteren aangezien bepaalde struts van de stent de stroming naar de zijtak belemmeren. Experimenteel

onderzoek heeft reeds aangetoond dat deze balloninflatie inderdaad positief is voor de toegang naar de zijtak, maar dat deze procedure soms leidt tot een verslechterde situatie in de hoofdtak.

Deze studie had enerzijds tot doel om de haalbaarheid na te gaan om met behulp van computersimulaties de optredende stentvervorming tijdens een dergelijke complexe procedure realistisch te gaan voorspellen. De goede overeenkomst van de numerieke resultaten met reeds gepubliceerde experimentele observaties toont duidelijk aan dat computersimulaties een rol kunnen spelen bij het bestuderen van bifurcatie stenting. Anderzijds werd ook de impact van stent- of ballonkeuze bestudeerd. Het opblazen van een grotere ballon doorheen de zijkant van een stent leidt duidelijk tot een betere toegang tot de zijtak. Daarnaast werd ook vastgesteld het vervormingspatroon van de stent sterk afhankelijk is van het stenttype. Deze ingreep veroorzaakte bijvoorbeeld slechts voor één van de twee onderzochte stents een obstructie in de hoofdtak.

Hoofdstuk 4: Virtuele stentimplantatie in een patiënt-specifieke coronaire bifurcatie

De studie beschreven in dit hoofdstuk vergelijkt het mechanisch gedrag van drie verschillende stents. De stents werden virtueel geïmplanteerd in een gebogen hoofdtak van een bifurcatie, waarvan de geometrie gebaseerd is op patiënt-specifieke klinische beelden. Het beschrijven van het mechanisch gedrag van de drie verschillende arteriële lagen (intima, media en adventitia) vormt een belangrijk onderdeel van dit hoofdstuk. Een bestaand model dat toelaat om het anisotroop gedrag van elk van deze lagen te beschrijven werd geïmplementeerd in het eindige elementen pakket Abaqus en de correctheid van de implementatie werd nagegaan, door het virtuele mechanische gedrag te vergelijken met experimentele en analytische data. Het gebruik van anisotrope materialen vereist het vastleggen van locale materiaaloriëntaties. Daarom wordt ook een nieuwe techniek voorgesteld om de vezeloriëntatie ter hoogte van de bifurcatie te definiëren. Ook op het gebied van stentmodellering werd progressie gemaakt. Door de gekromde vorm van het bloedvat was het bijvoorbeeld noodzakelijk om een innovatieve simulatiestrategie te ontwikkelen waarbij de stent ingebracht wordt door middel van een voerdraad, net zoals in realiteit.

Uit de resultaten blijkt dat alle stents leiden tot een gelijkaardige rechttrekking van het bloedvat, maar dat de veroorzaakte spanningen in de bloedvatwand daarentegen sterk afhankelijk zijn van het stenttype. Door gebruik te maken van parametrische modellering worden ook enkele stentvarianten voorgesteld die de spanningen in de bloedvatwand beperken. Dit toont duidelijk de kracht van deze computersimulaties. Verschillende ontwerpvarianten kunnen worden bestudeerd vooraleer over te gaan tot fabricatie.

Hoofdstuk 5: Geometrische analyse van stents

Cardiologen worden overstelpt met het aanbod aan verschillende stenttypes. Het is dan ook belangrijk deze verschillende stents op basis van objectieve criteria te vergelijken, zodat artsen een weloverwogen keuze kunnen maken rekening houdend met het te behandelen letsel. Bij het plaatsen van een stent ter hoogte van een bifurcatie is de grootte van de openingen in de stent van groot belang. Een stent geplaatst in de hoofdtak vormt een obstructie voor de stroming naar de zijtak. Daarom wordt veelal een ballon doorheen één van deze openingen opgeblazen met als doel deze opening zo groot mogelijk te maken en alle struts tegen de bloedvatwand aan te drukken.

In dit hoofdstuk worden de stentopeningen van vijf verschillende stents op een nieuwe manier opgemeten en geanalyseerd. Op basis van micro-CT beelden worden de driedimensionale (3D) stentgeometrieën virtueel gereconstrueerd, wat resulteert in een oppervlaktebeschrijving van de 3D objecten met driehoeken. Deze stentmodellen worden verder geanalyseerd met behulp van het softwarepakket pyFormex. Na een aantal operaties, zoals bijvoorbeeld het ontrollen van de cilindrische geometrie in een vlak, wordt de planaire omtrek van één stentopening afgezonderd en opgemeten. Uit de resultaten blijkt dat de omtrek (of dus de maximale grootte) van de openingen van de onderzochte stents sterk verschilt.

Het combineren van de informatie over de grootte van de stentopeningen met anatomische informatie (diameter hoofdtak, diameter zijtak, bifurcatiehoek) laat toe om vooraf te gaan voorspellen welke stents geschikt zijn voor een bepaalde bifurcatie. Het plaatsen van een stent waarvan de omtrek van de openingen kleiner is dan de omtrek van de opening naar de zijtak zal bijna altijd resulteren in een obstructie van de stroming naar de zijtak.

Hoofdstuk 6: Virtuele optimalisatie van een nieuwe bifurcatie stent

In hoofdstuk 6 worden eindige elementen simulaties gebruikt om de haalbaarheid van een nieuwe specifieke bifurcatiestent en een aangepaste procedure te onderzoeken. De stent is bedoeld om in de hoofdtak geïmplanteerd te worden en heeft een specifiek strutpatroon in het centrale gedeelte, dat toelaat om ter hoogte van de bifurcatie een grotere stentdiameter te bereiken. Dit is van belang om een gedeeltelijke ondersteuning van de ingang van de zijtak te bekomen. De aangepaste procedure bestaat uit een postdilatatie van de reeds geëxpandeerde stent met een specifieke ballon (bijvoorbeeld een 'bulge' of een compliante ballon). Deze postdilatatie heeft tot doel om:

- de stentopeningen ter hoogte van de toegang naar de zijtak gedeeltelijk

open te duwen zodat het inbrengen van een ballonkatheter in de zijtak eenvoudiger wordt.

- reeds voor een gedeeltelijke ondersteuning van de ingang van de zijtak te zorgen.

In een eerste deel van deze studie worden de ballonmodellen en de vrije stentexpansie gevalideerd aan de hand van experimentele data. Daarna worden deze gevalideerde modellen gebruikt om de volledige bifurcatie stenting procedure te simuleren. De nauwkeurigheid van de gesimuleerde vervormingen na de postdilatatie wordt geverifieerd met een in-vitro experiment waarbij een identieke procedure wordt gevolgd.

Op basis van het eindige elementen model wordt de impact van een aantal parameters bestudeerd (ballondruk, balloongrootte, compliantie, stentontwerp en bifurcatiegeometrie) op de finale vervorming van de struts. Uit deze numerieke resultaten blijkt welke parameters een grote impact hebben op de stentvervorming en deze inzichten laten dan ook toe om het stentontwerp en de procedure verder te optimaliseren.

Hoofdstuk 7: Richtlijnen voor stentontwerp en finale opmerkingen

Het finale hoofdstuk geeft een overzicht van de voornaamste bevindingen en bevat enkele richtlijnen omtrent stentontwerp en stentselectie. Daarnaast worden ook enkele suggesties voor verder onderzoek geformuleerd.

Summary

Chapter 1: Introduction

Cardiovascular disease is the most common cause of death in Western countries, accounting for 48% of all deaths in Europe [1]. One of the most important cardiovascular diseases is atherosclerosis, which often leads to narrowed (or stenosed) arteries that obstruct the flow of oxygen rich blood. In the case of coronary arteries, this may limit the oxygen delivery to the heart muscle and can lead to a heart attack. The blood flow through these narrowed arteries is often restored by inserting scaffolding structures, named stents. These small tube-like devices are mounted on the end of a catheter that is inserted into the arterial tree through a small incision. After positioning the stent in the narrowed artery, it is deployed by inflating a balloon. The deformed stent is left in place to keep the artery open and to restore the blood flow. Using stents to treat stenosed arteries is much less invasive as compared to the more traditional bypass surgery, where an alternative conduit is used to restore the blood flow to the downstream tissue. It is therefore not surprising that European physicians used more than 770000 stents in 2004 [2].

The first stent generation was associated with 20-30% in-stent restenosis rates (i.e. a re-narrowing of the stented vessel). The introduction of drug-eluting stents further improved the outcome and the occurrence of restenosis was reduced to less than 10% for unbranched vessels.

There is a tendency for atherosclerosis to develop at specific arterial sites such as bifurcations and curvatures [3] and this has been related to the specific blood flow patterns at those locations. Even with drug-eluting stents, the treatment of bifurcation lesions remains a clinical challenge for interventional cardiologists, due to the technical complexity and high re-intervention rate. Restenosis occurs in 15% of the cases [4] and in addition, bifurcation stenting is associated with an increased thrombosis risk. Many different bifurcation stenting techniques have been proposed with various levels of complexity (e.g. T-stenting, V-stenting, culotte stenting,...) and each of them having one or more limitations [5]. The cost of these interventions

can be very high as most techniques require the use of multiple stents and balloons.

There is a clear need for user-friendly dedicated bifurcation stents which further improve the current outcomes but that also reduce the technical difficulty. The market for such dedicated products is considerable. This attracts the attention of large medical device companies but also leads to a number of start-ups focusing on this niche market. However, the use of these dedicated products has been rather limited. Many of these products are currently undergoing clinical trials and some of the products that have been approved had a limited user-friendliness.

The previously mentioned bifurcation stenting techniques and dedicated devices are usually investigated and optimized by deploying the stents in bifurcated silicone tubes (in-vitro testing). The resulting stent deformations are then visualized and analysed by using micro-CT (Computed Tomography) [6]. Many interesting results have been obtained in this way. However, this experimental approach has a number of disadvantages. It is time-consuming, expensive and requires many stent samples. Furthermore, this approach only allows to investigate stents that have been manufactured.

During this thesis, innovative finite element analysis techniques have been developed and used to study the complex problem of bifurcation stenting. This approach can be used to study stresses and strains and allows to gain insight in products that are difficult to test experimentally. In addition, this approach allows to study several 'What if?' scenarios addressing different materials, geometries and loading conditions before devices are actually manufactured. Therefore, this technique does not only offer a tool to investigate and compare currently used stents and stenting techniques, but also to develop new stents where it has the potential to reduce the time-to-market.

The objective of this thesis was to develop and use advanced computational methods:

- to gain insights in the shortcomings of current stents and stenting techniques.
- to define optimal design parameters for a bifurcation stent.
- to provide guidelines to interventional cardiologists regarding stent selection.
- to virtually investigate and design new stents.

Chapter 2: Advances in finite element stent modelling

A first step to study the field of bifurcation stenting using finite element analysis is to develop validated models to study balloon-expandable stents.

Therefore, we first developed a model to investigate the free stent expansion. This model serves as a solid basis to study and optimize the mechanical behaviour of balloon-expandable stents as the numerical results correspond very well with both qualitative and quantitative experimental data. A limitation of many balloon-expandable stents is that they often deploy in a non-uniform way, both in longitudinal and in circumferential direction. A uniform expansion is preferred as this reduces the endothelial damage and leads to a more uniform drug delivery in case of drug eluting stents. Based on the validated model, a parametric study has been conducted and the results show that both the balloon length and the folding pattern have an enormous impact on the uniformity of the expansion. A reduced balloon length leads to a more uniform deployment in longitudinal direction, while an increased number of balloon folds positively influences the uniformity in circumferential direction.

Besides the development of accurate computer models to study stents, it is also crucial to speed up and automate the generation of these stent models in order to efficiently investigate many different stents and implantation techniques. For example, creating a stent model based on an available stent sample can be time-consuming. The traditional approach to do this involves a number of time-consuming steps, such as the accurate determination of the stent and strut dimensions and the generation of the CAD (Computer Aided Design) model corresponding with the stent. In this chapter, an alternative method is being presented which allows to generate finite element stent models in a semi-automatic way starting from micro-CT images of the stent. The efficiency and accuracy of the developed procedure is illustrated for the Multi-Link Vision stent.

Chapter 3: Finite element analysis of side branch access during provisional stenting

In this chapter, one of the currently applied techniques is analysed (i.e. provisional stenting) which involves the implantation of a stent in the main branch, followed by subsequent inflation of a balloon (which is positioned in both the main and the side branch) through the side of the stent. The second balloon inflation is performed with the intention of improving the side branch patency by pushing the obstructing struts against the vessel wall. Experimental research has demonstrated that such inflation indeed has a positive effect on the side branch access, but may lead to floating struts in the main branch lumen.

A first objective of this study was to investigate the feasibility of using computer simulations to accurately study the stent deformations during a complex procedure as such provisional stenting. The good correspondence between the numerical results and previously published experimental ob-

servations clearly show that computer simulations can play a role during the investigation of bifurcation stenting techniques. The second aim of this study was to assess the impact of the balloon size and stent type. The inflation of a larger balloon through the side of the main branch stent clearly results in a better side branch access, but may result in overdilation. Furthermore, it was also observed that different stent types may lead to totally different deformations. For example, for one of the two investigated stents, this procedure resulted in an obstruction within the main branch.

Chapter 4: Virtual stent insertion in a patient-specific coronary bifurcation

The study described in this chapter investigates and compares three different second generation drug-eluting stents when being implanted in the curved main branch of a coronary bifurcation. The aim is to provide better insights into the related changes of the mechanical environment. The three-dimensional bifurcation model is based on patient-specific angiographic data that accurately reproduce the in vivo curvatures of the vessel segments. The layered structure of the arterial wall and the anisotropic mechanical behavior of each arterial layer (intima, media and adventitia) are taken into account by using an existing advanced constitutive model that was implemented as a user-defined material for Abaqus. The accuracy of the implementation is verified by comparing the virtual mechanical behaviour with experimental and analytical data. The use of anisotropic materials requires a proper definition of the local material orientations. Therefore, a novel algorithm has been developed to automatically define the fiber orientations. In addition, an innovative simulation strategy considering the insertion of a folded balloon catheter over a guide wire is proposed in order to position the stents within the curved vessel.

Analysis of the results reveals that all stents lead to more or less the same amount of vessel straightening after implantation, but the resulting distributions of the wall stresses are strongly dependent on the stent design. Using a parametric modeling approach, two design modifications, which reduce the predicted maximum values of the wall stress, are proposed and analyzed. This illustrates the added value of using computer simulations during the design phase. Many design variants can be analysed without having to manufacture every design iteration.

Chapter 5: Geometrical stent analysis

Interventional cardiologists are being overwhelmed by the large number of available stents offered by various medical device companies. Hence, it is extremely important to provide objective comparisons of the properties

(mechanical, geometrical, etc.) of these stents in order to allow physicians to select appropriate devices for a particular stenotic lesion. In case of bifurcation lesions, one important stent parameter is the size of the openings (i.e. cell size). A stent positioned in the main vessel often obstructs the blood flow into the side branch. Therefore, such implantation is often followed by a balloon dilation through the side of the stent with the aim of pushing all struts against the vessel wall by increasing the opening between the struts.

In this chapter, the stent cells of five different stents are being measured and analysed using an innovative technique. Three-dimensional (3D) reconstructions of the stent geometries are being generated based on micro-CT images, resulting in a triangulated surface description of the 3D objects. These stent models are further processed and analysed using the pyFormex software. One of the operations which is performed on the stent geometry consists of the unraveling of the cylindrical stent geometry into a planar structure. Finally, a line respresenting a planar stent cell is extracted and its circumference is measured. The results show a substantial variation of the cell size of the different investigated stents.

Combining the cell size data with anatomical information (main branch diameter, side branch diameter and bifurcation angle) shows which stents should preferably be used for which bifurcations, as these stents have cells that can be sufficiently enlarged by dilating through the side. Implanting a stent with a cell circumference which is smaller than the ostium circumference will almost inevitably result in a suboptimal deployment and obstructing struts.

Chapter 6: Virtual investigation of a novel provisional bifurcation stent system

Besides using the finite element models to better understand the mechanics of currently available stents, they can also be incorporated in the design process of new devices to perform virtual prototyping and design optimization. In chapter 6, computer simulations are being used to investigate the feasibility of a new dedicated bifurcation stent and a modified procedure for provisional stenting. The stent is intended for the main branch and has a modified strut pattern in the central stent region, which allows the stent to reach a larger diameter at the location of the bifurcation. This is important to provide partial scaffolding at the side branch ostium. The modified procedure consists of a postdilation with a dedicated balloon within the already expanded main branch stent (for example, a bulge or a compliant balloon). This postdilation is performed with the aim of:

- opening the stent cells obstructing the side branch access in order to facilitate the insertion of a balloon catheter into the side branch.

- causing strut protrusion into the side branch to provide partial ostial scaffolding.

The first part of this study involves the validation of the different balloon models and of the free stent expansion using experimental compliance data. These validated models are then used to simulate the complete bifurcation stenting procedure. An in-vitro experiment has been performed to verfiy the accuracy of the predicted deformations after the postdilation.

Based on the finite element model, the impact of a number of device and procedural parameters (such as balloon pressure, balloon compliance, balloon size, stent design, bifurcation geometry) on the final strut deformation has been examined. These results provide new insights and allow to further optimize the stent design and the proposed procedure.

Chapter 7: Stent design guidelines and final remarks

The final chapter gives an overview of the major findings of the research and contains some guidelines regarding stent design and selection. In addition, some suggestions for further research are included.

Chapter 1

Introduction

ALL oxygen rich blood leaves the heart through the aortic valve into the aorta, the largest blood vessel in our body. From there, it is distributed all over the body and supplies every body part (e.g., muscles, organs,...) with oxygen. This is only possible by the bifurcated nature of the arterial system. After leaving the heart, the aorta branches into smaller arteries, which eventually divide into arterioles. Similarly these arterioles branch into minuscule capillaries where the exchange of oxygen and other substances takes place with the surrounding tissue. This bifurcated organisation is often referred to as the vascular tree.

The coronary circulation, a crucial part of this vascular tree, provides oxygen rich blood to the heart. Obstructions of the blood flow at the largest coronary bifurcations result in suboptimal functioning of a considerable part of the heart muscle and are difficult to treat. Analysis of the treatment of this challenging subset of bifurcation lesions by using advanced computational methods defines the main topic of this thesis.

This chapter begins with a description of both the healthy and the diseased anatomy of arterial bifurcations, followed by a description of procedures and dedicated devices applied to treat coronary bifurcation lesions. The third part of this introduction consists of a brief overview of research methods which are available to study and to optimize the current coronary bifurcation treatment procedures. Finally the aim of the doctoral research is formulated and the organisation of the dissertation is clarified.

1.1 Anatomy, physiology and pathology of coronary bifurcations

1.1.1 Healthy coronary bifurcations

In general, there are two main coronary arteries, the left coronary artery (LCA) and the right coronary artery (RCA), which originate from the root of the aorta. The part of the LCA between the aorta and the first bifurcation is known as the left main artery (LM). The left main bifurcates into the left anterior descending artery (LAD) and the left circumflex artery (LCX). The RCA, LCA, LM, LAD and LCX are the most important coronary arteries. In some rare cases, people have only one coronary artery or sometimes they have a third one, the posterior descending artery. For healthy people with a balanced distribution of the coronary arteries[1], the diameters of the proximal segments of the RCA, LM, LAD and LCX are respectively 3.0±0.5, 4.4±0.4, 3.6±0.4 and 3.4±0.5 mm according to the data published by Dodge et al. [7]. A schematic overview of the main coronary arteries is shown in Fig. 1.1.

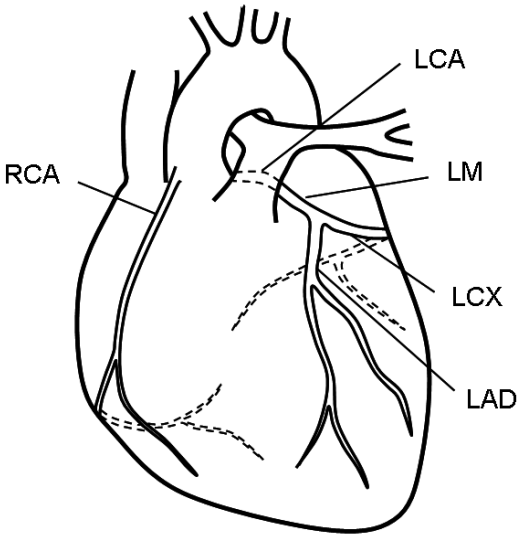

Figure 1.1: Schematic overview of the main coronary arteries (RCA = right coronary artery, LCA = left coronary artery, LM = left main artery, LCX = left circumflex artery, LAD = left anterior descending artery).

The coronary tree contains many bifurcations (and sometimes trifurcations) in order to supply the complete heart muscle with oxygen and nutrition. A

[1] A balanced distribution means that nor the LCA, nor the RCA is dominant.

bifurcation typically consists of a proximal main branch (PMB), a distal main branch (DMB) and a side branch (SB). The SB ostium is the opening in the main branch (MB) that leads to the SB and the carina is the point where the two branches split. In this work the bifurcation angle is defined as the angle between the SB and the DMB axes[2]. Using this definition, Kaplan et al. [9] reported angle values of 56.6±21.7° based on 80 coronary bifurcations. All main anatomical bifurcation features are indicated in Fig. 1.2.

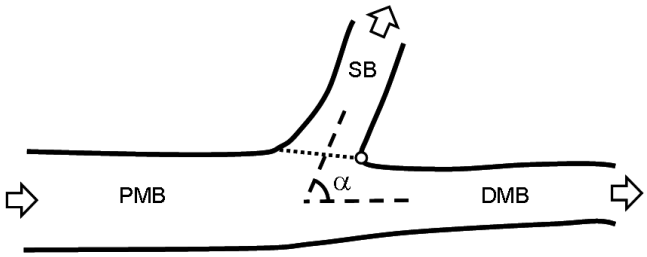

Figure 1.2: Schematic representation of a coronary bifurcation with inflow in the proximal main branch (PMB) and outflow at the distal main branch (DMB) and the side branch (SB). α indicates the bifurcation angle. The SB ostium and the carina are represented by a dotted line and a small circle respectively.

Physiological systems such as the coronary tree display a high degree of organization, for example the stepwise decrease of the vessel diameter up to the capillary level (i.e. geometrical tapering). There have been numerous attempts to explain and to quantify the design of the vascular tree. These theoretical models provide relationships between the diameters of the PMB, the DMB and the SB. For example, Murray [10] derived an optimal condition for vascular bifurcations based on the principle of minimum work that is known as Murray's law. It states that the cube of the diameter of the PMB (D_{PMB}) equals the sum of the cubes of the diameters of the DMB (D_{DMB}) and the SB (D_{SB}):

$$D_{PMB}^3 = D_{DMB}^3 + D_{SB}^3 \tag{1.1}$$

Recently, Finet et al. [11] proposed a linear relationship between the different vessel diameters for coronary bifurcations which is easier to use in clinical practice:

$$D_{PMB} = 0.678 * (D_{DMB} + D_{SB}) \tag{1.2}$$

[2] The bifurcation angle is sometimes defined as the angle between the PMB axis and the SB axis [8].

The ratio 0.678 is based on angiographic data and is accurate for all coronary arteries. The authors also applied Murray's law to their data and observed that the predicted D_{PMB} using formula 1.1 underestimated the actual D_{PMB} with 5%. The fact that Murray's law predicts a smaller D_{PMB} than the relation proposed by Finet et al. is reflected in Fig. 1.3, where the distal branch diameters (D_{DMB} and D_{SB}) are assumed to be equal. With this assumption, both relations are linear and the predicted values for D_{PMB} are always 7% higher using the relation proposed by Finet et al.

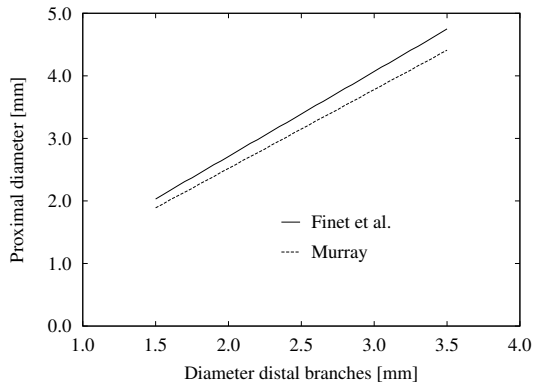

Figure 1.3: Comparison of the relation between bifurcation vessel diameters proposed by Murray [10] and Finet et al. [11] when assuming equal distal branch diameters.

Healthy arteries typically consist of three distinct layers, the tunica intima (the innermost layer), the tunica media (the middle layer) and the tunica adventitia (the outermost layer), as depicted in Fig. 1.4. In young arteries, the intima is a single layer of endothelial cells resting on a basement membrane of connective tissue. However, ex vivo testing of non-stenotic aged arteries revealed the load bearing capacity of the intima and its considerable mean thickness of 27% with respect to the total wall thickness [12]. The occurrence of such a substantial intimal layer in aged arteries is the result of diffuse intimal hyperplasia, introduced by a non-atherosclerotic process [13]. The media is built up of a three-dimensional network of bundles of collagen fibrils, elastin and smooth muscle cells. The fibers have a helicoidal organization with a small pitch angle (20.6±5.5° according to [12]) resulting in a high circumferential strength. The adventitia mainly consists of fibroblasts and collagen fibers embedded in a ground-matrix and forms a protective layer around the arteries [14].

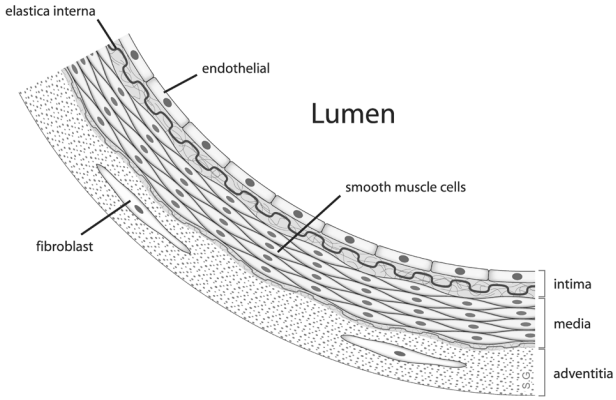

Figure 1.4: Layered structure of young and healthy arteries [15].

1.1.2 Bifurcation lesions

Cardiovascular disease causes nearly half of all deaths in Europe (48%) [1]. Atherosclerosis is one important type of these diseases and is an inflammatory pathology which affects blood vessels. Whether endothial denudation or dysfunction initializes the inflammatory process is still a matter of debate. Such endothelial dysfunction or denudation increases the adhesiveness of the endothelium and its permeability and can be caused by hypertension, smoking, diabetes and combinations of these or other factors. The higher permeability leads to an accumulation of low density lipoproteins (LDL) between the intimal and medial layer. After oxidation of this LDL, monocytes migrate into the vessel wall and differentiate into macrophages, which then ingest the oxidized LDL and modify to foam cells. Subsequently, smooth muscle cells migrate to the inflammation site and a fibrotic collagen cap develops around the plaque. These processes thicken the arterial wall, which compensates by gradual dilation, so that the lumen remains unaltered. Continued inflammation leads to the intrusion of the lesion into the lumen. Such a narrowing of the lumen, called a stenosis, may reduce the supply of oxygen rich blood to downstream tissues [3].

There is a tendency for atherosclerosis to develop at specific arterial sites such as bifurcations and curvatures. At these locations, there are some regions where the blood flow is slow and changes direction during the cardiac cycle, resulting in a weak net hemodynamic shear stress (see Fig. 1.5). Such flow conditions with shear stress values below 1 Pa alter the expression of genes on the endothelial layer, making these arterial regions prone to atherosclerotic lesions, while normal arterial shear stress levels above 1 Pa

result in an atheroprotective gene expression profile [16]. Regions subjected to too high shear stress values ($> 7\,\mathrm{Pa}$) such as cardiac valves have an increased thrombotic risk [16].

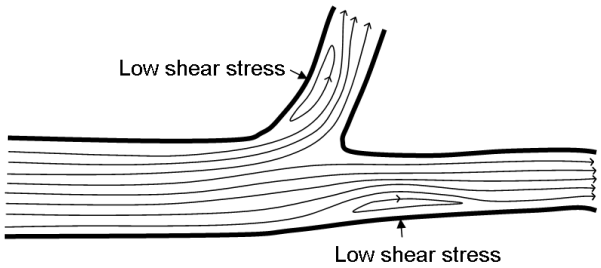

Figure 1.5: Schematic illustration of the blood flow in a bifurcation.

Coronary bifurcation lesions occur in many different types and a proper classification is required to define these lesions and to compare different treatment techniques. Medina et al. [17] proposed a simple and clear classification method to distinguish different lesions depending on the distribution of the plaque as depicted in Fig. 1.6. The method consists of giving a binary value (1 or 0) to each of the bifurcation vessels segments respecting the following sequence: PMB, DMB and SB. A value of 1 is assigned when the segment contains a narrowed section. All possible lesion types are shown in Fig. 1.6.

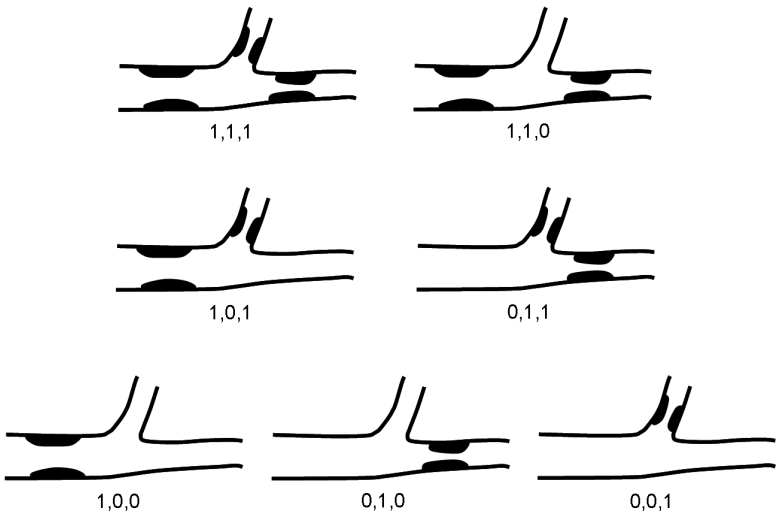

Figure 1.6: Medina classification for coronary bifurcation lesions.

The European Bifurcation Club suggests to use this Medina classification when describing coronary bifurcation lesions, although it only gives information related to the location of the plaque [18]. Other parameters such as bifurcation angle, lesion length and severity of the stenosis are not incorporated. However, assessment of these parameters requires a quantitative evaluation of coronary angiography data which is still operator dependent. Advanced software allowing automatic extraction of these parameters may help at this point (e.g. CAAS 3D quantitative coronary analysis (QCA) software, Pie Medical).

1.2 Treatment techniques

A severe stenosis in a coronary artery decreases the supply of oxygen rich blood to the heart muscle (myocardium) and often results in chest pain (angina pectoris) or a heart attack (myocardial infarction). Treatment can include weight reduction, cholesterol reduction, change in lifestyle, as well as control of high blood pressure. Some individuals, however, will require invasive treatment such as coronary artery bypass surgery, balloon angioplasty or stent placement. An important question is of course: Which stenoses are severe and should be treated? It has been shown that neither visual assessment of an angiogram by experienced interventional cardiologists nor quantitative coronary angiography can accurately predict the significance of moderate narrowings [19]. Therefore, many lesions are treated without definite evidence that that particular stenosis is causing the symptons. Fractional flow reserve (FFR) has been proposed as an index to assess the functional severity of coronary stenoses and is calculated from pressure measurements. More specifically, the FFR is calculated as the ratio of the mean distal intracoronary pressure measured by a pressure-monitoring guide wire to the mean arterial pressure measured by the coronary catheter [20, 21]. A threshold value for the FFR of 0.75 is often used [21].

Coronary artery bypass surgery involves the creation of one or more alternative conduits to bypass the obstruction(s) in the coronary tree and was performed for the first time in 1960 [22]. The internal mammary artery is often used to construct the bypass, but alternatively, a vein from the leg (saphenous vein) or an artery from the forearm (radial artery) can be taken. This procedure often requires the opening of the chest via a sternotomy (i.e. an incision in the sternum to allow access to the heart) which makes the procedure highly invasive for the patient.

In 1977, a less invasive alternative called angioplasty was introduced by Dr. Gruentzig. During a first step of this minimally invasive procedure, a catheter with a tightly folded balloon at the distal end is mounted over a guide wire that was already inserted through a small incision in the femoral, radial or brachial artery. Subsequently, the balloon catheter is advanced to

the narrowed vessel section using radiopaque markers and inflated at high pressure. This results in a stretched (or partially dissected) vessel wall and in an enlarged lumen. After deflating the balloon, part of the lumen gain is lost by the recoil of the vessel wall. This luminal loss can be limited by deploying a mechanical scaffold (stent) which provides in most cases a permanent support to the vessel wall (see section 1.2.1).

All of the techniques (coronary artery bypass surgery, balloon angioplasty and stent placement) are still used to treat atherosclerotic lesions in clinical practice. The selection of a particular technique or a combination of different procedures for a specific patient depends on many factors such as number of lesions, the location and the severity of the stenosed segments, the personal preference of the clinician (and patient) and many others. A detailed discussion and comparison on the application of the different techniques in terms of safety, outcome and cost-effectiveness falls outside the scope of this work. The further discussion will be limited to stent placement.

1.2.1 Stent placement

The first stent was implanted in 1986 and was a major breakthrough. From 1992 to 2004, the total number of percutaneous coronary interventions and the number of coronary stenting procedures in Europe increased from approximately 184000 to 885000 and from 3000 to 770000 [2]. The most important category of coronary stents are balloon-expandable, referring to the expansion mechanism of the stent which is driven by the inflation of an angioplasty balloon (see Fig. 1.7). The insertion procedure is very similar to the one previously described for balloon angioplasty. However, the higher stiffness of the system due to the stent structure which is crimped around the folded balloon slightly increases the technical complexity of the intervention. Stent placement in patients having high grade stenosis often requires initial predilatation with a more flexible angioplasty balloon having a lower profile. After positioning the stent at the location of the narrowing, the stent is deployed by gradual inflation of the balloon. Subsequently, the balloon is deflated and the complete system is removed from the body, except for the permanently deformed stent which remains in place, keeping the artery open (see Fig. 1.8).

A second category of stents based on the expansion mechanism are the self-expandable stents. During insertion, these spring-like stent structures are located inside a delivery catheter and removal of this restraining catheter results in their deployment. Typically, these stents are made of Nitinol, a Nickel-Titanium based alloy having superelastic properties. Nitinol devices have the ability to undergo large deformations when loaded and to return to their original shape when the load is removed. Although rarely used for

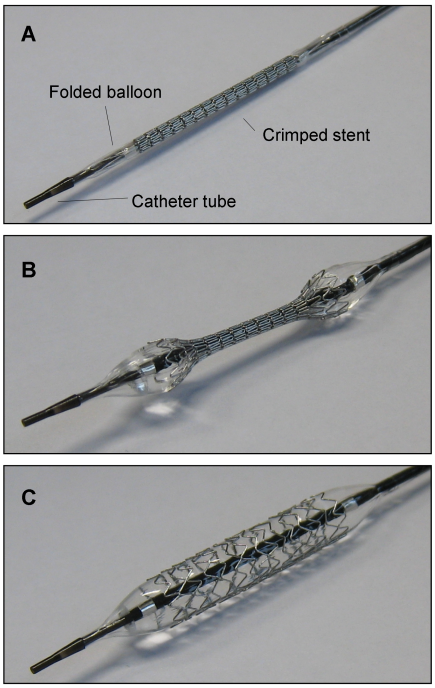

Figure 1.7: Unconstrained expansion of the Endeavor stent (Medtronic): Panel A shows the stent, crimped around a folded angioplasty balloon. The deployment starts at the stent ends (panel B) and continues towards the stent center (panel C).

coronary applications, these self-expandable stents are the preferred choice for improving blood flow in stenosed peripheral arteries (e.g. carotid artery and femoral artery), as their spring-like behaviour results in a permanent outward force on the inner wall of these highly deformable arteries. In case of balloon-expandable stents, large vessel deformations might lead to undesired permanent deformations that would jeopardise their scaffolding function.

Palmaz et al. [23] introduced balloon mounted stents to open up stenosed pheriperal arteries in 1985. Schatz et al. [24] subsequently modified the Palmaz stent, leading to the development of the commercially successful Palmaz-Schatz stent. In 1994, two important randomized clinical trials confirmed the superiority of the Palmaz-Schatz stent compared to balloon angioplasty [25,26], establishing the elective placement of coronary stents as a standard treatment. According to those studies, stent placement significantly reduced restenosis (i.e. a renarrowing of a previously treated vessel segment) levels compared to balloon angioplasty from approximately 30-

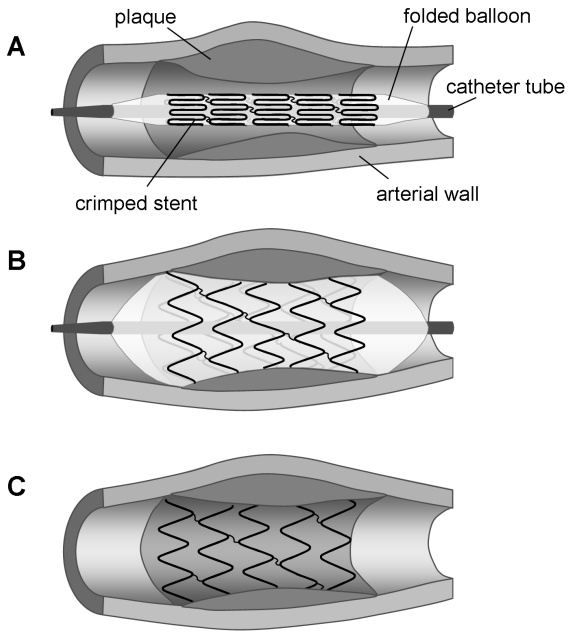

Figure 1.8: Schematic illustration of a balloon-expandable stent placement. After correct positioning of the crimped stent (panel A), the balloon is inflated at high pressure leading to the expansion of the device and to an improved luminal area (panel B). Finally, the procedure is completed by deflating and extracting the balloon catheter. The stent remains in place to keep the vessel open (panel C).

40% to 20-30%.

In 2002, a major revolution was caused by the introduction of Drug-Eluting Stents (DES), having an active coating to inhibit in-stent restenosis. These DES typically consist of three components: a metallic stent platform, a polymer coating, and the drug itself stored within the coating. After deployment, the drug is slowly released from the coating to the injured vessel wall. Clinical trials revealed restenosis rates below 10% for both the sirolimus-eluting Cypher stent (Cordis, Johnson & Johnson) and the paclitaxel-eluting Taxus stent (Boston Scientific). However, standard Bare Metal Stents (BMS) are still used on a large scale as the cost-effectiveness of DES compared to new generation BMS remains a concern [27]. In addition, discussions regarding the long-term safety of DES caused a decline of their use in 2006. Nevertheless, some recent studies demonstrate the limited impact of DES on the long-term safety in comparison with BMS [28].

Two important current trends in percutaneous coronary intervention are the development of drug-eluting balloons and biodegradable stents. One type of drug-eluting balloon (SeQuent Please, B. Braun) has a drug matrix applied to the outer balloon surface. This matrix consists of paclitaxel, embedded in a hydrophilic iopromide, which increases the solubility and transfer of paclitaxel to the vessel wall. The matrix is fragmented into small units at inflation, the iopromide dissolves and the paclitaxel migrates into the vessel wall. An inflation time of 30 seconds is recommended for optimal drug delivery. Drug-eluting balloons have the potential to resolve the current limitations of DES and can be used with or without BMS. Treatment of in-stent restenosis with paclitaxel-coated balloon catheters significantly reduced the incidence of restenosis [29] and avoids stent-in-stent situations. Furthermore, this approach results in a uniform drug distribution in the vessel wall whereas DES may lead to an inhomogeneous drug distribution [30].

Current metallic stents remain permanently in the artery, although their scaffolding function is only required for a number of weeks [31]. Therefore, considerable efforts have been spent to create safe and effective metallic and polymer based biodegradable stents. Such biodegradable devices would reduce the duration of the antiplatelet treatment, which is needed to avoid thrombosis. However, their development is hampered by difficulties in replicating the properties of conventional stainless-steel or cobalt-chromium stents [31, 32].

The design of the last generation stents differs a lot from the first commercially available stents. Nowadays, stents usually demonstrate a better mechanical behaviour in terms of the following criteria (non-limiting list):

- **Flexibility:** The crimped stent must be flexible to pass all tortuous vessels and bifurcations during insertion. Furthermore, the expanded stent should have sufficient flexibility in order not to straighten the often curved vessels.

- **Radial strenght:** Minimal luminal loss after deflation of the balloon can only be obtained if the stent has a sufficient radial strength in order to resist the compressive forces of the vessel wall.

- **Elastic recoil:** The diameter of the expanded stent may change (i.e. radial elastic recoil) after deflation of the balloon as illustrated in Fig. 1.9. It can be defined as $(D_f - D_i)/D_i$. This elastic recoil should be minimized as it reduces the final lumen.

- **Foreshortening:** The longitudinal contraction (see Fig. 1.9) which may occur during expansion should be as little as possible in order to minimize the shearing on the endothelial layer. Such shearing may lead to endothelial damage [33]. It is often quantified as $(L_f - L_o)/L_o$.

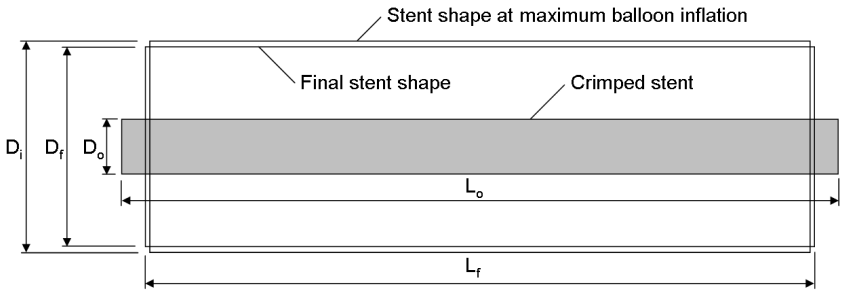

Figure 1.9: Schematic illustration of stent recoil and foreshortening (L_o and D_o denote the length and diameter of the crimped stent, L_f and D_f denote the length and diameter of the final stent shape after balloon deflation and D_i refers to the intermediate stent diameter at the maximal balloon pressure).

- **Crossing profile:** To facilitate placement, the crossing profile of the complete device (i.e. D_o in Fig. 1.9) should be minimized.

The large number of design prerequisites turn the development cycle into a process of compromises as some requirements result in contradictory design recommendations. For example, reducing the strut thickness will lead to a lower crossing profile of a stent system, but will have a negative impact on the radial strength. This explains the large variety of the developed balloon- and self-expandable stent designs (see Fig. 1.10 and 1.11). It should be noted that the design process is further complicated by the numerous patents which limit the available design space. However, spending time and money to develop adequate stent designs seems justified as it was shown that restenosis rates are design dependent for BMS [34, 35].

1.2.2 Stenting bifurcation lesions

Balloon angioplasty of coronary bifurcation lesions was soon identified as an unfavorable determinant for angioplasty success [36]. Using advanced techniques such as kissing balloon inflation (i.e. simultaneous inflation of an angioplasty balloon in both branches) improved the outcome, but these interventions were still associated with high complication and restenosis rates [37]. Using first generation stents for bifurcation lesion treatment yielded unsatisfactory results, mainly because of the limited access to the SB [38]. Advances on the stent design level as well as the availability of very low profile balloons facilitated the deployment of stents at bifurcations and led to a wave of new bifurcation stenting techniques. However, the need for re-intervention continued to be high [39, 40]. The introduction of DES markedly reduced the restenosis rates in the main vessel, but the

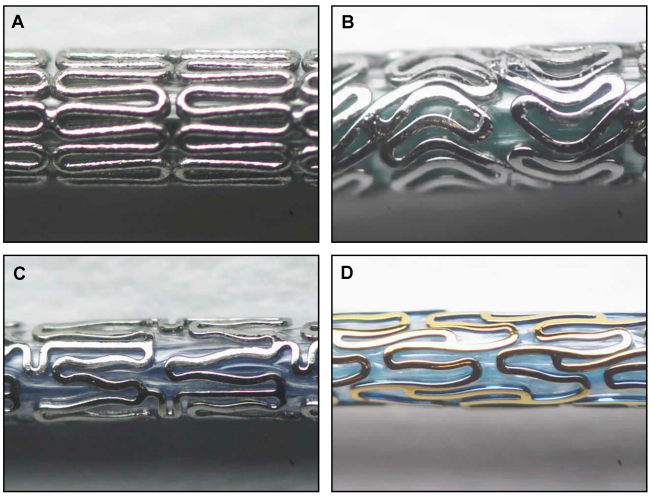

Figure 1.10: Examples of balloon-expandable stents. A: Endeavor (Medtronic), B: Taxus Liberté (Boston Scientific), C: Promus (Boston Scientific), D: PRO-Kinetic (Biotronik). The images do not have the same scale.

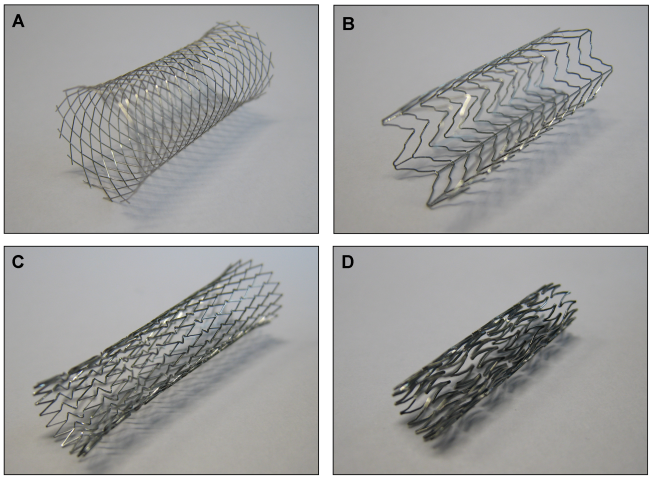

Figure 1.11: Examples of self-expandable stents. A: Wallstent (Boston Scientific), B: RX Acculink (Abbott Vascular), C: Xact (Abbott Vascular), D: SelfX (Abbott Vascular). The images do not have the same scale.

results for the SB were disappointing with restenosis rates of approximately 15% [4,41]. Furthermore, the higher incidence of stent thrombosis compared to conventional stenting remains a concern [41, 42]. Since the treatment of bifurcation lesions is estimated to be 15% of all percutaneous coronary interventions, further understanding of this complex issue is required to optimize the safety and outcome of bifurcation stenting procedures [38, 43].

Many different bifurcation stenting techniques have been proposed, with various levels of complexity and each of them having one or more limitations. In 2000, Lefèvre et al. [44] proposed a classification system for these techniques, which was further extended by Louvard et al. [45]. Currently, the MADS classification (Main, Across, Distal, Side) has been unanimously accepted by the European Bifurcation Club and divides the techniques into four major groups depending on in which arterial segment a first stent is implanted (see Fig. 1.12 and 1.13) [18]. The most important techniques are outlined below. An important question (which is still unanswered) is whether or not to systematically predilate the MB and SB before stenting. The advice of the European Bifurcation Club regarding this is to predilate the SB in case of long or calcified SB lesions [18].

1.2.2.1 Provisional stenting

The provisional stenting strategy which involves stent placement in the main vessel first and then the SB when necessary is currently the gold standard for the majority of the treatments [18]. Elective implantation of two stents may be considered in case of SB lesions which are longer than 2 or 3 mm [18]. The first step of provisional stenting is to decide whether a guide wire is needed in the SB. There are two main advantages of this jailed wire technique[3]. First, such a jailed wire favorably alters the bifurcation angle and turns T-shaped bifurcations into Y-shaped bifurcations, resulting in easier access to the SB. Second, total occlusion of the SB during stent placement in the MB is prevented. However, retracting this trapped wire may damage the endothelial layer and therefore systematic use is still debated. It is recommended to use this jailed wire technique for complex lesions. If this jailed wire technique is used, then the MB stent should be initially deployed at low pressure (8 atm) in order to minimize the vessel wall injury and to avoid damage of the jailed wire. After having rewired the SB through the side of the stent using the jailed wire as a landmark (if used), this jailed wire is removed and the stent can be postdilated at high pressure. Depending on the angiographic result, the complexity of the lesion and personal preference, the operator can also decide to perform final kissing balloon postdilatation. An angiographic assessment of the SB lesions is not always enough, as Koo

[3] Expanding the MB stent when a guide wire is placed into the SB 'jails' this SB wire between the stent struts and the vessel wall.

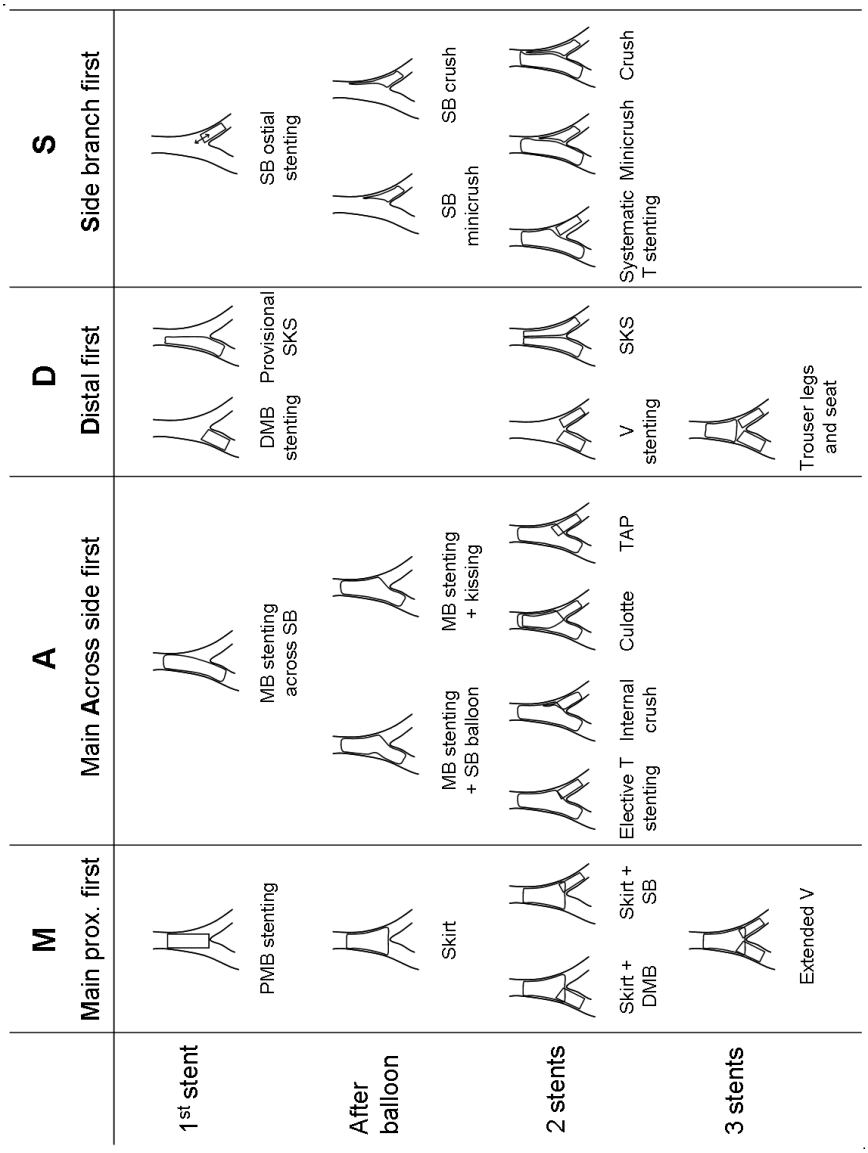

Figure 1.12: MADS classification of the different bifurcation stenting techniques (adapted from [18]). Clarification of the abbreviations: MB = main branch, PMB = proximal main branch, DMB = distal main branch, SB = side branch, prox = proximal, TAP = T-stenting and small protrusion technique, SKS = simultaneous kissing stents.

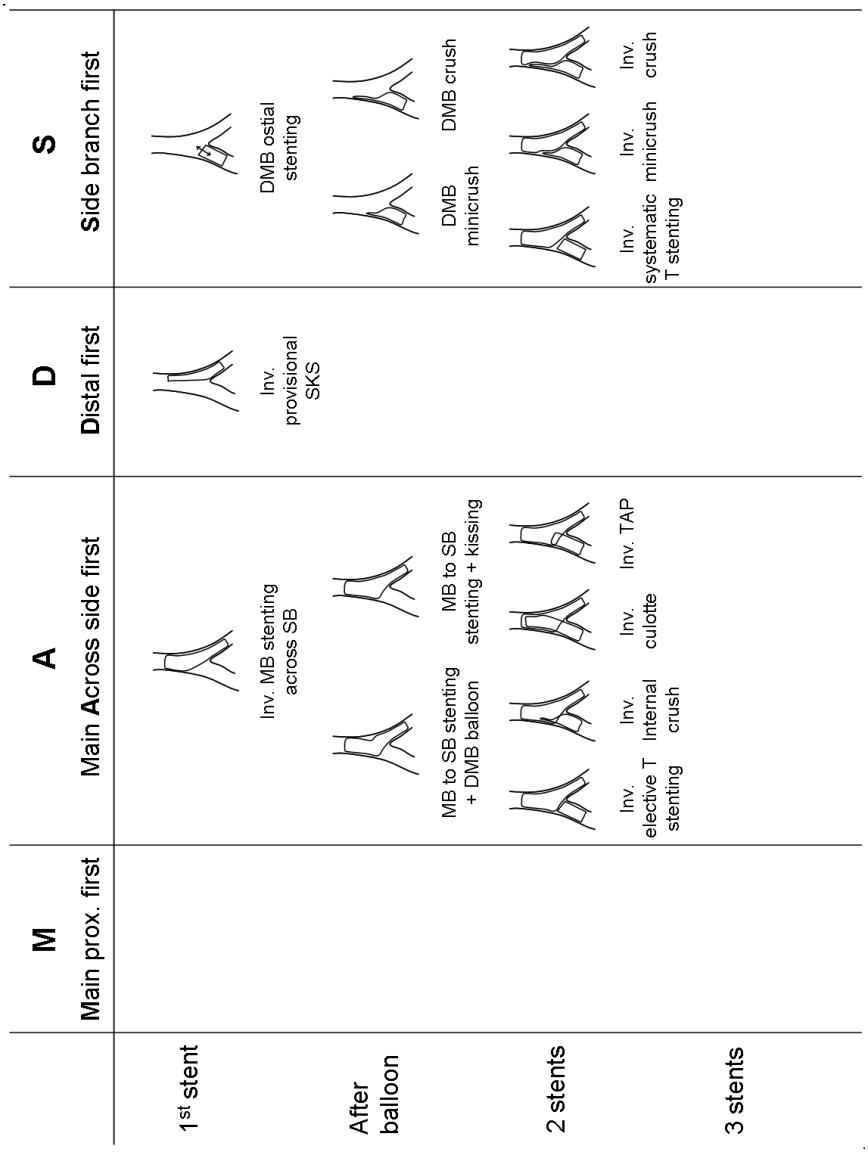

Figure 1.13: MADS classification of the inverted techniques (adapted from [18]). Clarification of the abbreviations: MB = main branch, PMB = proximal main branch, DMB = distal main branch, SB = side branch, prox = proximal, TAP = T-stenting and small protrusion technique, SKS = simultaneous kissing stents, inv = inverted.

et al. [46] have shown that about 70% of all ostial lesions following MB stenting are functionally not significant. Moreover, in this study, there were no lesions with $< 75\%$ SB diameter stenosis that had a fractional flow reserve (FFR) < 0.75. The main reasons to perform kissing balloon postdilatation are to optimise the strut appositioning and improve the SB access. The last step, stenting the SB, only occurs if the result of the SB is unsatisfactory. Several techniques that will be described in detail in the next sections are available to stent the SB at this point, such as T stenting, internal crush and culotte stenting.

1.2.2.2 T stenting

T stenting involves stenting both the MB and SB in a T-shaped manner and is best suited to treat bifurcation lesions with an angle close to 90° [47]. Using this technique for bifurcations where the angle significantly differs from 90° results in incomplete ostial coverage or in stent struts protruding into the MB. The operator can choose to stent the MB or the SB first. If a provisional SB stenting strategy is applied, then the MB stent is implanted first and T stenting can be performed when suboptimal SB results occur. In this case, the SB stent is advanced into the SB through the already expanded stent. To avoid this technically demanding insertion for lesions where it is a priori the intention to stent both branches, stenting the SB first may be the preferred option. This second approach requires very accurate positioning because protrusion of this stent into the MB may hamper subsequent stent placement in the main vessel. Therefore, alternative strategies have been suggested to overcome this limitation. Kobayashi et al. [48] proposed to position the main vessel stent prior to deployment of the stent in the SB (modified T stenting). As such, potential strut protrusions do not compromise MB stenting. Furthermore, protruding struts will be compressed against the vessel wall after expansion of the MB stent. A second suggestion is to inflate a balloon at low pressure (4 atm) in the MB after placing the undeployed stent in the SB. The stent can then be accurately positioned at the SB ostium by sligthly pulling back the stent against the already inflated balloon while limiting strut protrusion [49]. The same principle can be applied when the main vessel is stented first to assure minimal protrusion into the MB while guaranteeing good ostial coverage and is called the TAP technique (T stenting And small Protrusion) [50].

1.2.2.3 The crush technique

The crush technique was introduced after observation of high restenosis rates at the ostium of the SB using DES. Incomplete ostial coverage and the resulting suboptimal drug delivery were assumed to be important contributors to the higher incidence of restenosis at that location. The main

advantage of the crush technique is the complete coverage of the SB ostium for a large range of bifurcation angles. The procedure starts with advancing two stents, one in the SB and one in the MB. The SB stent is then retracted into the MB over a distance of 4 to 5 mm. The MB stent should be positioned so that its proximal marker is located more proximal than the proximal marker of the SB stent. Following the expansion of the SB stent (which protrudes in the main vessel), the delivery balloon and guide wire are removed. Subsequently, the MB stent is deployed, crushing the protruded struts of the stent implanted in the SB against the wall of the main vessel, hereby leading to three layers of struts in the proximal section of the bifurcation near the SB ostium. Final kissing balloon inflation drastically improves the outcome and is therefore mandatory [51]. However, recrossing three layers of struts can be difficult or even impossible and makes the procedure laborious. Concerns regarding the risk of thrombosis due to the relatively large zone with three strut layers lead to the introduction of the mini-crush technique [52]. Almost the complete mini-crush procedure is identical to the classic crush technique, except for the retraction of the SB stent that is limited to 1 or 2 mm instead of 4 to 5 mm. This reduces the region with increased strut density.

The step crush technique was proposed to make the crush technique compatible with a 6 Fr guiding catheter, which may be useful when a radial vascular approach is being used[4]. The procedure is again very similar to the standard crush, but the stents are now sequentially inserted and deployed. The initial position of the SB stent is identical, but a balloon is advanced in the MB and this balloon is then used to crush the proximal part of the SB stent against the wall of the main vessel. After removal of the balloon, the MB stent is positioned and deployed.

The reverse or internal crush can be performed when a provisional SB stenting strategy was applied, but a SB stent is required after stenting the main vessel and subsequent kissing balloon inflation. First, a second stent is advanced into the SB through the deployed stent, followed by the placement of a balloon in the MB. Then the SB stent is retracted into the MB and deployed. The balloon and the wire are removed and the MB balloon is inflated to crush the proximal portion of the SB stent against the struts of the MB stent. Again, final kissing balloon postdilatation should be performed to optimize the strut apposition.

1.2.2.4 Culotte stenting

The culotte technique was first described by Chevalier et al. [53] and has the main advantage of providing complete ostial coverage for a large range of bifurcation angles. This technique can be used as a two-stent strategy

[4] The radial artery is normally slightly smaller than the femoral artery.

or for bifurcation lesions treated with a provisional stenting approach that need a second stent after stenting the MB. The most angulated branch (i.e. usually the SB) is stented first when a two-stent strategy is applied. The other branch is then rewired through an expanded cell of the deployed stent and dilated. The next step involves the advancement of the second stent through the deformed cell and subsequent deployment, hereby creating a double layer of struts in the proximal part of the bifurcation. Final kissing balloon inflation can be performed in order to minimize the number of floating struts. The procedure can be technically demanding due to the two rewiring steps. Similar to the crush technique, culotte stenting leads to high metal concentrations in the proximal part of the bifurcation.

1.2.2.5 V stenting and simultaneous kissing stents technique

The current definition of V stenting differs from the originally proposed V stenting technique [54] in which a non-crimped Palmaz-Schatz stent (PS153, Johnson & Johnson) was manually bended at one of its connector elements resulting in two parallel cylinders that were then crimped by the operator on two balloons. This self-made device was advanced to the bifurcation until the bended connector touched the carina. Both stent parts were finally deployed, one in each distal branch. Nowadays, the term V stenting is used for a technique that involves the implantation of two separate stents in the two distal branches. These two stents are positioned with their proximal ends at the carina, and may form a new carina when these two stent ends touch each other. The Simultaneous Kissing Stent (SKS) technique is very similar to V stenting, however, after advancing a stent in each branch, both stents are pulled back into the proximal main vessel until both proximal stent ends touch each other over a distance of 5 mm or more [55].

1.2.2.6 Skirt technique

The skirt technique was introduced to treat lesions immediately proximal to a bifurcation and requires manual manipulation of the device [56]. A stent has to be crimped on two balloons, but this should be done very carefully because such manipulation may damage the polymer coating of DES. This stent system is then advanced over two wires, one in each branch, until the distal stent end hits the carina. Finally, both balloons are simultaneously inflated.

1.2.2.7 Y stenting

Y stenting involves the deployment of a stent in each distal branch (V-stenting), followed by a third stent implantation in the proximal MB as close as possible to the carina to complete the 'Y', which can be achieved

by using the skirt technique. According to the MADS classification system, this technique is called 'trousers legs and seat'. The sequence of stent implantation is inverted during the 'extended Y technique', starting with the proximal MB stent and then stenting the distal branches. Also this technique receives a different name in the MADS classification: the extended V technique.

1.2.2.8 Clinical outcomes

A large number of clinical studies have been published during the last couple of years focusing on different bifurcation stenting techniques. However, these clinical studies did not answer the question of which technique to use for a particular bifurcation lesion (or type of lesion). One important reason for this is that most published results are based on nonrandomized registries, which unfortunately limits the value of the conclusions. To date, only very few randomized trials have been organised in the field of bifurcation stenting [4, 41, 57–59]. The results of these studies and registries are often difficult to compare because of the various lesion classification systems that have been adopted in the past and the lack of detailed descriptions of the applied stenting techniques. The large number of different stent designs used further complicates the interpretation of the data. For example, the culotte technique may give a good outcome when using design A, but the results may be quite poor when using design B. Finally, the high crossover rate when comparing one to two stenting techniques makes it difficult to draw solid conclusions. The following paragraphs try to summarize some of the main findings in the field of bifurcation stenting. The reported numbers should however be read critically because of the previously mentioned limitations.

Before the introduction of DES, several authors [40, 60, 61] reported that stenting both vessels using a two-stent technique did not provide an advantage as compared to a single stenting strategy (in combination with a dilatation of the other branch). At that time, the outcome was often quite disappointing whatever strategy used. For example, Yamashita et al. [40] reported major adverse cardiac events rates (defined as death, myocardial infarction or target lesion revascularization) of 51% and 38% at six-month follow-up for the two-stent and the single stent cases respectively.

Thuesen et al. [62] published a subgroup analysis of the bifurcation lesions treated during the randomized SCANDSTENT trial, which compared sirolimus-eluting to bare metal stents. It was observed that the sirolimus-eluting stents reduced the angiographic restenosis rate from 28.3% to 4.9% in the MB and from 43.4% to 14.8% in the SB. Major adverse cardiac events occurred in 9% of the cases with sirolimus-eluting stents and 28% with bare metal stents. These results lead to the widespread use of DES when dealing with bifurcation lesions. It should be noted, however, that the restenosis

rate for the SB remains higher as compared to the DES standard values for unbranched vessels.

In a randomized trial, Pan et al. [63] compared sirolimus-eluting with paclitaxel-eluting stents for the treatment of bifurcation lesions. Patients treated with sirolimus-eluting stents showed significantly lower rates of restenosis and target lesion revascularization than patients treated with paclitaxel-eluting stents. These findings were consistent with a non randomized study conducted by Hoye et al. [64].

The question whether or not to use two drug-eluting stents on a routinely basis instead of applying a simpler one stent strategy (using a DES) was addressed by a number of randomized trials. In 2004, Colombo et al. [41] did not find a statistical significant difference between the simple and the complex approach. The main limitation of this study was the extremely high cross-over rate of more than fifty percent. In the same year, the results of a study conducted by Pan et al. [57] were published and showed a similar trend: stenting both branches seems to provide no advantages over stenting the MB only followed by SB balloon dilation. The cross-over rate in this study was limited (five out of 91 patients). To date, the largest randomized bifurcation trial with 413 patients comparing simple (1 stent) versus complex (2 stents) stenting techniques for DES is the Nordic Bifurcation Study [58]. Again, there was no statistically significant difference in terms of MACE (major adverse cardiac events) and target lesion revascularization at six-month and at 14-month follow-up [65]. However, the elective implantation of two stents was associated with increased procedural and fluoroscopy times. In addition, implanting two stents obviously leads to a higher cost and therefore, the authors recommend the simpler, provisional strategy as the routine bifurcation stenting technique. Ferenc et al. [59] compared routine T-stenting with provisional T-stenting, hereby limiting the number of variables of the study. Allowing several two-stent techniques as was done during the Nordic Bifurcation Study [58] (culotte, crush, etc.) makes it difficult to draw conclusions for one of these techniques, compared to the simple one-stent approach. Ferenc et al. [59] concluded that routine T-stenting did not improve the target lesion revascularization as compared to provisional T-stenting, which is again in agreement with all previous studies. Recently, the results of the CACTUS trial have been published by Colombo et al. [4]. This randomized trial compared the crush technique with a provisional SB stenting approach. At six months, target lesion revascularization and MACE did not differ significantly.

Future randomized trials should address the large number of open questions: Is there a need for systematic kissing balloon postdilatation? If a two-stent technique is required, which one should be applied for which type of bifurcations? Does the selected stent design impact the outcome for a particular technique? But as dr. Wijns (Cardiovascular Center, OLV, Aalst, Belgium) mentioned during the European Bifurcation Club meeting

in Prague (2009), the focus should be on the dedicated devices which are designed for these lesions instead of putting efforts in comparing the various complex techniques that were developed for suboptimal stent designs.

1.2.3 Dedicated bifurcation stents

The introduction of DES and the improved insights into the different techniques resulted in markedly lower restenosis rates when treating bifurcation lesions. The very good results observed after stenting unbranched vessels can, however, not yet be obtained. It should be noted that the acceptable results for bifurcation stenting that have been published are obtained by interventional cardiologists who have a particular interest in this specific domain. These interventional cardiologists are aware of the different causes of suboptimal strut positioning and probably spend more time to optimize the result (e.g. advancing a SB balloon catheter through the side of the MB stent can be very time-consuming). The importance of operator-experience was clearly demonstrated by Latib et al. [66] who compared the outcomes of bifurcation stenting at their institution over three consecutive periods. It is therefore likely that the results obtained by highly skilled operators are not representative for all centers. Hence, there is a need for user-friendly dedicated bifurcation stents which further improve the current outcomes but that also reduce the technical difficulty.

As already stated, bifurcation lesions account for approximately 15-20% of all lesions that need percutaneous treatment, leading to more than 500000 bifurcation interventions annually [67]. This interesting market attracts the attention of large medical device companies but also leads to a number of start-ups focusing on this niche market. As a result, a large number of dedicated bifurcation stent systems have been developed and other systems are still under development. The available product information of these stent systems is often limited because some of these devices are not yet available on the market. Fortunately, the work of Abizaid et al. [68] and the very recent review of Latib et al. [66] provide a very nice overview of the recent bifurcation stents. The discussion of the different stent systems provided in the next sections is often based on these two papers.

1.2.3.1 Antares Coronary Stent System

The Antares (Trireme Medical, California, USA) is a balloon-expandable bare metal stent for provisional stenting. The stent is made from stainless steel and has a strut thickness of 89 µm. Only one wire is needed for initial insertion but a 'stabilizing wire' is concealed within a dedicated lumen in the catheter. Once the stent is positioned at the bifurcation, the operator should torque the catheter to align the stent's central opening (indicated

with radiopaque markers) with the SB ostium. Then, the stabilizing wire can be released at the central opening of the Antares stent and inserted into the SB. This approach minimizes the risk of wire wrap. Finally, the stent can be further advanced on both wires and deployed by inflating a single balloon. A SB support structure is automatically deployed with elements protruding approximately 2 mm into the SB that provide ostial scaffolding (see Fig. 1.14).

The first-in-man study of 11 patients/lesions treated with the Antares stent demonstrated a device success rate of 100% [66]. At 30 days follow-up, there were no adverse events reported[5].

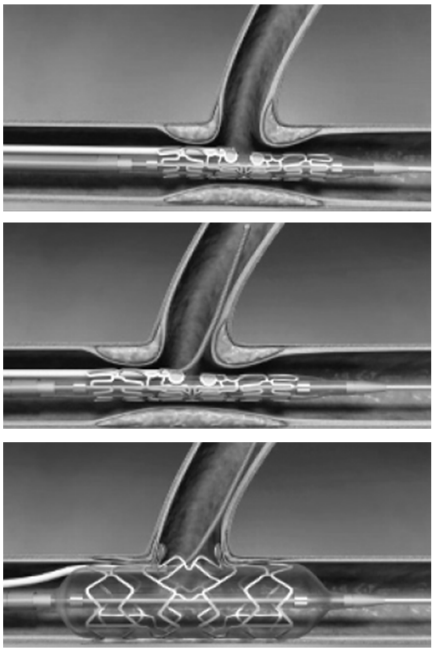

Figure 1.14: Schematic overview of the insertion and deployment procedure of the Antares stent system (Trireme Medical). The top panel shows the device when the stabilizing SB wire is still within the dedicated lumen. Following to correct positioning, the stabilizing wire is advanced into the SB (middle panel) and the stent is finally deployed by inflating a single balloon (bottom panel). Adapted from [66].

[5] These numbers are based on the review paper of Latib et al. [66] since the original report of the first-in-man study could not be accessed by the author.

1.2.3.2 Axxess Bifurcation Stent System

The Axxess Plus stent (Devax, California, USA) is a self-expandable conically shaped nitinol stent placed in the parent vessel up to the carina (see Fig. 1.15). The angle between the branches should be smaller than 60°. In such bifurcations, it is claimed that the combination of the self-expandable properties and the conical shape allows adequate scaffolding of the ostia of the two daughter vessels. The implantation procedure starts with the insertion of a guide wire in both branches, followed by a mandatory predilatation of the main vessel [69]. The Axxess stent is then inserted over one of the wires and the stent is partially deployed by retracting a covering sheath, hereby exposing the three distal markers (see Fig. 1.15). This should allow accurate positioning of the device at the level of the carina prior to full stent expansion. A fourth marker is located at the proximal edge of the stent. The symmetric design of the stent makes rotational orientation unnecessary. The abluminal surface of the struts (thickness of 152 μm) is coated with a resorbable polymer that delivers Biolimus A9, an anti-restenotic drug [70].

The Axxess Plus trial clearly showed the frequent necessity of implanting one or more additional stents in the distal branches since a total of three stents was used in 42% of the patients [69]. The Axxess stent was successfully implanted in 130 of 139 cases (93.5%). In six of the failure cases, the stent was placed distal or proximal to the intended location. At six months follow-up, the in-stent restenosis within the Axxess stent was 4.8% and the overall target lesion revascularization was 7.5%.

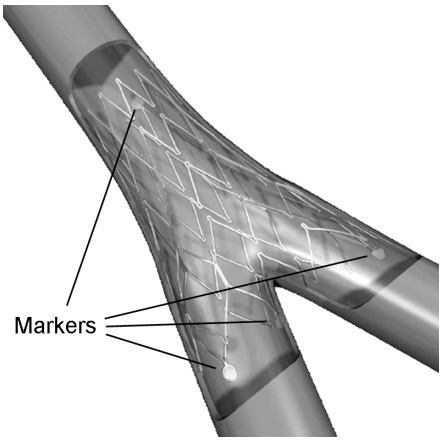

Figure 1.15: The design of the self-expandable Axxess stent (Devax) aims at providing adequate coverage in the bifurcation region. Placement is facilitated by the four radiopaque markers (three distal and one proximal). Adapted from [70].

1.2.3.3 Multi-Link Frontier

The Multi-Link Frontier stent system (Abbott Vascular, Redwood City, California, USA) is a 316L stainless steel stent premounted on a dedicated delivery system with two balloons and two guidewire lumens and requires a 7 Fr guide catheter [71]. The stent design differs along the stent length and can accomodate to larger diameters in the proximal part. The ends of the two balloons are joined by a mandrel which leaves the tip of the SB balloon catheter and is distally enclosed within a pocket in the MB balloon catheter shaft. This facilitates tracking and avoids the risk on guidewire crossing. After removing the joining mandrel (and thus unjoining the balloon tips), a guide wire can be inserted into the SB. The final position of the stent is obtained by further advancing the device on both wires until resistance is felt. The device is deployed by kissing balloon inflation since the catheter incorporates a common inflation lumen for the simultaneous inflation of the two balloons (see Fig. 1.16).

Lefèvre et al. [71] evaluated the safety and feasibility of this device during the FRONTIER stent registry. A device success rate of 91% was achieved for the 105 enrolled patients. The MACE rate (death, myorcardial infarction and target lesion revascularization) at six months was 17.1% and the overall restenosis rate for any branch was 44.8%.

Abbott currently develops and investigates a drug-eluting variant of the Frontier stent, the Pathfinder, which is based on the Xience V technology [72]. The Pathfinder will be made from the stronger cobalt-chromium alloy allowing a reduced strut thickness in comparison to the Multi-Link Frontier stent (i.e. 81 µm instead of 99 µm).

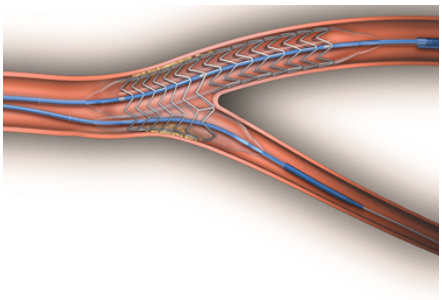

Figure 1.16: The Multi-Link Frontier stent (Abbott Vascular) is deployed by the simultaneous inflation of two balloons [73].

1.2.3.4 Nile Croco

The Nile Croco (Minvasys, Genevilliers, France) is a device consisting of a bare metal cobalt-chromium stent mounted on a dedicated delivery system with two separate balloons requiring independent manipulation and pressure monitoring. The stent is crimped on the first balloon and on the distal tip of the second balloon catheter. Insertion requires two guidewires and a 6 Fr guiding catheter. If wire wrapping occurs, then the SB wire should be pulled back into the MB and finally re-advanced into the SB. After the stent is deployed within the MB by inflating the first balloon, the second balloon is advanced to perform final kissing balloon inflation with the aim of opening the struts towards the SB and providing ostium scaffolding (see Fig. 1.17). The proximal part of the SB balloon is designed to avoid overexpansion of the proximal MB when performing kissing balloon inflation.

Garcia Del Blanco et al. [74] reported a device success rate (defined as successful device placement and final kissing balloon postdilatation) of 96% during a multicentre Nile Croco registry (103 patients). The MACE rate (defined as cardiac death, myocardial infarction and target lesion revascularization) at six months in the 85 patients that were followed was 12%.

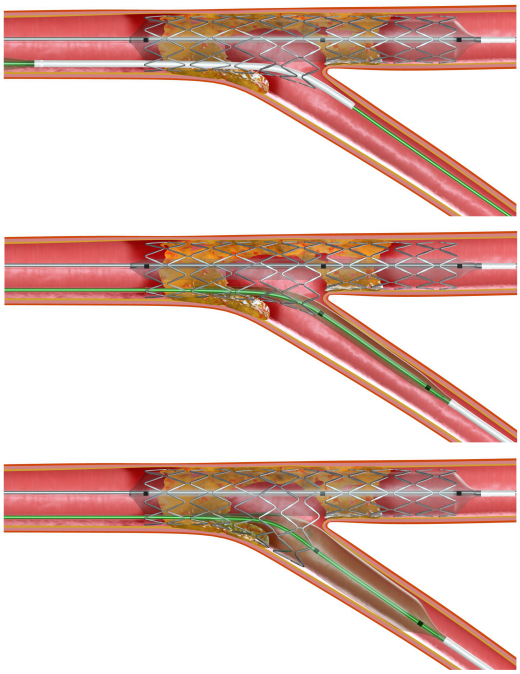

Figure 1.17: Schematic illustration of the deployment of the Nile Croco bifurcation stent (Minvasys). Courtesy Minvasys.

1.2.3.5 Petal

The Petal stent (Boston Scientific, Massachusetts, USA) was originally developed by Advanced Stent Technologies as a bare-metal stainless steel stent called AST Petal, but the second generation device (i.e. Taxus Petal) has a platinum chromium platform and will elute paclitaxel like the Taxus stent. The stent is characterized by its unique centrally located side aperture, designed to scaffold the SB ostium with outwardly deploying strut elements (see Fig. 1.18). The crossing profile has been reduced, making the new device compatible with 6 Fr guiding catheters (instead of 7 Fr for the first generation Petal stent). After mandatory predilatation, a guide wire is inserted in each branch. The dual side-exchange delivery system has a main lumen that guides the catheter over the MB guide wire, while the secondary lumen facilitates proper alignment of the aperture to the SB ostium as it tracks over the SB guide wire [75]. Another particular feature of the device is the secondary elliptical balloon adjacent to the cylindrical MB balloon. The Petal stent is crimped over both balloons, which are connected to the same inflation lumen so that a single inflation device is needed. The crimping is performed in such a way that the secondary balloon is located under the side aperture and the petal elements (indicated in Fig. 1.18). Upon inflation, the main balloon deploys the stent into the MB, while the secondary balloon deploys the petal elements into the SB ostium.

A first-in-man study with 13 patients was conducted using the first generation Petal stent system [75]. The device was succesfully implanted in 12 patients. The device was not used in one case due to vessel dissection after predilatation. Twisting of the wires occurred in three cases and required repositioning of one of the wires before delivery could be accomplished. In one patient, stent rotation was impeded so that alignment with the SB did not initially occur.

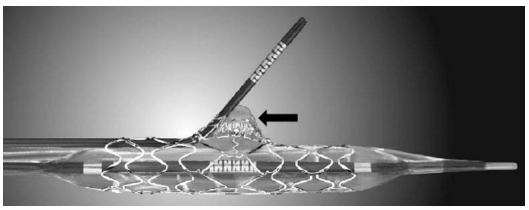

Figure 1.18: The Petal stent (Boston Scientific) has a side aperture with struts (the so-called petal elements) that deploy into the SB by inflation of the particular secondary balloon. Adapted from [66].

1.2.3.6 Sideguard

The Sideguard ostium protection device (Cappella, Massachusetts, USA) is a trumpet-shaped self-expandable nitinol stent with a low profile (less than 3.5 Fr). The SB is treated first when using this device, although the conventional approach is to stent the main vessel first. The combination of its short length and low crossing profile should lead to greater navigability even when dealing with calcified lesions. The trumpet-shaped SB stent is designed to provide complete ostial scaffolding and to minimize the arterial trauma (see Fig. 1.19) and will be indicated for bifurcation angles from 45° to 135°. Only one wire is required to insert the Sideguard and there is no need for rotational orientation, while longitudinal positioning is facilitated by a number of radiopaque markers attached to the stent. The expansion is triggered by inflating a balloon which tears a protective sheath that keeps the Sideguard in place until deployment. After removal of the SB wire, any conventional main vessel stent can be deployed. The procedure should be completed with a standard final kissing balloon inflation in order to optimize the strut appositioning of the MB stent. The current Sideguard stent is a BMS but the next generation will be drug-eluting with a biodegradable polymer [66, 76].

The device was successfully implanted in 21 of the 25 patients enrolled in a first-in-man study [77]. A second trial has begun with a modified Sideguard device [66].

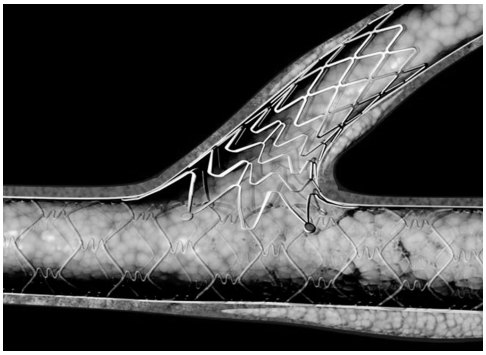

Figure 1.19: Illustration of the Sideguard ostium protection device (Cappella). Adapted from [76].

1.2.3.7 SideKick

The SideKick (Y-Med, San Diego, California, USA) is a balloon-expandable stent system advanced over a MB guide wire. The device contains an exit

port for a SB guide wire intended to preserve SB access during stent deployment. A different SideKick system can be employed depending on the location of the lesion. The difference between these systems is in the location of the exit port which is located proximally, in the middle or distally (see Fig. 1.20). Once the SideKick has reached the implantation position, the SB protection wire is inserted using the high torquability of the device. A clinical study with 20 lesions showed a device success rate of 80%. One major adverse cardiac event occurred due to a subacute stent thrombosis [78].

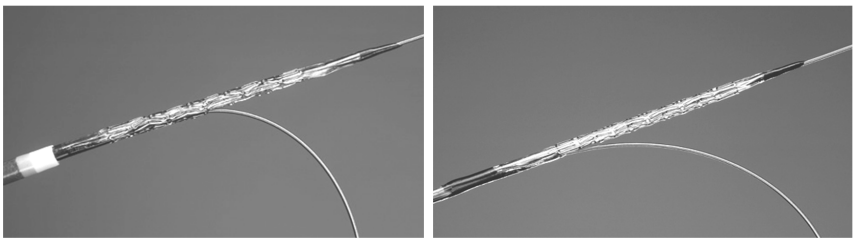

Figure 1.20: Comparison of two SideKick stent systems (Y-Med) with a different location of the exit port (left panel: central location, right panel: proximal location). Adapted from [79].

1.2.3.8 Stentys Coronary Bifurcation Stent

The Stentys Coronary Bifurcation Stent (Stentys, Paris, France) is a self-expandable nitinol stent for provisional stenting. The 5 Fr rapid-exchange delivery system requires one guidewire and is compatible with 7 Fr guiding catheters. The positioning of the stent is facilitated by the four stent markers (one proximal and three distal). After placement, the stent is expanded in the MB by rectracting a constraining sheath. The nitinol design is characterized by the small Z-shaped struts (strut thickness of 77 µm) of the circumferential ring elements. These ring elements are connected by a number of small bridges but can be disconnected by balloon angioplasty through the side of the stent. This unique feature provides the ability to achieve good ostium scaffolding as the stent has the potential to expand to a diameter of 7.5 mm (see Fig. 1.21). The procedural success of the device is independent of accurate positioning in contrast to some other dedicated bifurcation stents. It is claimed that the design is suitable for the majority of bifurcation angles (30° to 70°) [80].

The 30 days results of the first-in-man study demonstrated the feasibility and safety of the Stentys stent [81]. Procedural success was achieved in 39 of the 40 cases. The stent could not be positioned in one patient with highly tortuous vessels. The stent struts at the SB ostium could not be disconnected in two cases because the proximal part of the stent with non-

disconnectable struts was covering the SB ostium. For this first-in-man study, both a drug-eluting and a bare metal variant of the device were used. The drug-eluting stent is coated on the abluminal side with a durable polymer matrix (PESU) which contains paclitaxel.

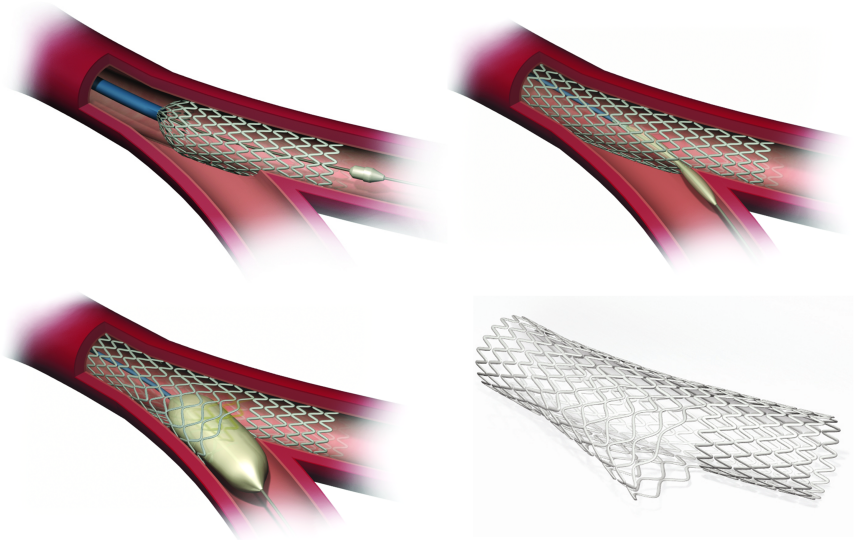

Figure 1.21: Schematic illustration of the implantation of the self-expandable Stentys device (Stentys) in the MB (top left), followed by the insertion and inflation of an angioplasty balloon through the cell closest to the carina (top right and bottom left). This dilation disconnects the struts (the drawings do not show the bridge elements) and results in improved SB access and ostium scaffolding. The bottom right panel shows the final stent shape. Courtesy Stentys.

1.2.3.9 Tryton Side-Branch Stent

The Tryton Side-Branch Stent (Tryton Medical, Massachusetts, USA) is a balloon-expandable cobalt-chromium stent with a strut thickness of 84 µm. The stent design consists of three distinct stent zones as shown in Fig. 1.22: a 'distal side-branch zone', a 'central transition zone' and a 'proximal main vessel zone' [82]. The SB zone has similar design characteristics as standard slotted tube stents and provides sufficient radial strength. The central transition zone consists in the circumferential direction of three panels, which can be deformed independently [83]. This central zone is designed with the intention to provide complete ostium scaffolding and to make the design suitable for all bifurcation angles (15° to 90°). The proximal main vessel zone has a very low strut density and consists of a proximal ring element connected to the transition zone by three long axially oriented bridging

elements. The stent can be implanted as a conventional stent using a single guidewire and does not require rotational orientation. The longitudinal positioning is facilitated by the four shaft markers: two standard markers at the balloon ends and two additional markers delineating the transition zone [82]. Two different delivery systems are available: a straight balloon that has a constant diameter and a stepped balloon with a larger diameter of the proximal part as compared to the distal part.

In all the cases of the first-in-man study involving 30 patients, the Tryton stent was used in conjunction with a standard DES for the MB as depicted in Fig. 1.22 [83]. This approach is very similar to Culotte stenting, but the dedicated design reduces the area with a double layer of struts in the proximal main vessel. The first-in-man study learned that predilatation of the MB is essential to advance the MB stent through the struts of the Tryton stent. The Tryton device is compatible with a 5 Fr guiding catheter, but a 6 Fr catheter is necessary to perform final kissing balloon after implantation of the MB stent. The Tryton stent failed to track to the lesion site in one patient [83]. At six months follow-up, the MACE rate (defined as cardiac death, myocardial infarction, coronary artery bypass surgery or target lesion revascularisation) was 9.9% and no restenosis in the SB was observed [84].

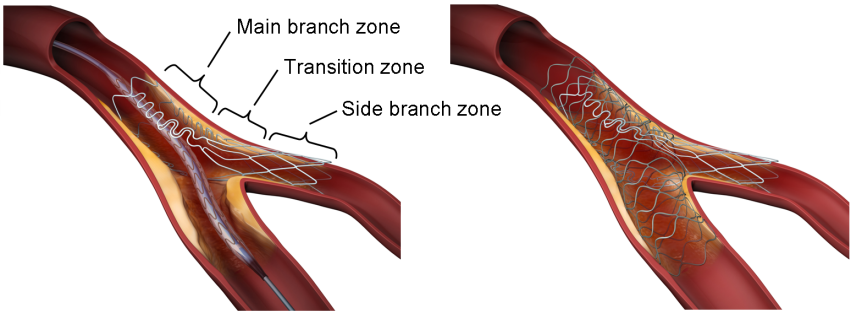

Figure 1.22: Schematic illustration of the Tryton device (Tryton Medical). The implantation of the Tryton stent using a stepped balloon is depicted in the left panel, which also indicates the three stent zones. The right panel shows the placement of a conventional MB stent through the struts of the Tryton stent. Courtesy Tryton Medical.

1.2.3.10 Twin-Rail

The Twin-Rail (Invatec, Roncadelle, Italy) is a stainless steel stent crimped on two balloons in its proximal portion and only on the main vessel balloon in its distal portion. The delivery system is compatible with a 6 Fr guiding catheter and requires two guidewires. There is only one inflation port, in contrast with the Nile Croco device which consists of two independent

balloons, since the single dual lumen catheter splits into the two distal balloons (see Fig. 1.23). Positioning of the stent is achieved by advancing the system over the two guidewires up to the carina of the bifurcation. At this point, no further advancement of the system is possible. The stent has a variable design along its length and can be expanded to larger diameters proximally than distally.

In 2005, Lefèvre [85] presented the results of the DESIRE trial at the Transcatheter Cardiovascular Therapeutics meeting and concluded that the angiographic success was high despite the relatively low rate of device success (75%) for this small cohort with 15 patients. At seven months, the target lesions revascularization rate was 14.3%.

Figure 1.23: Twin Rail bifurcation stent system (Invatec). Adapted from [66].

1.2.3.11 Conclusions

The design and development of dedicated bifurcation stents is an extremely fascinating technological challenge from an engineering point of view. There are a large number of often conflicting design requirements and it is therefore not surprising that the perfect solution seems not yet to be found. Some dedicated bifurcation stent systems have already been abandoned (e.g. AST SLK View, Jostent bifurcation, Bard XT, Medinol NIRside, Cordis DBS, etc.) because of their bulkiness, low flexibility and the technical complexity to implant them. The previous sections summarized the main characteristics of some of the devices currently available or under investigation and clearly show the large variety of design concepts (e.g. self-expandable versus balloon-expandable stents, single balloon versus double balloon systems, single wire versus double wire systems, SB versus MB stents, etc.). However, this overview is not complete. More devices are currently being developed but were not included due to a lack of available information. For example, Medtronic and Abbott Vascular are currently developing dedicated bifurcation stents based on their workhorse DES, the Endeavor and Xience V stent, respectively. Hexacath (Rueil-Malmaison, France) investigates a double-balloon stent system but also Boston Scientific further explores alternatives to their Taxus Petal stent.

Large trials are needed to evaluate all these different dedicated systems. One device that will perfectly treat all types of bifurcation lesions will probably never exist due to the large variety of both the bifurcation anatomy (e.g. angle and diameter) and plaque location. Therefore, it is highly likely that the current dedicated devices will be further improved in future and that totally new concepts using for example biodegradable struts or drug-eluting balloons will be investigated.

1.3 Bifurcation stent research

The previously described bifurcation stenting techniques are usually investigated and optimized using bench tests. A similar 'trial and error' based experimental approach is in many cases the main tool to develop new (dedicated bifurcation) stents [75, 80, 86]. Computer simulations such as finite element analysis (FEA) are less established as a research and development tool in the domain of bifurcation stenting. However, a combined virtual-experimental approach offers a number of advantages as compared to bench testing only. The next sections give a literature overview of the main findings resulting from bench tests and provide an introduction to finite element stent analysis.

1.3.1 Bench testing

Many of the current insights in bifurcation stenting are based on the results of bench (or in-vitro) testing. A number of groups have been active in this domain but Dr. Ormiston and his co-workers (Mercy Hospital, Auckland, New Zealand) can be considered the leading experts as they have published numerous bench testing papers during the last decade [6, 75, 87–89]. They studied several bifurcation stenting techniques and compared different standard and dedicated stents. Some of their methods and results will be shortly mentioned in the following paragraphs but the interested reader is referred to the original papers for more details.

1.3.1.1 Bench testing techniques

Briefly, bench testing of bifurcation stenting involves the deployment of one or more stents within an in-vitro bifurcation model and visualization of the resulting lumen, stent deformations, strut coverage and/or positioning. Based on these observations, the techniques can be modified and guidelines can be formulated regarding stent choice and procedural parameters such as inflation pressure, balloon size and inflation sequence. The basis of this

approach has remained unaltered since the first papers in 1999, but considerable progress has been made regarding the bifurcation model and the visualization, two crucial aspects of bench testing.

In the early days, photography was the main tool to visualize and analyse the bifurcation stenting techniques [87, 90], while nowadays, micro-Computed Tomography (micro-CT) has become the standard [6, 91, 92]. Micro-CT allows generating three dimensional reconstructions which can be used to examine the stents from different perspectives. Parts of the reconstructed geometry can be removed to improve the clarity and 'fly-through' movies can be created (Fig. 1.24). However, there are limitations to this approach as reported by Ormiston et al. [6]: micro-CT imaging and the related reconstruction are expensive and time-consuming. In addition, simultaneous visualization of the balloon, stent and bifurcation model proves to be extremely difficult due to the large density differences of the individual components. A last limitation is related to the fact that only the final stent configuration has been visualized up to now, although information of the evolution of the strut deformation with increasing pressure would be very useful. A dynamic movie of a deploying or deforming stent has not been created yet due to a number of reasons: (i) The object should perfectly maintain its shape and position during scanning, but has to rotate over 360°. This is much more complicated if the guide wire and balloon catheter are present. (ii) This would be very time-consuming since every frame would require a complete scan. (iii) During the transient expansion phase, it is sometimes not possible to get a stable stent geometry.

The first bifurcation models were completely rigid and the set-ups allowed to take the deformed stents out of the model [87, 90]. This was necessary since photographs were used for visualization. These rigid models have now been replaced by flexible silicone models, which lead to more realistic stent deformations. Until now, most bifurcation models had a planar structure except for the model created by Murasato [91]. In a simple way, he included the three-dimensional structure of the left main coronary artery bifurcation, by glueing silicone tubes on the outer surface of a cylinder with a diameter of 7.5 mm. But as stated by Murasato [91], the observations made in these in-vitro setups should be interpreted carefully, as they might not accurately represent the phenomena occurring in human atherosclerotic vessels.

1.3.1.2 Applications

The focus of the first bench testing papers was on stent deformation after dilatation through the side of the stent [44, 87, 90]. Such postdilatation may be required to improve the access to the SB but distorts the stent within the main vessel and compromises the MB lumen. MB redilatation or kissing balloon postdilatation almost completely restores the main lumen.

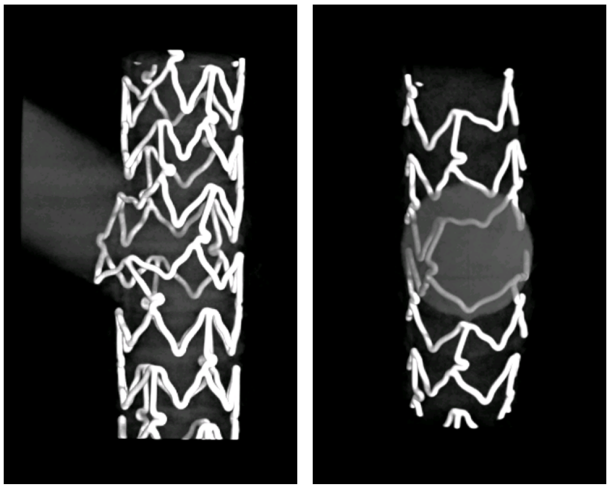

Figure 1.24: Micro-CT visualization of a Promus stent (Boston Scientific) after kissing balloon postdilatation. The left panel shows a top view on both branches of the bifurcation, while the right panel gives a view into the SB. The floating struts at the SB ostium are clearly visible after removal of the struts at the opposite MB wall.

The results of the two-stent bench studies also showed the importance of performing final kissing balloon inflation to improve the stent expansion and to correct distortion, regardless of the applied technique [6, 88, 89]. For the crush technique, better results were obtained after a two step kissing postdilatation as compared to a one step kissing postdilatation[6] [6]. The size of the stent cells is an important design parameter as a better expansion is obtained after both culotte and crush stenting when using stents with large cells [6, 89]. It should be stressed that clinical studies are required to assess whether or not these observations are clinically relevant.

1.3.2 Finite element analysis

Structural Finite Element Analysis (FEA) is a numerical technique used to virtually predict and investigate the mechanical behaviour of structures, such as cars, airplanes, mobile telephones and medical devices. Numerous software programs are available, both commercial and non-commercial, that perform FEA. The accuracy of the results obtained with these programs depends on the user input. For each simulation, a geometrical model has to be created and adequate material properties have to be assigned. In

[6] A two step kissing postdilatation starts with an additional high pressure balloon postdilatation in the SB followed by the standard simultaneous kissing inflation.

addition, realistic boundary and loading conditions have to be defined. FEA gives additional information as compared to physical tests and allows to study several 'What if?' scenarios addressing different materials, geometries and loading conditions before devices are actually manufactured [93]. This technique offers many advantages to investigate and compare currently used stents and stenting techniques, but also to develop new stents where it has the potential to reduce the time to market.

An extensive overview of the scientific literature regarding finite element stent modelling in the period 1999-2007 is given by De Beule [94]. This review clearly shows the considerable progress that has been made in this field during the last decade. Two of the most noteworthy advances are the use of more realistic arterial geometries and material models and the development of more accurate device models. Although many papers contributed to the current level of finite element stent modelling, some of the initially applied approximations proved to be inaccurate. For example, one of these inaccurate simplifications was to model the deployment of a balloon-expandable stent by neglecting the balloon and applying a direct pressure on the inner stent surface. This example clearly demonstrates the need to use FEA in conjunction with physical testing in order to verify the accuracy of the applied simplifications and to enhance the credibility of the obtained FEA results.

During the last few years, there has been a significant increase in the number of publications in the field of finite element stent analysis. More advanced simulation techniques have been introduced and these techniques have been applied to address a broad range of challenging research problems. Giving a complete overview of all the work done in this research domain, starting from 2008 till now, falls outside the scope of this thesis. However, a few papers have been selected and each of these is briefly summarized in the next paragraphs, mainly with the aim of illustrating the recent trends in the field of finite element stent modelling.

Wu et al. [95] nicely illustrated the potential of using topology optimization techniques by improving the design of a DES with drug reservoirs. The optimized design had an increased stiffness and resulted in lower stresses around the drug reservoirs while maintaining the volume of the reservoirs and thus the loading capacity. In addition, care was taken that the final optimized design was manufacturable.

Timmins and colleagues [96] studied the effects of varying stent design and atherosclerotic plaque stiffness on the vessel wall stresses and on the final lumen. The obtained results show that the stiffest design leads to a larger lumen, but also causes the highest stresses within the vessel wall. The difference in peak stress for the stiff and the less stiff stent was strongly dependent on the plaque stiffness. Increasing the plaque stiffness results in a more pronounced difference in peak stress. The authors conclude that

stent design is more important when dealing with a rigid, calcified lesion.

The work of Gijsen et al. [97] demonstrated the feasibility of using virtual stent expansions together with an in-vivo and patient based arterial model. The 3D reconstruction of the artery was obtained by combining angiography and IVUS as described in [98]. The simulation results reveal higher stresses in the arterial wall behind the stent struts and in the regions where the arterial wall was thin.

Finite element analysis is used to study many different aspects of stent implantations, but the final goal of the majority of the studies is to better understand stent mechanics in order to improve future stents and thus future clinical outcomes. Using finite element modelling to investigate and explain the results from completed clinical studies, as done by Zahedmanesh and Lally [99] is of course a very nice approach to improve our understanding of stent mechanics. They analyzed the two stents that were evaluated during the ISAR-STEREO trial [100], a clinical study that identified strut thickness as an independent predictor of in-stent restenosis (thinner struts results in a lower restenosis rate). The results obtained by Zahedmanesh and Lally support the hypothesis that arteries develop restenosis in response to injury and also confirm the importance of using computer simulations during the design phase of new stents.

The paper by Kouisis et al. [101] is a very nice example of how to combine experimental testing with numerical analysis. The authors developed an experimental setup that allowed to study the transient expansion of balloon-expandable stents. The obtained experimental data was first used to develop a finite element model to study this type of stents, and then also to validate the numerical results. The authors conclude that the finite element results are in satisfactory agreement with the experimental data.

Very recently, Gastaldi et al. [102] studied the provisional side branch approach. In particular, they investigated the impact of stent postioning on the stent deformations after side branch dilation through the side of the stent. For the studied closed cell stent design, the results clearly indicate the importance of a cell perfectly aligned with the side branch. This 'central' positioning results in a minimal obstruction of the side branch lumen and may therefore reduce hemodynamic disturbances. It should, however, be noted that the position of one cell with respect to the side branch can not be controlled with a single wire system.

1.3.3 Conclusions

FEA has proven to be a powerful technique to study the mechanical behaviour of stents. This technique also has the potential to provide new insights in the field of bifurcation stenting where bench testing is currently

the main investigation and development tool. Bench testing research contributed significantly to the current understanding of bifurcation stenting, but is limited to manufactured stents only. Furthermore, it requires the extensive use of advanced (expensive) visualization methods such as micro-CT. In contrast, postprocessing the FEA results is inexpensive and leads to a good (even dynamic) visualization of all components (e.g. balloon, stent and artery). Furthermore, different device and procedural parameters can be investigated prior to manufacturing. However, it should be stressed that FEA should be used in conjunction with a limited number of physical tests in order to assess the accuracy of the simulations and to enhance their credibility.

1.4 Aim of the doctoral research

The objective of this thesis is to develop and use advanced computational methods:

- to gain insights in the shortcomings of current stents and stenting techniques used to treat bifurcation lesions.
- to define optimal design parameters for a bifurcation stent.
- to provide guidelines to interventional cardiologists regarding stent selection.
- to virtually investigate and design new stents.

1.5 Organisation of the dissertation

The thesis is organised as follows:

- In chapter 2, a finite element model is described that allows to investigate the free expansion of balloon-expandable stents. This model is used to study and optimize the mechanical behaviour of this kind of stents.
- The most frequently applied bifurcation stenting technique is analysed in chapter 3 by using numerical analysis. The virtually observed stent deformations are compared to previously published bench testing results.
- A comparison of the impact of three different second generation drug-eluting stents when being implanted in the curved main branch of a coronary bifurcation is given in chapter 4. The advances with respect

to the modelling of coronary bifurcations (patient-specific morphology and anisotropic tissue properties) are described in detail.

- A quantitative analysis of the geometry of different stents is described in chapter 5.
- In chapter 6, we applied the developed simulation strategies to investigate the feasibility of a new dedicated bifurcation stent and a modified procedure for provisional stenting.
- Finally, chapter 7 gives an overview of the major findings of the research and contains some guidelines regarding stent design and selection. In addition, some suggestions for further research are included.

Chapter 2

Advances in finite element stent modelling

USING finite element simulations to study bifurcation stenting is not trivial. All the individual components (balloon, stent, bifurcation) have a complex geometry and undergo large deformations. These components also interact with each other, leading to a difficult contact problem. The presence of arterial tissue further complicates the simulations as this inhomogeneous multi-layered structure displays anistropic mechanical behaviour. For these reasons, it is important to go step by step instead of immediately jumping to full scale bifurcation stenting simulations. A first crucial step to study bifurcation stenting using finite element analysis is to develop validated models to study balloon-expandable stents as described in the first part of this chapter. The second part describes a novel methodology to develop discretized models for existing stents. This method was developed with the aim of reducing the amount of pre-processing[1].

---

[1] The contents of this chapter were published in the Journal of Biomechanical Engineering:
Numerical study of the uniformity of balloon-expandable stent deployment
P. Mortier, M. De Beule, S. G. Carlier, R. Van Impe, B. Verhegghe, and P. Verdonck
130:021018(1–7), 2008

and in the journal, Medical and Biological Engineering and Computing:
Automated generation of a finite element stent model
P. Mortier, M. De Beule, D. Van Loo, B. Masschaele, P. Verdonck, and B. Verhegghe
46:1169–1173, 2008

2.1 Uniformity of balloon-expandable stent deployment

2.1.1 Introduction

The major drawback of coronary stenting is restenosis, the reoccurrence of stenosis. This phenomenon is related to both arterial injury and an inflammatory response of the vessel wall against the stent struts. In the case of BMS, restenosis occurs in more than 20% of the treated artery sections [25,26,103]. This problem of renarrowing has been significantly reduced (to approximately 10% [104, 105]) by the introduction of DES. These promising results were recently shadowed by concerns regarding thrombogenicity and long-term outcomes [106]. In addition, 'real-world' cost-effectiveness analyses showed that DES might only be cost effective compared to BMS for elderly people and patients in specific high-risk groups [27]. Therefore, efforts aiming at reducing the arterial injury caused by stent implantations remain very meaningful.

Basically, vascular injury is due to a combination of stent-artery and balloon-artery interactions, both of which depend among other things on the stent design [107,108]. Examination of the patterns of endothelial damage shows a higher incidence of injured zones at the stent ends [33, 109]. This observation has been explained by Squire [33] as the result of three facts: (i) the stent expands in a nonuniform ends-first manner (dogboning), causing high local contact stresses, (ii) an axial contraction of the geometry during the stent expansion (foreshortening), and (iii) contact between the balloon, which is longer than the stent, and the artery.

Computer simulation (e.g., FEA) can be a very useful tool to study and optimize the stent expansion [110–113]. Several numerical studies discuss nonuniform stent expansion without simulating the balloon [114–116], although it has been experimentally shown by Squire [33] that nonuniform stent expansion is related to both stent design and balloon length. The same conclusion was drawn by Wang et al. [117] based on experiments and FEA. Their simulations were performed by using a cylindrical (nonfolded) balloon and were qualitatively validated. To the authors' knowledge, all the published numerical studies concerning stent expansions ignore the folding pattern of the balloon and, consequently, the impact of the folding pattern on the uniformity of the stent expansion remains unknown. Furthermore, dogboning has always been considered at one specific moment in time, although this phenomenon changes during the deployment of a stent.

Keeping the previous considerations in mind, the phenomenon of nonuniform stent expansion was numerically examined at each moment during the deployment. More precisely, the consequences of combining different realistic folded balloon catheters with a particular balloon-expandable coronary

stent were investigated. Catheters with different balloon lengths and folding patterns were used in the simulations and, consequently, this study allows choosing the optimal balloon catheter for this specific new generation stent design. Furthermore, the proposed methodology to obtain a uniform stent expansion by selecting the most favorable balloon can easily be applied to all balloon-expandable stents. Finally, attention has been paid to the impact of relatively small positioning inaccuracies during the crimping process on the expansion behavior. The crimping itself has not been incorporated in the simulations, as it has been shown by De Beule et al. [118] that including the crimping procedure has only a minor influence on the overall stent expansion behavior. The numerical results of a reference model were quantitatively validated by comparing the obtained pressure-diameter relationship with data provided by the manufacturer. In addition, the predicted deformations were also qualitatively compared to an experimental stent deployment.

2.1.2 Materials and methods

2.1.2.1 Balloon and stent geometry

The whole study is conducted on a three-dimensional stent geometry, resembling the Cypher stent (nominal length of 8 mm, nominal diameter of 3 mm; Cordis, Johnson & Johnson, Warren, NJ). The geometry of the stent, based on micro-computer-tomography images [119] was created using the graphical finite element preprocessor ABAQUS/CAE. The length, and inner and outer diameters of the crimped stent are 8.5 mm, 0.9 mm, and 1.2 mm, respectively. The resulting strut thickness of 0.15 mm is also confirmed by data provided by the manufacturer. The commercially available Cypher stent is crimped on a Raptor balloon (nominal diameter of 3 mm; Cordis), which is trifolded around the cylindrical catheter tube. This folding pattern was confirmed by the obtained micro-CT images. The catheter tube was included in the model as it interacts with the balloon during the unfolding process. The diameter of this tube is considered to be 0.6 mm. The cylindrical part of the balloon has a length of 10.5 mm, resulting in an overlength of 1 mm at both stent ends. Finally, the uniform balloon thickness is considered to be 0.02 mm.

2.1.2.2 Constitutive models

The Cypher stent is made of 316L stainless steel. Before stent expansion, the stainless steel stent struts are subjected to a range of manufacturing processes, which influence the constitutive response of the struts. Consequently, the material properties should ideally be obtained from tests performed on stent struts themselves. Therefore, the mechanical properties to describe the

inelastic behavior are based on the results published by Murphy et al. [120], who carried out tensile tests on similar stent struts. The impact of using such data instead of a more general constitutive law for 316L stainless steel is considerable [121]. The mechanical behavior is described using a Von Mises plasticity model with isotropic hardening. Young's modulus, Poisson's ratio, and the yield stress are 196000 N/mm^2, 0.3, and 375 N/mm^2, respectively [120].

The semicompliant Raptor balloon is fabricated from Duralyn, a nylon based material. The constitutive behavior of this material is based on a pressure/diameter relationship that is provided by the manufacturer for pressures higher than 0.2 N/mm^2. Values according to lower pressures were obtained by extrapolation, resulting in an initial diameter of 2.85 mm at the unpressurized state. The geometry of the trifolded balloon has been developed consistent with this initial diameter, the inner diameter of the stent, the balloon thickness, and the diameter of the cylindrical catheter tube. The methodology used to deduce the constitutive law of the balloon from pressure/diameter data is in accordance with the thin shell membrane theory [122] and results in stress/strain data, which are approximated by Young's modulus of 920 N/mm^2. In addition, the balloon material is characterized by a Poisson's ratio of 0.4.

These material properties have been numerically verified by expanding a cylindrical balloon (initial diameter of 2.85 mm) with tapered ends, as depicted in Fig. 6.2. Because of symmetry considerations, the computational time could be decreased by simulating only half of the balloon in the longitudinal direction. The application of a linear elastic constitutive model was satisfactory, as the maximum percentage difference in diameter between the original manufacturer's compliance chart and the numerical results is only 0.55% (at p=0.8 N/mm^2).

The third part of the stenting device, the catheter tube, is modeled as a rigid cylinder since the tube is relatively stiff compared to the balloon membrane. This approximation of reality is acceptable for the simulations undertaken in this work. In the case of flexibility tests, a more detailed constitutive model for the catheter tube would be required.

2.1.2.3 Boundary conditions

The tapered ends of the balloon are not taken into account in the folded balloon model. As a result, axial stresses (resulting from the pressure acting on the tapered ends in the longitudinal direction) have to be imposed to the folded balloon. This was done by applying a pressure dependent axial elongation to the balloon, starting from 0 mm (initial state) to 0.043 mm at a pressure of 1.5 N/mm^2. These values are valid for the 10.5 mm balloon and are obtained from the numerical expansion of the cylindrical balloon

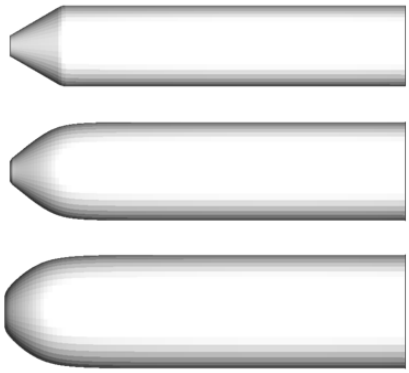

Figure 2.1: Numerical inflation of a cylindrical balloon (only half of the balloon was simulated because of symmetry).

model, which was described above. Adapted values have been used for every balloon length as these axial elongations are balloon length dependent. In order to avoid rigid body motion of the stent, six central nodes lying in the midsection are constrained in both longitudinal and tangential directions. Finally, the catheter tube is completely constrained in all directions.

2.1.2.4 Discretization

The stent geometry was meshed with 30112 linear eight-node hexahedral elements (C3D8R) using the preprocessing capabilities within ABAQUS/-CAE. The regions of the stent geometry subjected to minor deformations during the stent expansion were meshed with larger elements. The trifolded balloon (with a length equal to 10.5 mm) consists of 58386 four-node quadrilateral membrane elements (M3D4R), but this number varies depending on the balloon length and the folding pattern. The catheter tube was modeled with 3410 four-node bilinear rigid quadrilateral elements (R3D4). Further mesh refinements were unnecessary, since the radial displacements obtained with a higher number of elements (i.e., stent: 53655, balloon: 103950, and catheter: 7040 elements) changed less than 1%. A part of the meshed stenting device is visualized in Fig. 2.2.

2.1.2.5 Finite element simulations

All the stent expansion simulations were carried out using the ABAQUS finite element package. In particular, the ABAQUS/EXPLICIT solver was used for the highly nonlinear calculations, which additionally involve a complex (self-)contact problem. The general contact algorithm has been used

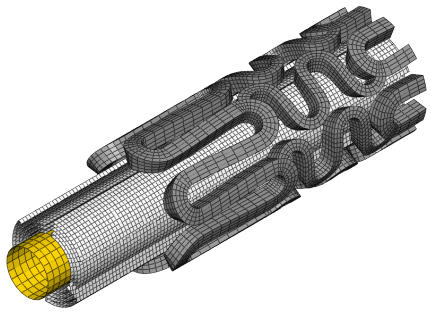

Figure 2.2: Meshed section of the balloon-catheter-stent model.

in order to handle the interactions between the balloon, the catheter tube, and the stent. Friction has been included in the simulations by means of a Coulomb friction model with a static friction coefficient of 0.2 (valid for both nylon-nylon and nylon-steel interactions under clean conditions).

The time period of the quasi-static stent expansion process has been decreased with the aim of reducing the computational time. The main problem is that as the event is accelerated, the presence of inertial forces may modify the response of the system. Energies were monitored during the stent expansion in order to assure that the inertial forces were acceptable. During most of the expansion process, the ratio of kinetic to internal energy of the whole model was less than 5%. Only during the short transition period between the crimped and the expanded state the ratio was slightly higher and a maximum of 8% was reached.

Several numerical simulations have been carried out to investigate the impact of combining different realistic balloon catheters with the Cypher stent geometry. The simulation, which incorporates the correct balloon length (i.e., 10.5 mm) and folding pattern (i.e., trifolded), was compared to the pressure-diameter relationship provided by the manufacturer and is termed reference simulation. In addition, a qualitative validation was performed by comparing the reference simulation with the experimental deployment of one Cypher stent which was visualized using micro-CT. The obtained results from this reference simulation served as a basis for the analysis of subsequent numerical calculations (see Table 2.1).

Simulations A-J concentrated on the influence of the balloon length on the uniformity of the stent expansion, while keeping the folding pattern of the balloon. Then, Simulation K was carried out to examine the influence of altering the folded shape from a trifolded to a sixfolded balloon, as shown in Fig. 2.3. In accordance with the trifolded balloon, the sixfolded balloon has been developed consistent with the initial balloon diameter, the stent inner diameter, the balloon thickness, and the diameter of the cylindrical

Table 2.1: Overview of the different models and their characteristics. Axial stent position refers to the position of the stent on the balloon catheter.

Simulation	Balloon length [mm]	Folding pattern	Axial stent position
Reference	10.5	trifold	central
A	10.3	trifold	central
B	10.1	trifold	central
C	9.9	trifold	central
D	9.7	trifold	central
E	9.5	trifold	central
F	9.3	trifold	central
G	9.1	trifold	central
H	8.9	trifold	central
I	8.7	trifold	central
J	8.5	trifold	central
K	10.5	sixfold	central
L	10.5	trifold	non-central
M	10.5	sixfold	non-central

catheter tube. Finally, the influence of positioning inaccuracies was studied in Simulations L and M by axially translating the previously centrally placed stent over 0.1 mm. All finite element simulations were carried out on an in-house built low-cost, high performance computing cluster. With the aim of quantifying the uniformity of the stent expansion during inflation, the following dogboning (DB) and asymmetry (AS) coefficients are introduced:

$$\mathsf{DB} = \frac{\mathsf{R}_{\text{max(distal,proximal)}} - \mathsf{R}_{\text{central}}}{\mathsf{R}_{\text{max(distal,proximal)}}} \tag{2.1}$$

$$\mathsf{AS} = \frac{\mathsf{R}_{\text{max(distal,proximal)}} - \mathsf{R}_{\text{min(distal,proximal)}}}{\mathsf{R}_{\text{max(distal,proximal)}}} \tag{2.2}$$

$\mathsf{R}_{\text{max(distal,proximal)}}$ and $\mathsf{R}_{\text{min(distal,proximal)}}$ stand, respectively, for the maximal and the minimal value of the two end radii of the stent measured at the inner surface at a specific moment during the inflation. This can be the distal or the proximal radius. This distinction is necessary as the stent ends may not have the same radii at the same moment during the stent expansion. $\mathsf{R}_{\text{central}}$ is the inner radius of the stent midsection.

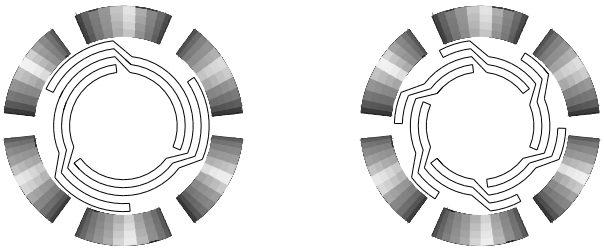

Figure 2.3: Comparison of a trifolded (left) and a sixfolded (right) balloon. Both folding patterns are based on the same initial balloon diameter, namely, $D_o = 2.85\,\mathrm{mm}$.

2.1.3 Results and discussion

2.1.3.1 Validation of the reference model

The expansion of the reference model is shown in Fig. 2.4. The stent deploys in a nonuniform ends-first manner (dogboning) as depicted in the central panel of Fig. 2.4. The bottom panel shows the stent configuration, which is reached at a pressure of $1.5\,\mathrm{N/mm^2}$. The results of this reference simulation are quantitatively validated through comparison with data provided by the manufacturer. In particular, the relation between the central inner diameter and the applied pressure is considered (compliance chart) as the companies always deliver such a chart for balloon-expandable stents (Fig. 2.5). The maximum percent difference in diameter occurs at a pressure of $1.4\,\mathrm{N/mm^2}$ and is an underestimation of 4% compared to the manufacturer data. Consequently, our model corresponds well to the provided compliance chart and serves as a solid, validated basis for further parametric studies.

In addition to the good quantitative agreement with the manufacturer data, the simulation results correspond well with the qualitative experiment during which the deployment of the Cypher stent was visualized using micro-CT (see Fig. 2.6). Furthermore, the specific deployment pattern in the low pressure range (i.e., the rapid increase in stent diameter when the inflating pressure reaches a certain value) and the dogbone shape were also observed experimentally.

2.1.3.2 Influence of the balloon length

The stent geometry during the transient expansion phase for Simulations E and J and the reference model is shown in Fig. 2.7. In contrast to the reference simulation, stent Model J with the shorter balloon length (8.5 mm) does not open in an ends-first manner. For the Model E with the intermediate balloon length, the diameters of the stent ends during the transient phase

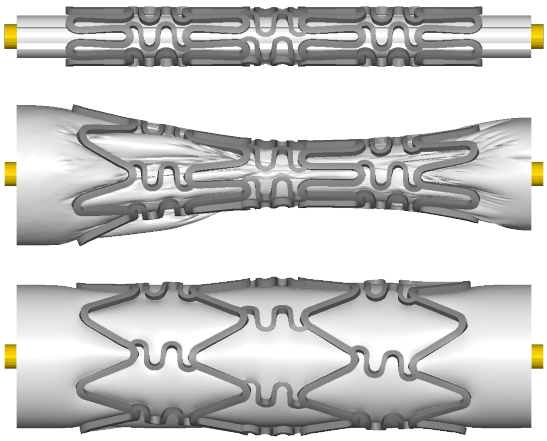

Figure 2.4: Expansion of the reference model (trifolded balloon with a length of 10.5 mm): before inflation (top); transient phase (middle) corresponding to a pressure between 0.3 MPa and 0.4 MPa (during the transient expansion phase, the balloon unfolds and the stent diameter rapidly increases); situation after this transient expansion (pressure higher than 0.4 MPa, bottom).

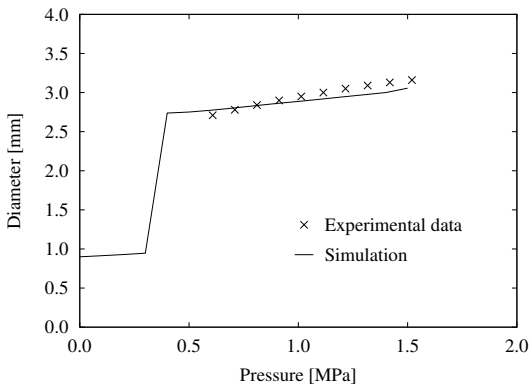

Figure 2.5: Quantitative validation of the reference model: the maximum percent difference in diameter between the numerical results and the compliance chart provided by the manufacturer is 4.1% and occurs at a pressure of 1.4 MPa. The steep part (pressure between 0.3 MPa and 0.4 MPa) of the curve obtained by simulation corresponds to the transient central shape from Fig. 2.4.

are only slightly larger than the central diameter, but this phenomenon is less pronounced compared to the reference model. The dogboning coefficient (whose value changes during the expansion of a stent) is an appropri-

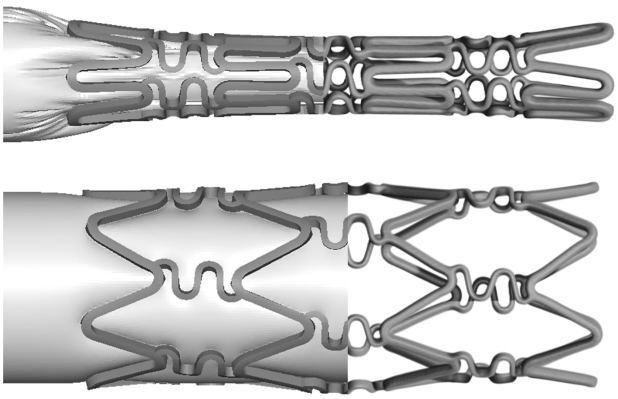

Figure 2.6: Qualitative validation of the Cypher stent expansion: the left side shows the virtually predicted deformations while the right part of the image displays the micro-CT visualization of the stent deployment.

ate parameter to quantify these observations. For the reference simulation, this coefficient is 0% at the start of the inflation (Fig. 2.4, top, cylindrical shape), reaches a maximum of 59% during the short transient expansion phase (Fig. 2.4, center) after which it decreases again, and finally becomes approximately 2% at high pressures (Fig. 2.4, bottom, cylindrical shape). In order to obtain a uniform stent deployment, the maximum value of this dogboning coefficient during inflation should be kept as low as possible. Therefore, these maxima have also been determined for models A-J and are visualized in Fig. 2.8, which shows a strong relation between the balloon length and the maximum observed dogboning coefficient during the different stent expansions. These results can be used to determine the maximum balloon length that should be combined with a particular stent design in order to avoid dogboning.

Wang et al. [117] have also investigated the relationship between balloon length and dogboning by finite element modeling. However, they apply an increasing pressure on the stent by using a cylindrical balloon with 'virtual' material properties. The accuracy of this approximation is still unknown, as the validation is purely qualitative, whereas the model proposed here has been quantitatively validated. Furthermore, examining the impact of using a different number of folds is not possible when discarding the folding pattern. Nevertheless, this approach remains interesting for balloon length investigation because the computational effort can be reduced.

Besides the impact of the balloon length on the vascular injury by dogboning, the balloon itself can cause endothelial damage by direct balloon-artery interactions [33, 108]. As a result, the balloon overlength should be reduced in order to decrease the balloon-artery contact area at the stent ends. Luck-

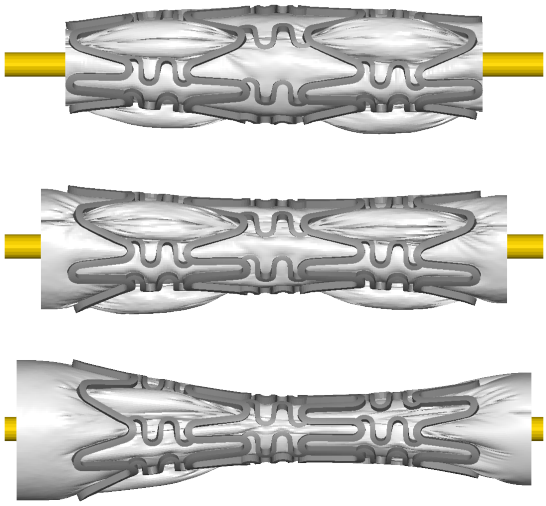

Figure 2.7: Transient expansion shape for Model J (top), Model E (center), and the reference model (bottom). A shorter balloon length results in a decreased dogbone effect.

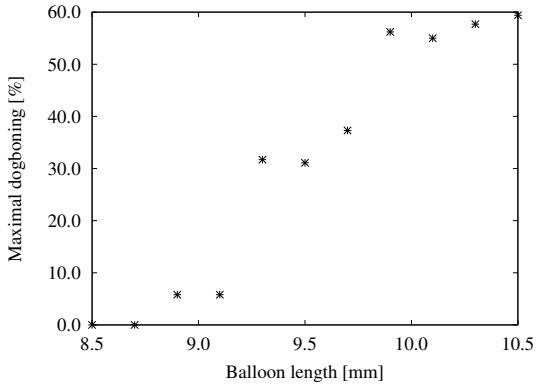

Figure 2.8: Relationship between the balloon length and the maximal dogboning coefficient during the transient expansion phase. A more uniform expansion is obtained by decreasing the balloon length.

ily, these two causes of vascular injury (dogboning and balloon-artery contact) result in the same guideline for the balloon length, namely, that this length should be kept as small as possible. If a reduction in the balloon length fails to eliminate dogboning, the stent geometry should be modified, as dogboning also depends on this geometry [114–117]. In particular, the

stiffness of the stent ends has to be increased. However, too large an increase will result in an opposite (unwanted) effect (i.e., larger diameter of the central part of the stent compared to the diameter of the stent ends). Therefore, the modification of the stiffness should be done with great care.

2.1.3.3 Influence of the folding pattern

A comparison of the results from the reference model with those obtained from Simulation K is shown in Fig. 2.9. This comparison allows the identification of the impact of the folding pattern, as all the other variable parameters (e.g., balloon length) remain unchanged. During the transient stent expansion, one can observe that the balloon bulges out through some of the stent openings. As can be seen in Fig. 2.9 (left panel), the trifolded balloon results in large balloon protrusions in three of the six stent cells in that cross section. These strongly protruding parts of the balloon cause larger stent openings at these locations, leading to a nonuniform stent strut distribution (the maximal angle between two struts is 71 degrees while a uniform strut distribution corresponds with an angle of 60 degrees). This nonuniform behaviour was also observed experimentally with micro-CT at the end of the transient expansion phase (see Fig. 2.9, central panel). As the number of balloon protrusion (3) corresponds with the number of balloon folds (3), one should expect that using a sixfolded balloon would result in a more uniform strut distribution. Indeed, a finite element simulation was conducted using a sixfolded balloon and a uniform strut distribution was obtained. This may be an important finding as the uniformity of the strut distribution affects the tissue scaffolding and the drug delivery in case of DES.

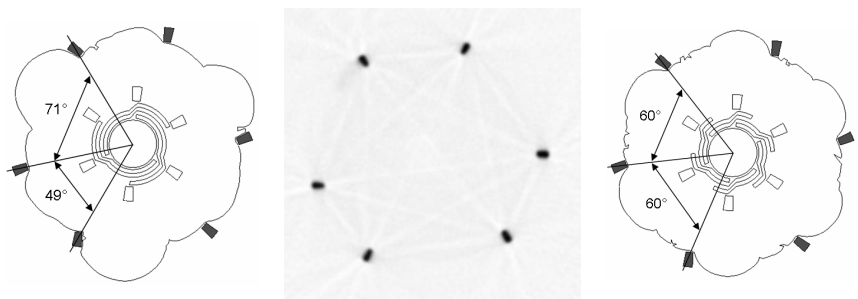

Figure 2.9: Cross section at the end of the transient expansion phase, showing that a trifolded balloon causes a nonuniform strut distribution (left panel: simulation; center panel: experiment), whereas a sixfolded balloon (right panel: simulation) results in a homogeneous strut placement.

2.1.3.4 Influence of small positioning inaccuracies

The results of Models L and M are shown in Fig. 2.10. Moving the stent over a small distance (i.e., 0.1 mm) in the longitudinal direction results in a totally different deployment pattern during the transient phase. Such an axial translation can be due to positioning inaccuracies during the crimping process. The stent end corresponding to the longest free balloon end opens first, because at that end, the same pressure acts on a larger balloon surface. Results are summarized in Table 2.2 in terms of dogboning coefficients and coefficients of asymmetry. The coefficient of asymmetry is strongly related to the position of the stent on the balloon catheter. For the trifolded balloon, the already existing asymmetric expansion of a centrally placed stent is reinforced by a small axial translation of the stent (coefficient changes from 34% to 64%). This difference is more pronounced in the case of a six-folded balloon. A central stent position causes an approximately symmetric deployment (7%), while a noncentral placement leads to severe asymmetry (47%). Consequently, minor positioning inaccuracies of the stent should be avoided, as this leads to asymmetric stent expansions. In the future, more advanced computer models taking into account the exact stent geometry and incorporating the balloon ends could be used to tune manufacturing processes. More precisely, for a given balloon-stent combination and an allowed asymmetric expansion value, the maximum balloon eccentricity could be calculated.

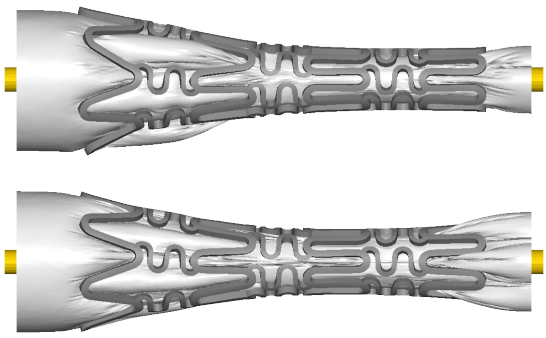

Figure 2.10: Transient expansion shape for Models L and M. A noncentrally placed stent results for both folding patterns in a strongly asymmetric expansion.

2.1.4 Limitations

In this study, the balloon ends were discarded from the model. Creating a balloon model that takes into account both the folding pattern and the

Table 2.2: Influence of small positioning inaccuracies on the uniformity of the expansion.

Simulation	Folding pattern	Axial stent position	DB (%)	AS (%)
Reference	trifold	central	59	34
K	sixfold	central	54	7
L	trifold	non-central	60	64
M	sixfold	non-central	58	47

balloon ends is a complex problem. Possible ways to overcome this limitation is to directly use a CT based 3D reconstruction of the folded balloon or to create the folded geometry by applied a coordinate transformation on the nodal coordinates of an unfolded balloon as proposed by Laroche et al. [123].

It has been shown that the longitudinal position of the stent on the balloon catheter has a considerable impact on the symmetry of the expansion, but the clinical consequences of this observation are still unknown. Therefore, future numerical models will incorporate the artery and this will allow to study the resulting stresses in the vessel wall. Including the artery in the simulation models can also be useful to investigate the impact of the presence of the artery on the obtained stent diameters, since it has been observed using intravascular ultrasound that in clinical practice, the stents will only reach on average 75% of the predicted diameter [124], as a consequence of complex interactions with the atherosclerotic plaque forming the coronary stenosis.

2.1.5 Conclusions

The proposed stent modeling strategy incorporates the folding pattern of the balloon. This approach results in a very close quantitative agreement of our results and the manufacturers' compliance chart. The model also shows good qualitative agreement with the experimentally observed stent deployment. This validated numerical model has been used as a basis for further investigation of several parameters, such as balloon length, folding pattern, and relative position of stent with respect to the balloon catheter. It was shown that changing these parameters can have an enormous influence on the transient stent expansion behavior. Therefore, the proposed methodology can be used to select the most appropriate balloon length and folding pattern for a particular stent design. Furthermore, it has been shown that small positioning inaccuracies (e.g., during the crimping process) can considerably modify the stent deployment. Consequently, the positioning of

the stent on the balloon catheter should be done with the greatest care and accuracy.

2.2 Automation of pre-processing

2.2.1 Introduction

The applicability of the current finite element stent models is restricted by the required amount of preprocessing and computational effort, which is significant. As a result, there is a continuous need to reduce the time cost of the complete process, from stent sample to simulation. This can be done by using acceptable model simplifications, such as the one proposed by Hall and Kasper [125]. They have shown that approximating the stent geometries with beam elements yields acceptable results when studying the global stent stress state after expansion and considerably decreases the computational time.

In addition to the computational cost, there is a considerable effort needed to obtain accurate finite element meshes (beam and/or solid) starting from existing stent geometries. The commonly used procedure involves different manual time-consuming steps: (1) determination of the stent dimensions, (2) creation of the 3D CAD model, and (3) mesh generation [112, 115, 126, 127] (Fig. 2.11). Furthermore, this procedure may fail to accurately replicate existing stent designs, because nonuniform deformations resulting from the crimping process (i.e., a fixation of the stent on a folded angioplasty balloon by reducing its diameter) are not taken into account.

Therefore, we investigated the feasibility of a novel strategy to create meshed stent models for finite element analysis starting from stent samples in a semi-automated way. The method is based on automatic centerline extraction from a triangulated surface and yields a beam mesh accurately representing the stent geometry. Such a triangulated surface is obtained from micro-CT images after segmentation and 3D reconstruction. Micro-CT reconstruction of stent geometries has been used in the past [128]. However, these works were related to computational fluid dynamics and a method to create a suitable mesh for finite element analysis starting from a reconstructed stent has not been proposed yet. The feasibility and time-effectiveness of the proposed methodology is demonstrated for the MULTI-LINK Vision stent.

2.2.2 Materials and methods

The micro-CT setup used for this investigation consists of a Feinfocus X-ray tube with beryllium exit window, a sample manipulator with air bearing rotation stage and a Varian Paxscan 2520 V X-ray flat panel detector [129].

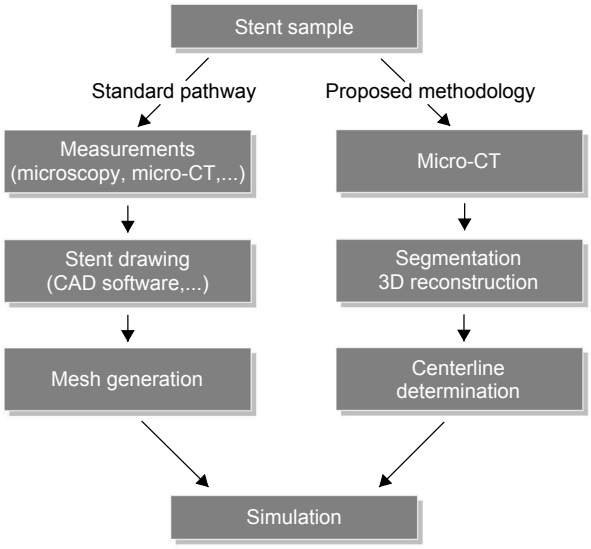

Figure 2.11: Two different strategies can be used to obtain a finite element mesh starting from a stent sample. The left pathway illustrates the previously used methodology, which involves several manual steps. The different steps of the alternative (semi-automated) strategy presented here are shown in the right pathway.

For the measurements we used the X-ray tube at 80 kV and 2.7 W which results in a focal spot size of 3 µm. The detector was used in binning mode with a pixel size of 254 µm. The field of view of the detector is 200 mm (width) by 160 mm (height). The distance between the source and the detector was 880 mm and the distance between the center of the stent and the X-ray source was 36 mm. This geometry results in a magnification of 24 times and a CT voxel size of 10.6 µm. The total scan time was 6 min for 900 projection images.

For this study, one commercially available stent was selected and scanned in its crimped state: the MULTI-LINK Vision (nominal diameter 3 mm, nominal length 8 mm, Abbott Vascular). The CT reconstruction was conducted with OCTOPUS software[2]. Mimics (Materialise, Leuven, Belgium) was used for the segmentation and 3D reconstruction[3]. The software package uses simple gray-value thresholding on the CT-slices in order to obtain a 3D mask of the object of interest. This mask could be considered as a large 3D matrix with Boolean values in each of its element, determining

[2] http://www.xraylab.com

[3] http://www.materialise.com/mimics

whether the element is part of the virtual object or not. This mask is then used to derive a triangulated mesh which is further processed by triangle reduction and smoothing operations using MAGICS (Materialise, Leuven, Belgium), the integrated remeshing feature of MIMICS.

An approximated centerline was determined starting from the triangulated surface using pyFormex, open-source software currently under development at our institution [130]. The main steps in the applied centerline algorithm are:

1. Calculation of the Delaunay tessellation [131].
2. Calculation of the embedded Voronoi diagram [131].
3. For each Voronoi vertex (i.e., the circumcenter of a Delaunay tetrahedron), the radius of the corresponding Voronoi sphere is computed.
4. The Voronoi vertex with the largest corresponding radius is added to a new list and all Voronoi vertices within this Voronoi sphere are deleted. This is repeated until all Voronoi vertices are deleted. The result is a subset of the original list of Voronoi vertices.
5. Two Voronoi vertices from the subset are connected if the distance between these two vertices is smaller then the sum of their corresponding radii.

The resulting centerline consists of connected line segments, that can directly serve as a finite element beam mesh. The beam section can be estimated from the triangulated surface. A flow chart of the complete process is depicted in Fig. 2.11.

The MULTI-LINK Vision stent was virtually expanded using both the standard pathway and the new approach (based on the centerline calculation) in order to verify the accuracy of the new method. The simulations were performed with the ABAQUS finite element solver (Dassault Systèmes). The two beam models were deployed to a 3 mm diameter by increasing the radius of a rigid cylinder [126]. The foreshorting, defined as $\frac{(l_o - l)}{l_o}$, was calculated for both stent models (l_o is the stent length in crimped state, l is the stent length in expanded state).

2.2.3 Results and discussion

The resulting finite element beam mesh (or centerline) is depicted in Fig. 2.12 (bottom panel) and was obtained from the surface mesh containing 171110 triangles within few minutes on a standard desktop computer (2 Ghz processor). The mesh consists of 2268 beam elements and accurately resembles the MULTI-LINK Vision stent geometry. This mesh can be used to

simulate the stent expansion and/or to investigate the mechanical behaviour of the stent [125, 132].

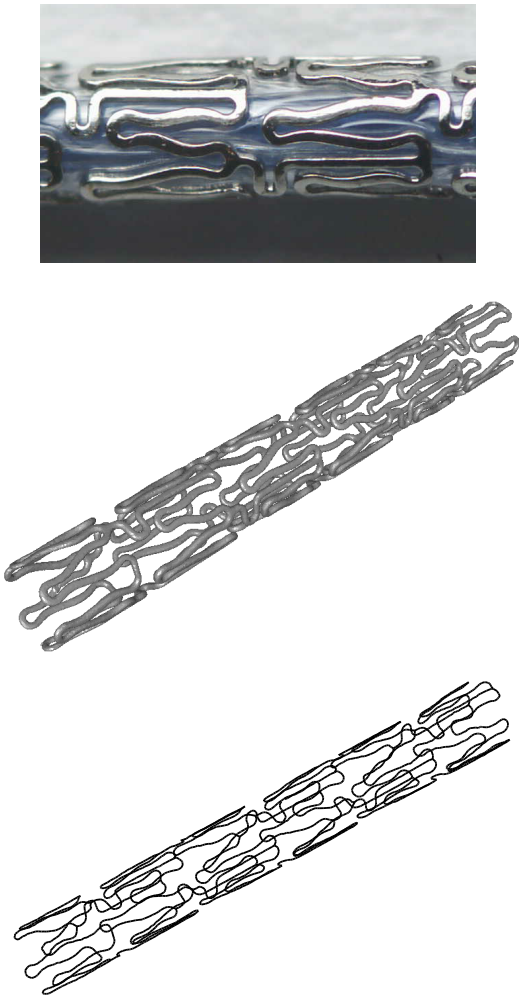

Figure 2.12: The top panel shows a photograph of the stent. The surface mesh obtained after segmentation of the CT-images is shown in the middle panel. The resulting finite element beam mesh obtained by centerline determination is depicted in the bottom panel.

Figure 2.13 shows the comparison between two virtually deployed MULTI-LINK Vision stents. The simulation based on the traditional approach (2046 beam elements) is depicted in panel A, whereas the beam mesh in panel B is based on the new approach involving the centerline computation. The

expanded stent geometries are very similar and this is also quantitatively reflected by the foreshortening, which is identical in both cases (i.e., 2.5%). Consequently, the beam mesh obtained by calculating the centerline seems an accurate alternative to a traditionally created beam mesh.

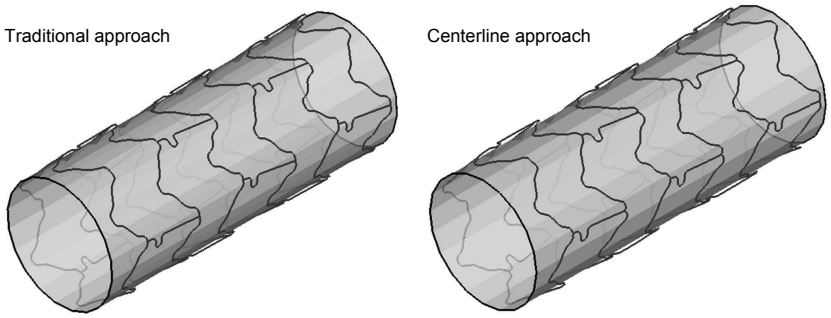

Figure 2.13: Comparison of the simulation results using two different methods to create the stent geometry. The simulation based on the traditional approach is depicted in the left panel, whereas the beam mesh in the right panel is based on the new approach involving the centerline computation.

Although the finite element beam mesh is automatically created from a triangulated surface, a certain amount of manual work is still required to obtain this surface mesh starting from a stent sample. This manual work is necessary to prepare the micro-CT setup (positioning of the sample) and to segment the images (e.g., choice of threshold and visual check of the obtained surface mesh). Nevertheless, this method assures an accurate representation of the investigated stent geometry, including the inhomogeneous deformations resulting from the crimping process. Furthermore, this approach may allow creating solid meshes in a semi-automated manner by sweeping the mesh along the centerline. Such a solid mesh may be required for very detailed stress analyses.

The triangulated surface depends on the threshold used during the segmentation process. Using a lower or higher threshold value may slightly modify the estimated strut cross-section. Using images with a voxel size of 10.6 µm, this means that the stent strut is approximately 20 µm smaller if 2 voxels are removed by using a different threshold, which is important for a stent with struts of approximately 80 µm. However, the impact of the applied threshold on the resulting centerline will be small on condition that the surface mesh is not connected at locations where two separate struts come close to each other (Fig. 2.14). A second micro-CT scan was performed using a higher resolution (CT voxel size of 1.05 µm) in order to obtain a more accurate estimate of the strut cross-section (see Fig. 2.15), which is required for the definition of the beam elements. Using this high resolution, only a small portion of the stent could be scanned.

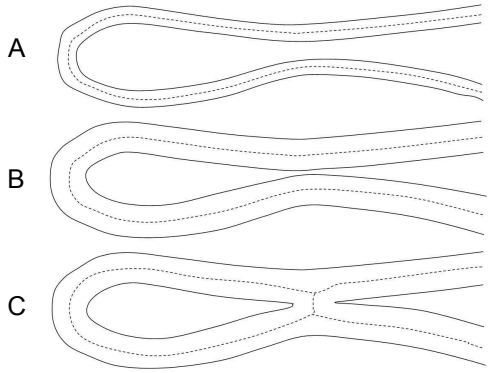

Figure 2.14: A and B: The same stent geometry using a different segmentation threshold. The resulting centerline in both cases is almost identical and therefore, the applied threshold has a limited impact on the resulting centerline. However, the centerline can be modified by the segmentation threshold in case that the reconstructed stent geometry contains connections between different struts which are not connected in reality (C).

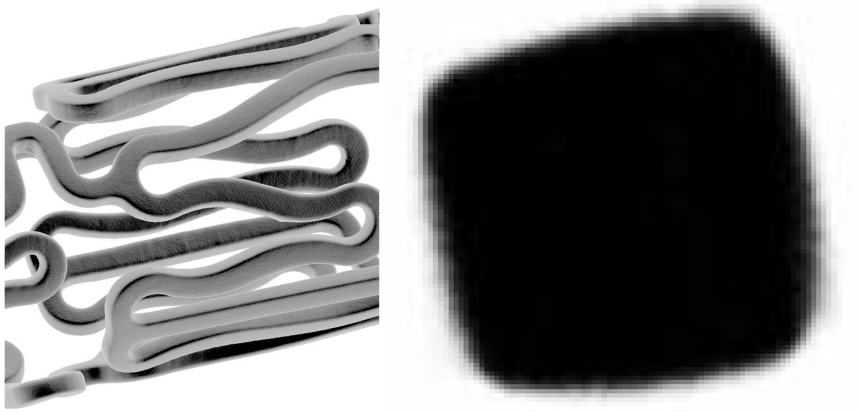

Figure 2.15: A second micro-CT scan was performed using a higher resolution (CT voxel size of 1.05 µm) in order to obtain a more accurate estimate for the strut cross-section (see right panel). Only a small portion of the stent was scanned at this resolution.

A limitation of the proposed approach is that the size of the elements of the finite element beam mesh is determined by the centerline algorithm and is independent of the curvature of the stent struts. However, it may be necessary to have more elements in regions of sharp geometry transitions.

Furthermore, it should be emphasized that the developed strategy is meant

to create a finite element mesh of existing stent designs in order to compare their mechanical behavior. The method does not provide the possibility for parametric modeling, which is useful during the design phase of new devices [94]. It is mainly because of this reason that parametric stent meshes were created using the traditional approach for the studies described in the remaining chapters.

2.2.4 Conclusion

Studying the mechanical behavior of current stenting devices by using finite element simulations is sometimes time-consuming, partially because the different manual steps that occur during the preprocessing phase. We developed a new methodology to automate the process of generating a finite element beam mesh starting from a stent sample. The proposed strategy is time-effective and results in a beam mesh, accurately representing the investigated stent geometry.

Chapter 3

Accuracy of finite element analysis of side branch access during provisional stenting

THE developed methodologies to simulate the mechanical behaviour of balloon-expandable stents can now be applied in the field of bifurcation stenting. The main goal of this chapter is to prove the feasibility of using finite element analysis in this domain by comparing the numerical results with previous bench test observations[1].

3.1 Introduction

Stenting the MB only (often referred to as provisional stenting) is currently the preferred strategy to treat bifurcation lesions as stenting both branches applying a complex technique seems to offer no advantages [5, 40, 58]. This approach offers the possibility of placing a second stent in the SB in case of suboptimal results (e.g., T-stenting). Provisional stenting compromises the access to the SB due to obstructing stent struts. Balloon dilatation through the side of the MB stent can improve the SB patency (Fig. 3.1).

---

[1] The contents of this chapter were published in the journal, Medical Engineering and Physics:
Finite element analysis of side branch access during bifurcation stenting
P. Mortier, M. De Beule, D. Van Loo, B. Verhegghe, and P. Verdonck
31:434–440, 2009

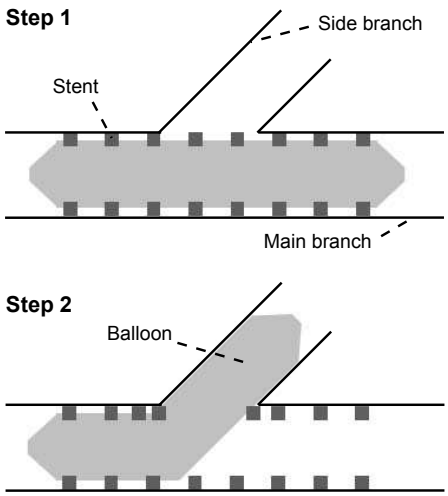

Figure 3.1: Concept of SB balloon dilatation through the MB stent.

Ormiston et al. [87] performed in vitro experiments in order to study the stent deformations following to SB dilatation. They have shown that such a balloon inflation results in unwanted distortions of the stent, compromising the downstream MB lumen. Their results also evidenced the need for final kissing balloon inflation (i.e., simultaneous dilatation of MB and SB) or MB redilatation. These in vitro tests require a large number of (expensive) stent samples. Even more stents will be needed to investigate other, more complex techniques, involving two or three stents, such as the crush technique, culotte stenting, etc. This may explain the scarcity of in vitro studies in the domain of bifurcation stenting. Therefore, computer models addressing these complex stenting techniques may be a valuable research tool complementing experimental studies. Numerical models have already proven to be a useful tool to investigate the free expansion [94,115,126,127] and the fracture behaviour [133] of these devices, but also to study the supraphysiological loading state in the arterial wall after stent implantation [112,113,132,134]. Using numerical models to study bifurcation stenting may also help in this specific field to understand the shortcomings of current clinical techniques and devices.

Therefore, an innovative simulation strategy is described to study SB balloon dilatation through a stent implanted in the MB. The proposed methodology incorporates the interactions between balloon, stent and arterial wall, and also the nonlinear material behaviour of the artery is taken into account. The value of the described model is in its ability to compare different balloon-stent combinations. This is illustrated by investigating the impact

of using two different balloon sizes (2.5 and 3 mm) and two commercially available stent designs (Cypher and MULTI-LINK Vision) on the stent cell deformation and on the global stent distortion. The deformed stent cells are quantitatively analysed in order to allow easy comparison between the different balloon-stent combinations. The proposed computer model provides a useful tool for stent designers to create dedicated bifurcation stents and may help clinicians to choose the optimal balloon size and stent design.

3.2 Materials and methods

3.2.1 Geometry

For this study, two commercially available stents were selected: the Cypher (nominal diameter 3 mm, nominal length 8 mm, Cordis, Johnson & Johnson) and the MULTI-LINK Vision (nominal diameter 3 mm, nominal length 8 mm, Abbott Vascular) balloon-expandable stents. These nominal dimensions are provided by the manufacturers and should be obtained at a pressure of 10 atm (Cypher) or 9 atm (MULTI-LINK Vision). CT-images were used to determine the main stent dimensions and the 3D stent models were created based on these measurements (see Fig. 3.2). The length, inner diameter and strut thickness of the crimped Cypher stent are, respectively 8.5, 0.9 and 0.15 mm. For the MULTI-LINK Vision stent, these values are, respectively 7.9, 0.895 and 0.08 mm.

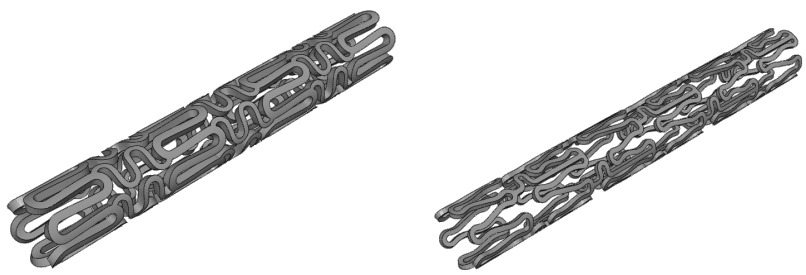

Figure 3.2: 3D model of Cypher (left) and MULTI-LINK Vision (right) stent.

The semi-compliant Raptor balloon catheters (Cordis, Johnson & Johnson) with nominal diameter 2.5 and 3 mm were used for the SB balloon dilatation. Micro-CT images clearly revealed the trifolded configuration of these commercially available balloon catheters [126]. Figure 3.3 shows the balloon catheters in an idealized folded configuration used for the simulations. These approximated folded balloon geometries are based on the initial diameters (i.e., at 0 MPa) which were obtained by extrapolation of

Table 3.1: Material properties for SS316L and L605 Co-Cr alloy.

Alloy	Young's modulus	Yield stress	Poisson's ratio
SS316L	196000 MPa	375 MPa	0.30
L605 Co-Cr	243000 MPa	629 MPa	0.35

the pressure-diameter data provided by the company (only available for pressures higher than 0.2 MPa). A uniform membrane thickness equal to 0.02 mm is assumed for both balloon catheters. Both folded configurations have an outer diameter of 0.88 mm.

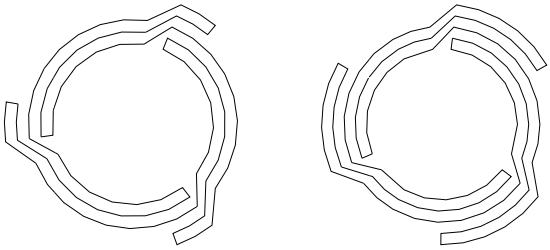

Figure 3.3: Geometrical models representing trifolded Raptor balloon catheters with a nominal diameter of 2.5 mm (left panel) and 3 mm (right panel).

The bifurcation geometry is determined by the angle of intersection, MB inner diameter, SB inner diameter and wall thickness, which was supposed to be uniform. These four parameters are, respectively 45°, 3, 2.5 and 0.5 mm.

3.2.2 Constitutive behaviour

The Cypher stent is laser-cut from a stainless steel 316L tube in contrast to the tubes used to manufacture the MULTI-LINK Vision stent that are made from L605 cobalt-chromium alloy. Material properties for these alloys were taken from literature [120, 135] and are summarized in Table 3.1.

The Raptor balloon catheters are made from Duralyn, a nylon-based material. Material properties for both balloon catheters were derived starting from the compliance data provided by the manufacturer. The followed approach is based on the thin shell membrane theory [122] and results in stress-strain data which are approximated by a Young's modulus of 600 and 920 MPa, for the 2.5 and 3 mm balloon catheter, respectively. The different Young's moduli are a result of the membrane thickness, which was considered to be the same for both balloon catheters. Poisson's ratio is set to

0.4. The compliance of both balloon catheters was validated by inflating a cylindrical balloon (with the same initial diameter as the one used for the folded configuration) with tapered ends and comparing the results in terms of pressure-diameter with the original compliance data. The arterial wall behaviour was modelled using a homogeneous isotropic hyperelastic law as described by Prendergast et al. [136].

3.2.3 Simulation details

During a first simulation step, a stent was expanded in the MB by enforcing a radial displacement to a cylindrical balloon until the cylinder reached a diameter of 3 mm. De Beule et al. [126] have shown that this expansion strategy yields good results to study free expanding stents in the high-pressure range. This approach was used to expand stents within a vessel in order to reduce the computational cost of the simulations. This seems a reasonable simplification because of the assumed cylindrical shape of the MB. Following to the expansion, the diameter of the cylindrical balloon was gradually decreased, allowing for a recoil phase. During a second step, a folded balloon was inflated (up to 1.5 MPa) while positioned in both the MB and SB, resulting in a distortion of the stent geometry. Finally, the pressure in the balloon was gradually removed. This procedure is illustrated in Fig. 3.4 and was repeated for both stent designs combined with the two different balloon sizes, resulting in four simulations.

The original stent positions were chosen in such a way that after stent deployment, the folded balloon passed through a stent cell while avoiding intersecting elements. For the MULTI-LINK Vision stent, such a configuration was not found and a local external pressure was applied prior to inflation on the outer balloon surface in order to avoid intersecting elements.

The ABAQUS/Explicit solver was used for the large deformation analyses, as this code provides a very stable contact algorithm (i.e., the general contact algorithm). All contacts were assumed to be frictionless. During the stent deployment in the MB, contact between the folded balloon (used for subsequent dilatation through the side of the stent) and any other part in the model was not taken into account. A similar technique was used for the second step, which involved the SB balloon dilatation, where the contact with the cylindrical tube (used for the stent expansion in the MB) was ignored. All other contact pairs were taken into account.

Inertia was assumed to have a negligible impact on both the stent expansion and the balloon inflation. Therefore, the expansion scenarios were considered to be quasi-static phenomena. A well established technique to reduce the required computational effort is to accelerate the process in comparison with the physical procedure. However, this approach could introduce unwanted dynamic effects and may change the response of the system. There-

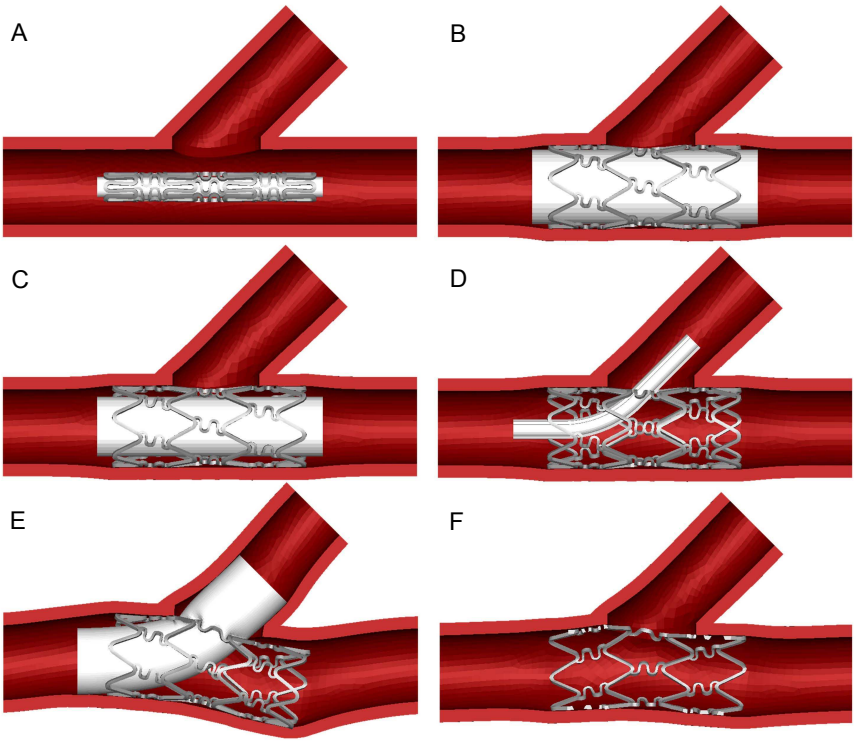

Figure 3.4: Illustration of the simulation procedure for the Cypher stent (panel A: initial configuration, panel B: fully expanded stent, panel C: stent configuration after recoil, panel D: initial position of the 2.5 mm SB balloon, panel E: deformed configuration at the maximum pressure of 1.5 MPa, panel F: final state after balloon deflation).

fore, energies were monitored during the simulations in order to assure that the inertial forces remained insignificant.

In order to avoid rigid body motions, the ends of all branches were constrained in both axial and tangential direction. Furthermore, pressure-dependent axial elongations were imposed to the balloon ends ranging from 0 mm(initial state) to 0.06 mm (2.5 mm balloon) or 0.035 mm (3 mm balloon) at a pressure of 1.5 N/mm^2, in order to account for the axial stresses which occur in a balloon with tapered ends. These axial elongations were obtained from the numerical expansion of the cylindrical balloon model (including the tapered ends), which was described above.

3.2.4 Postprocessing

In order to compare different stent designs and balloon sizes, operator independent criteria are required to assess the deformation of the stent. As the SB balloon dilatation aims to improve the SB patency a new parameter is introduced, the Projected Cell Area (PCA), which is related to the deformation of the stent cell through which the balloon is inflated (see Fig. 3.5). This stent cell is defined by a 3D curve and consequently, a projection is required for area calculations. The curve at the inner side of the stent cell was chosen for the PCA calculations as shown in Fig. 3.5. The curve projections and area calculations were performed using pyFormex, an in-house developed open source program [130]. Furthermore, the proposed projection direction also yields adequate results for stents that deploy partially within the SB without compromising the SB patency. A PCA that is greater than the circular area of the SB, means that the stent cells can be sufficiently enlarged by the employed balloon, but does not necessarily indicate optimal stent deformation.

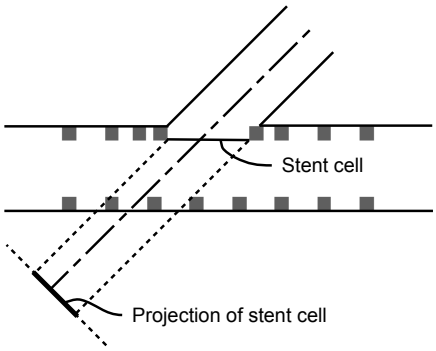

Figure 3.5: Schematic drawing illustrating the projection method used to calculate the Projected Cell Area (PCA).

3.2.5 Discretization

The finite element mesh of the Cypher and MULTI-LINK Vision stent consisted of 25992, respectively 29736 8-node hexahedral elements (C3D8R). The same element type was chosen for the arterial wall mesh, which contains 9561 hexahedrons. For the 2.5 mm balloon, 9858 4-node quadrilateral membrane elements (M3D4R) were used, whereas the 3 mm balloon was meshed with 12084 quadrilaterals. Finally, the cylindrical tube was also meshed with M3D4R elements (i.e., 6300).

A mesh sensitivity analysis was performed for the simulation of the Cypher stent, combined with the 2.5 mm balloon. Increasing the total number of elements with approximately fifty percent (79197 instead of 51711 elements) changed the resulting PCA after dilatation through the side of the stent with less then two percent. Therefore, mesh densities were considered acceptable for the analysis of the cell deformation.

3.3 Results and discussion

3.3.1 Validation of balloon models

The validation of the compliance behaviour of both balloons is depicted in Fig. 3.6. For the 2.5 mm balloon, the maximum percentage difference in diameter is less than four percent and occurs at a pressure of 1 MPa. The numerical results of the 3 mm balloon expansion differ less than one percent from the original data (i.e. at a pressure of 0.8 MPa). Both balloon models demonstrate realistic deformations under pressure and consequently, the linear elastic approximation of the stress-strain data seems justified.

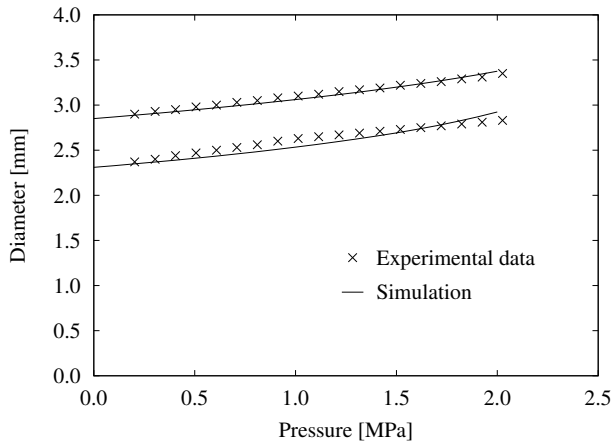

Figure 3.6: Comparison of the manufacturer data (crosses) with the simulation results (line).

3.3.2 Side branch access

Figure 3.7 shows the deformed stent geometries after deployment in the MB and after subsequent SB balloon dilatation. Inflating a balloon, positioned in both the MB and SB, through an already expanded stent clearly improves

the SB patency. Furthermore, such balloon inflation facilitates access to the SB through the stent struts. This is of major importance during T-stenting, a bifurcation stenting technique which involves the implantation of two stents, a first one in the MB and a second one in the SB.

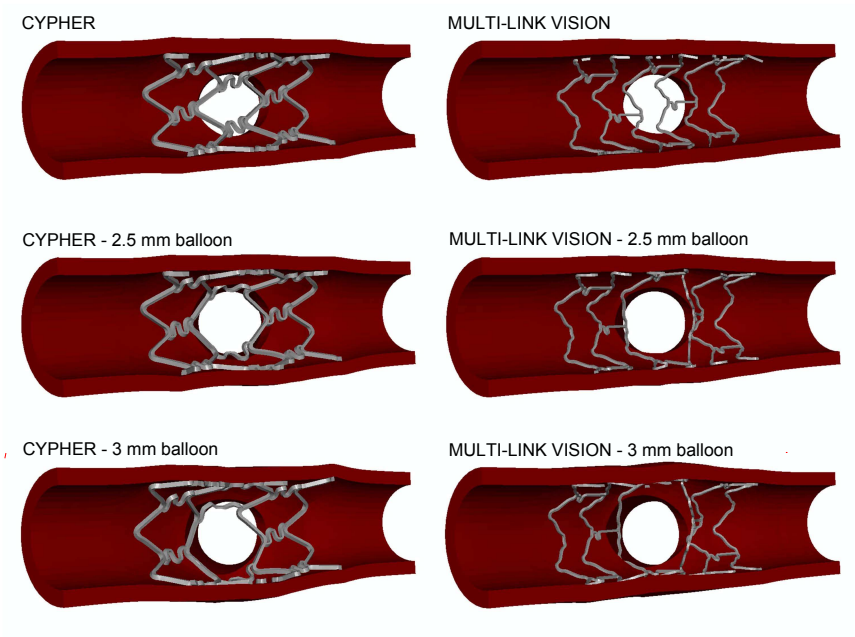

Figure 3.7: Stent distortion after expansion in the MB and following subsequent balloon dilatation through a stent side-hole. The stent opening in front of the SB considerably enlarges due to this balloon inflation and the effect depends on the balloon size.

The balloon inflation through a stent opening results in a significant enlargement of that stent opening and as intuitively expected, the largest opening is obtained by a 3 mm balloon dilatation. This effect is also quantitatively reflected by the previously introduced Projected Cell Area (see Table 3.2). The projected curves defining the stent cells are depicted in Fig. 3.8. The PCA increases noticeably when using a larger balloon (3.65–4.36 mm^2 for the Cypher stent and 5.74–6.64 mm^2 for the MULTI-LINK Vison stent). However, using a larger balloon will also induce a higher stress state within the unstented SB vessel wall. This is pure balloon angioplasty, which is known to cause high restenosis rates [25] and therefore a clinical study addressing the choice of balloon size when dilating through the side of a stent could be very valuable. It is likely that a trade-off between optimal cell opening and minimal injury to the SB will be needed. Restricting the length of the balloon outside the stent may already improve the outcome of

this procedure [45].

Table 3.2: Projected Cell Area (PCA) for the two investigated stents prior to and after SB balloon dilatation. Both the 2.5 and 3 mm balloon considerably increase the cell covering the SB, and this cell enlargement is maximal for the 3 mm balloon.

	Cypher	MULTI-LINK Vision
After stenting the MB	1.97 mm^2	2.21 mm^2
After 2.5 mm balloon dilatation	3.65 mm^2	5.74 mm^2
After 3 mm balloon dilatation	4.36 mm^2	6.64 mm^2

Ideally, all stent material should make contact with the vessel wall and all 'floating' struts should disappear. However, floating struts still occur for both stent designs (Fig. 3.7) and this might induce thrombosis formation [87]. The PCA for the MULTI-LINK Vision exceeds the cross-sectional area of the SB, which is 4.91 mm^2 and this is true for both the 2.5 and 3 mm SB balloon. Consequently the enlargement caused by these balloons is acceptable for this stent design. However, this does not guarantee optimal stent deformation and SB access, because this enlarged cell may be badly positioned with respect to the SB. In contrast, the PCA for the Cypher stent is lower than this cross-sectional SB area for the two different balloon sizes. This indicates that these balloons do not sufficiently enlarge the stent opening in front of the SB. The substantial difference in PCA for the two stent designs investigated is related to the different design concepts. The Cypher stent is a typical example of a closed cell design, whereas the MULTI-LINK Vison can be classified as open cell [137].

3.3.3 Stent distortion in the MB

A view into the MB (Fig. 3.9) clearly shows that dilating through the side of a stent may compromise the MB lumen. This phenomenon was also experimentally observed by Ormiston et al. [87] who carried out in vitro tests on five different stent designs. The distortion of the MULTI-LINK Vision stent corresponds well with the in vitro observed deformation of the MultiLink stent, which has a design very similar to the MULTI-LINK Vision stent (see Fig. 3.10). Both designs consist of different ring elements with three connection elements between each two subsequent rings. In particular, a significant distortion immediately distal to the SB after dilatation with a 3 mm balloon was also observed experimentally. The cut view shown in Fig. 3.11 illustrates this type of deformation behaviour.

The horizontal cut view also shows the markedly different deformation behaviour of the Cypher stent compared to the MULTI-LINK Vision stent.

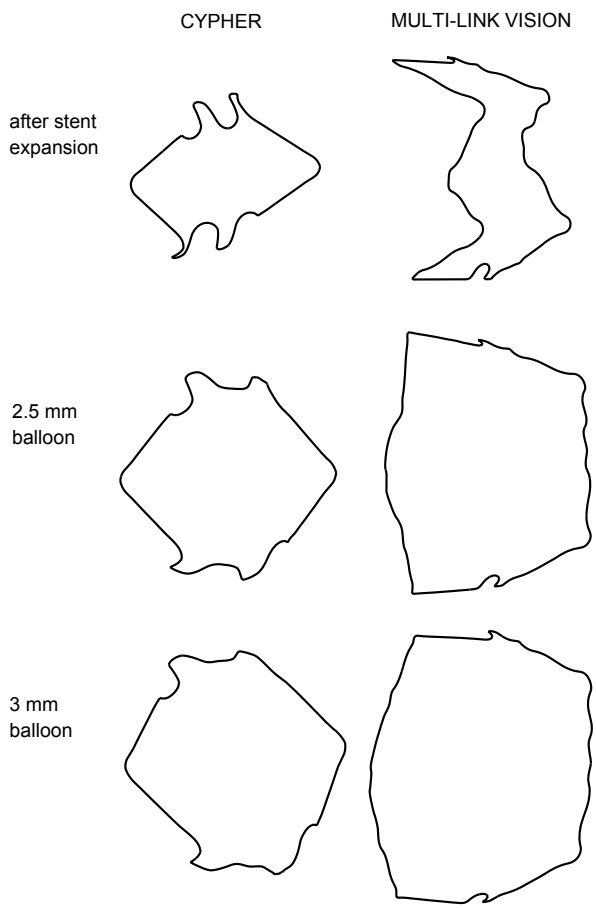

Figure 3.8: Projected stent cells prior to and after SB balloon dilatation. These 2D curves were used to determine the PCA.

For the Cypher stent, all struts remain very close to the MB wall after SB dilatation through a stent opening, although Ormiston et al. [87] reported that dilating through the side of stent compromises the downstream main-vessel lumen regardless of the stent design. However, it should be noted that none of the stent designs investigated in their work has a design similar to the Cypher stent. Furthermore, the impact of the balloon size seems to have a minor effect on the MB scaffolding properties for both stents.

The distortion of the MULTI-LINK Vision stent evidences the need for final kissing balloon (i.e., simultaneous dilatation of MB and SB). This well-known procedure improves the long-term outcome of several bifurcation stenting techniques [8, 51]. Final kissing balloon inflation may also be

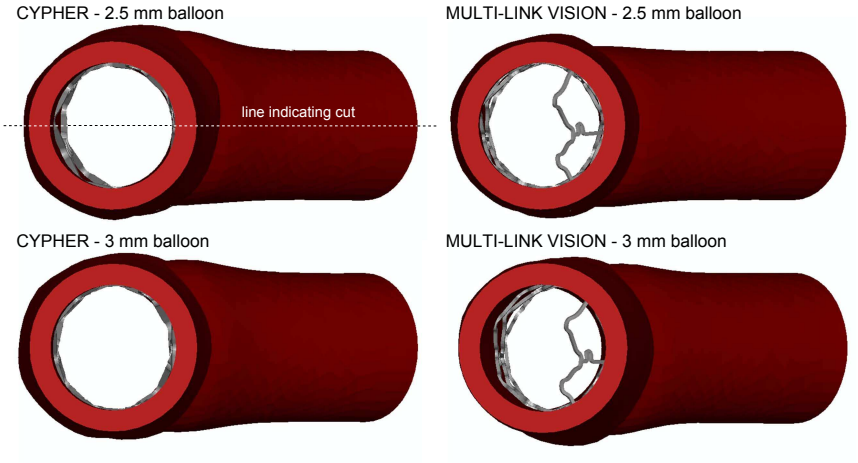

Figure 3.9: View into the MB (from proximal side) showing the impact of the SB balloon dilatation on the MB lumen. The results strongly depend on the stent design, in contrast to the balloon size, which seems to have a minor effect. The horizontal line indicates the cut views depicted in Fig. 3.11.

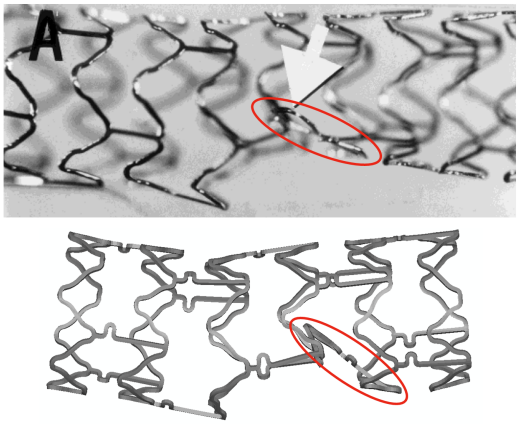

Figure 3.10: Comparison of the distortion of the MultiLink stent observed in bench tests [87] (top panel) with the numerically predicted deformation of the MULTI-LINK Vision stent (bottom panel).

required after dilating through the side of the Cypher stent, although the numerical results show good apposition of the struts. This is due to the fact that the SB balloon inflation has only been performed for one position of the expanded Cypher stent. Furthermore, only one bifurcation geometry has been considered.

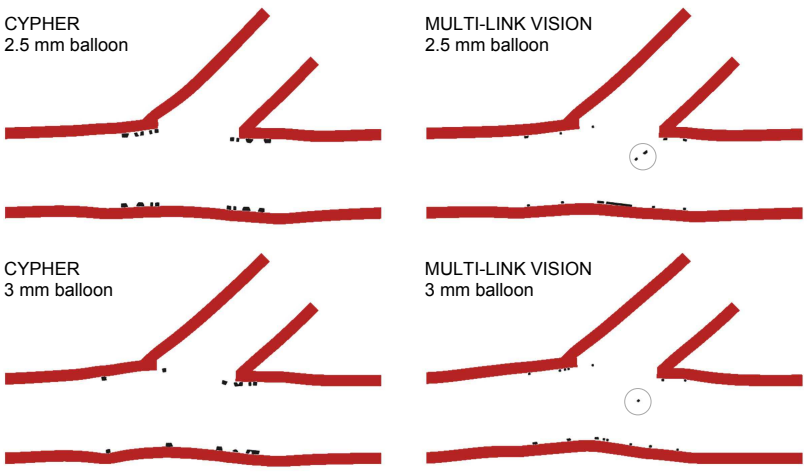

Figure 3.11: Cut view showing the stent strut positions. The circles indicate floating struts in the MB lumen.

3.3.4 Study limitations

The main limitations of this work are related to both the bifurcation morphology and the constitutive behaviour of the vascular tissue. The presence of a plaque is discarded and real-life coronary bifurcations certainly have a more complex geometry. Simulations based on a patient-specific bifurcation lesion including different components (e.g. intima, media, adventitia, lipid pool, etc.) would certainly improve the current model [132]. The anisotropic behaviour of the arterial tissue was discarded and the applied constitutive model should ideally be based on data from human coronary arteries. Furthermore, axial pre-stretch and arterial blood pressure were neglected.

In clinical practice, the balloon catheters for the SB dilatation are being inserted using a guiding catheter. The very small cross-section of this guiding catheter facilitates the placement of the balloon through the stent. A consequence of discarding this insertion procedure from the simulations is the possible presence of intersecting balloon and stent elements after the stent expansion. For the MULTI-LINK Vision stent, a local external pressure was applied on the outer balloon surface in order to avoid such intersections. Furthermore, the balloon catheter is normally (i.e., in clinical practice) bent during insertion through the side of an implanted stent. This bending was taken into account in the numerical model by using folded balloon geometry with an initial curvature. As a result, initial stresses in the balloon membrane due to this bending were neglected. However, the impact of these

stresses on the global deformation is believed to be of minor importance.

3.4 Conclusion

Numerical simulations are a valuable research tool complementing in vitro studies when investigating complex bifurcation stenting techniques due to the accurate prediction of the occurring deformations. The proposed model allows the impact of balloon size and stent design on balloon dilatations through the side of a stent to be quantified, without the need for various expensive stent samples. Furthermore, similar simulation strategies can be developed to study other (in clinical practice) proposed bifurcation stenting techniques, such as crush stenting, T-stenting, etc. This may lead to improved devices and/or procedures to treat bifurcation lesions.

Chapter 4

Virtual stent insertion in a patient-specific coronary bifurcation

THE previous chapter has demonstrated the usefulness of finite element analysis for bifurcation stent research. These simulations allow to study the mechanics of different techniques and devices with an acceptable degree of accuracy. However, advances in simulation techniques and medical imaging combined with the exponential increase in computational capacity open up new horizons in the domain of computational biomechanics. Models, considered state-of-art one day, are quickly replaced by more detailed simulations as shown in this chapter[1]. It is important to stress that results obtained with more simplified models remain useful as long as the assumption are jusitified by, for example, experimental observations.

4.1 Introduction

Stents have demonstrated good results in terms of safety and efficiency when being implanted in unbranched vessel segments, in particular since the introduction DES [138]. However, stenting coronary bifurcation lesions

[1] The contents of this chapter were published in the journal, Annals of Biomedical Engineering:
A novel simulation strategy for stent insertion and deployment in curved coronary bifurcations: Comparison of three drug-eluting stents
P. Mortier, G. A. Holzapfel, M. De Beule, D. Van Loo, Y. Taeymans, P. Segers, P. Verdonck, and B. Verhegghe
38:88-99, 2010

remains challenging due to the increased complication rate and the frequent need for re-intervention [4]. Several bifurcation stenting techniques have been proposed with various levels of complexity, and each of them has one or more limitations [5]. The provisional side-branch stenting strategy, which first involves stent placement in the main branch and second in the side branch, if necessary, is currently the gold standard for the majority of the treatments [18]. Using this provisional approach in combination with a DES yields an acceptable restenosis rate for the main branch, but the results for the SB remain disappointing with a restenosis rate of approximately 15% [4].

In the last couple of years, the second generation of DESs has been introduced on the market. The platform of the first generation DESs (Cypher by Cordis, Johnson & Johnson; Taxus by Boston Scientific) has been modified, and these DESs are now available as Cypher Select and Taxus Liberté, respectively. In addition, new DESs have been developed such as the Endeavor stent (Medtronic), the Xience V stent (Abbott Vascular) and the Promus stent (Boston Scientific). The growing number of available DESs increases the freedom for the physicians to choose from, but it also brings along the question of which stent to use for which particular case/type of stenosis. For example, a very flexible stent with a low crossing profile may be required to treat patients with highly tortuous vessels. Therefore, objective comparisons of these DESs are needed in terms of pharmacological effect, thrombogenicity, geometrical aspects of the design and mechanical performance among many others, because all of these parameters are important for optimal stent selection.

Using finite element analysis, we compared the mechanical effects of three different second generation DESs on the arterial wall of a coronary bifurcation with a (highly) curved main vessel when performing provisional stenting. A new method is used to generate a three-dimensional bifurcation model starting from patient-specific angiographic data obtained *in vivo*. The layered structure of the arterial wall and the anisotropic behavior of each of these layers are considered by applying a novel algorithm to define the fiber orientations. The suitability of the implemented anisotropic constitutive model is shown by comparing the numerically obtained virtual stress-strain response to experimental and analytical results. Innovative simulation strategies are proposed to deploy the stents in the curved main branch including the insertion of the folded balloon catheter over a guide wire. The stent design leading to the highest arterial stresses has been modified using a parametric model with the aim of reducing the arterial trauma while maintaining a sufficient radial strength.

4.2 Materials and methods

4.2.1 Arterial model

4.2.1.1 Geometry

Three-dimensional geometrical information on the lumen of a left coronary tree was obtained by rotational angiography using the dedicated Allura 3D-CA software [139]. The *in vivo*-based data consist of a stack of circular representations of vessel cross-sections, defined by their center, radius and inclination. A small portion of this set of data was selected for further reconstruction, namely that region where the left (main) coronary artery bifurcates into the left anterior descending and the left circumflex artery. Subsequently, NURBS surfaces were created using Rhinoceros 4.0 [140] based on a point cloud that describes the luminal cross sections.

Two luminal cross sections, which were non-diseased, were selected (one proximal and one distal) for both the side and the main branch, and they served as a starting point for generation of the outer wall. At those locations, a circular approximation of the outer wall was obtained by scaling the selected luminal circles. A scaling factor of 1.6 was applied, which resulted in a realistic wall thickness as this factor is based on the anatomical data for non-atherosclerotic coronary arteries published in [12]. A further description of the outer wall was obtained by scaling the remaining luminal circles to a diameter, based on linear interpolation (and extrapolation) of the diameters of the previously calculated cross sections. The resulting circular representations of the outer wall were then used as input for the generation of a second NURBS surface corresponding to the outer boundary.

The commercial software Gambit [141] was used to create a structured hexahedral mesh of the vessel wall starting from the two NURBS surfaces. Finally, the mesh was imported into the open source software pyFormex [130], where it was split into three layers with equal thickness, corresponding to the intima, media and adventitia. Figure 4.1 shows the bifurcation model and clarifies the applied procedure.

4.2.1.2 Arterial tissue

The arterial wall consists of three distinct layers (intima, media, adventitia), and each of these layers is reinforced by collagen fibers leading to a heterogeneous and anisotropic material behavior. These fiber-reinforced composites are assumed to behave nearly incompressible and demonstrate highly nonlinear stress-strain responses. It is assumed that the collagen fibers are organized in two families which can be represented by unit vectors $\mathbf{M}$ and $\mathbf{M}'$ with respect to the undeformed reference configuration. These unit vectors represent the average directions of the two fiber families

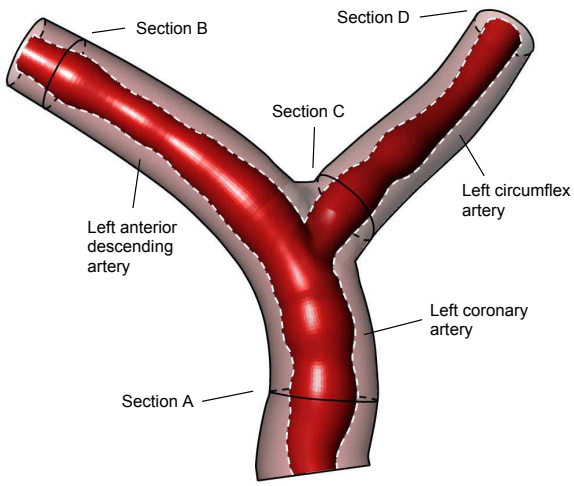

Figure 4.1: Three-dimensional model of the lumen of the left coronary artery bifurcation obtained by rotational angiography. The luminal geometry consists of circular cross-sections. Sections A-D of the lumen were considered non-diseased, and at those locations, the circles were scaled by a factor of 1.6 according to the data published by Holzapfel et al. [12]. Two scaled circles (at sections A and B for the main branch, and at sections C and D for the SB) served as a starting point to generate the outer wall of that branch. All other luminal circles were scaled to a diameter based on a linear interpolation (or extrapolation) of the diameters at sections A and B in case of the main branch or sections C and D for the SB.

embedded in an isotropic ground matrix. The volume preserving part of the strain-energy function $\overline{\Psi}$ to model the mechanical behavior of arterial tissues, as proposed by Holzapfel et al. [12], may be written as

$$\overline{\Psi} = \overline{\Psi}_{\text{iso}} + \overline{\Psi}_{\text{aniso}}, \tag{4.1}$$

which is the sum of an isotropic term $\overline{\Psi}_{\text{iso}}$, related to the matrix material, and an anisotropic term $\overline{\Psi}_{\text{aniso}}$, related to the embedded families of collagen fibers [142]. The two terms are particularized as

$$\overline{\Psi}_{\text{iso}} = \mu(\bar{I}_1 - 3), \tag{4.2}$$

Table 4.1: Material parameters for the constitutive model (4.1)–(4.3) determined by Holzapfel et al. [12]. The data correspond to Specimen I documented in [12].

Layer	μ [kPa]	k_1 [kPa]	k_2 [–]	ρ [–]	α [°]
Intima	28.62	124.01	180.43	0.55	69.5
Media	0.94	13.28	10.81	0.25	21.0
Adventitia	4.04	32.50	103.63	0.65	72.7

$$\overline{\Psi}_{aniso} = \frac{k_1}{2k_2} \sum_{i=4,6} (\exp\left[k_2 \left\{(1-\rho)(\bar{I}_1 - 3)^2 + \rho(\bar{I}_i - 1)^2\right\}\right] - 1), \quad (4.3)$$

where $\bar{I}_1 = \mathrm{tr}\overline{\mathbf{C}}$ is the first invariant of the modified right Cauchy-Green tensor $\overline{\mathbf{C}} = J^{-2/3}\mathbf{C}$, with the volume ratio $J = (\det\mathbf{C})^{1/2} > 0$ and the right Cauchy-Green tensor $\mathbf{C}$, and $\bar{I}_4 = \overline{\mathbf{C}} : \mathbf{M} \otimes \mathbf{M}$ and $\bar{I}_6 = \overline{\mathbf{C}} : \mathbf{M}' \otimes \mathbf{M}'$ are two modified invariants responsible for the anisotropic behavior [143]. By assuming a symmetric arrangement of the two families of collagen fibers and neglecting their radial component allows to define the unit vectors $\mathbf{M}$, $\mathbf{M}'$ in terms of an angle α measured between the fiber reinforcement and the circumferential direction. The (non-negative) material parameters k_2, $\rho \in [0, 1]$ are dimensionless, whereas k_1, μ have the dimension of stress. Holzapfel et al. [12] determined the set of parameters $(\mu, k_1, k_2, \rho, \alpha)$ for the three arterial layers of 13 postmortem non-stenotic coronary arteries corresponding to the model described in (4.1)–(4.3). The angle α was treated as a phenomenological parameter because the collagen structure of the individual layers was not investigated. Uniaxial testing of both longitudinally and circumferentially oriented arterial segments allowed the determination of all parameters by a least-square fitting algorithm. All simulations are based on the material parameters of one (randomly chosen) specimen (i.e. Specimen I in [12]). The used values are summarized in Table 4.1.

A standard approach to model nearly incompressible materials is to add a term of the form $\kappa(J-1)^2/2$ to the strain-energy function $\overline{\Psi}$, where κ is treated as a (positive) penalty parameter (see Chapter 7 in [143]). The penalty parameter κ influences the incompressibility constraint and is determined through numerical experiments.

The constitutive model stated above was implemented as a user-defined material (VUMAT) in ABAQUS/Explicit. The accuracy of material definition was verified by simulating displacement driven uniaxial tension tests for the individual layers both in the longitudinal and the circumferential directions. The resulting stress-strain responses were compared to the ex-

perimental data. In addition, a biaxial test was simulated and the results were compared with the analytical solution as documented in, for example, [144]. This provides an alternative way to verify the implementation of the material model. The simulations of the uniaxial and biaxial tests are performed with a single hexahedral element.

4.2.1.3 Fiber orientation

The anisotropic constitutive model requires an adequate assignment of the radial, circumferential and longitudinal directions in each finite element at the reference configuration. Only then the average fiber directions $\mathbf{M}$ and $\mathbf{M}'$ are properly defined. However, assigning local material orientations is not a straightforward task when dealing with complex geometries as in the present (three-dimensional) study.

The local orientations were defined on an element by element basis in an automated manner, making use of the structured nature of hexahedral discretization. The applied methodology was implemented in pyFormex and is illustrated in Fig. 4.2.

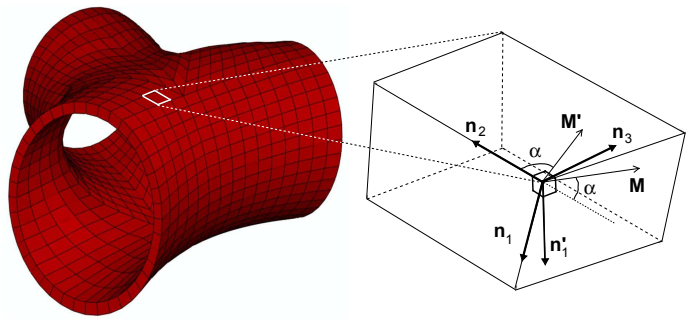

Figure 4.2: Outermost layer of the structured hexahedral discretization at the location of the bifurcation with an enlarged view of the indicated element. Local material orientations ($\mathbf{n}_1'$, $\mathbf{n}_2$, $\mathbf{n}_3$) are computed for every finite element based on its edges.

For each element, two edges were selected: a first edge which has a radial orientation (denoted by vector $\mathbf{n}_1$) and a second edge of which the direction was considered circumferentially (denoted by vector $\mathbf{n}_2$). In most cases, $\mathbf{n}_1$ and $\mathbf{n}_2$ are not perpendicular. Taking the vector product $\mathbf{n}_1 \times \mathbf{n}_2$ yields the longitudinal direction $\mathbf{n}_3$. A second vector product $\mathbf{n}_2 \times \mathbf{n}_3$ gives a modified radial direction $\mathbf{n}_1'$. The three perpendicular vectors $\mathbf{n}_1'$, $\mathbf{n}_2$, $\mathbf{n}_3$ define the local material orientations.

The local axes and the angle α, as given in Table 4.1, define the mean fiber directions $\mathbf{M}$, $\mathbf{M}'$ for each finite element. These mean fiber orientations were

computed at the center of each finite element and are depicted in Fig. 4.3 for a small portion of the superficial elements, located close to the bifurcation. As can be seen the proposed methodology results in a proper description of the fiber orientations for the bifurcated arterial geometry. An alternative method is proposed in [145].

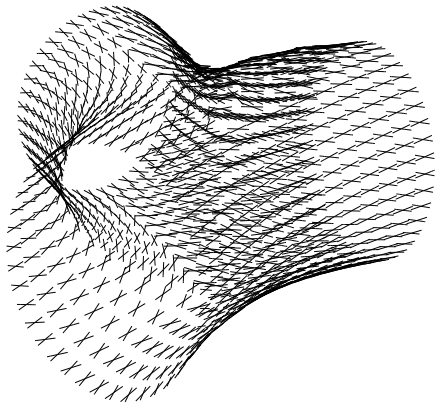

Figure 4.3: Illustration of the (local) mean fiber directions $\mathbf{M}$ and $\mathbf{M}'$ for the finite elements. The directions are depicted for a small portion of the superficial elements, located close to the bifurcation, as shown in Fig. 4.2.

4.2.2 Stent models

Three second generation coronary DES were selected for this study: (i) Cypher Select Sirolimus-eluting stent (Cordis, Johnson & Johnson); (ii) Endeavor Zotarolimus-eluting stent (Medtronic); (iii) Taxus Liberté Paclitaxel-eluting stent (Boston Scientific). Their geometries were acquired by micro-CT imaging of a sample of the devices in their balloon mounted state. The voxel pitch of the scans was 1 µm allowing an accurate assessment of all stent dimensions. This geometrical information was then used to generate three-dimensional parametric computer models using pyFormex. A comparison between a CT-based Endeavor stent geometry and the corresponding discretized model is shown in Fig. 4.4. The Cypher Select and the Taxus Liberté stents have rectangular strut cross-sections, while the Endeavor stent has circular cross-sections. The main characteristics of the three second generation DESs used in the numerical analyses are summarized in Table 4.2.

Both the Cypher Select and the Taxus Liberté stents are laser-cut from 316L stainless steel tubes. The Endeavor stent is made from a cobalt-chromium alloy (F562) and has a modular design where the individual segments are welded to each other. One of these welds is indicated in Fig. 4.4. The

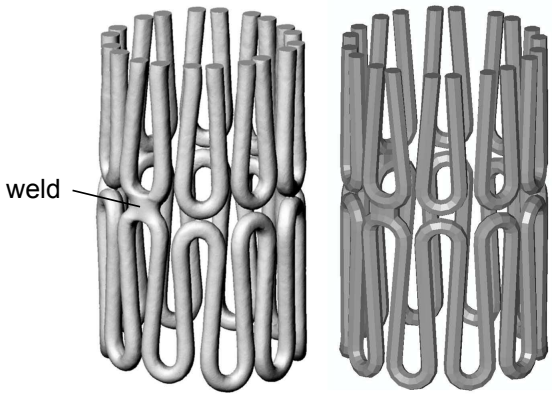

Figure 4.4: Comparison between a part of the micro-CT-based Endeavor stent geometry (left) and the discretized model (right). A weld is also indicated in the left figure.

Table 4.2: Overview of the analyzed stents and their main characteristics.

Stent	Nominal diameter	Nominal length	Strut thickness	Strut width	Material
Cypher Select	3.5 mm	13 mm	140 µm	130 µm	SS316L
Endeavor	3.5 mm	12 mm	91 µm	91 µm	CoCr F562
Taxus Liberté	3.5 mm	12 mm	97 µm	76 µm	SS316L

behavior of both alloys was described by an elasto-plastic material model. Related material properties were taken from [135], and are summarized in Table 4.3.

4.2.3 Balloon model

All stents were inserted and deployed using a semi-compliant Raptor balloon (Cordis, Johnson & Johnson) with a nominal diameter and length of 3.5 mm and 15 mm, respectively. Micro-CT images revealed that this balloon is pleated around the catheter shaft with three folds [126]. A geometrical model of this trifolded Raptor balloon was created using the two step strategy proposed in [123]. First, a discretized model of the unfolded balloon was generated based on the initial balloon diameter (i.e. at 0 MPa) which was obtained after extrapolation of the pressure-diameter data provided by the manufacturer (only available for pressures higher than 0.2 MPa). Second, the folded configuration was created by applying a mathematical

Table 4.3: Stent material properties for the Cypher Select and the Taxus Liberté, made from stainless steel (SS316L), and for the Endeavor, made from a stronger cobalt-chromium alloy (F562), see [135].

Material	Young's modulus	Poisson's ratio	Yield stress	Ultimate tensile stress	Ultimate elongation
SS316L	193 GPa	0.30	366 MPa	675 MPa	43%
CoCr F562	233 GPa	0.35	414 MPa	930 MPa	45%

transformation to all the nodal coordinates (for a detailed description of this transformation see the original work [123]). A uniform thickness of 0.02 mm was assigned to the balloon membrane which was then connected to the catheter shaft by merging the corresponding nodes of the shaft and the membrane. A longitudinal cross-sectional view of the unfolded balloon catheter at 0 bar with the main catheter dimensions are depicted in Fig. 4.5. Thereby the balloon diameter is 3.27 mm, while the nominal diameter of 3.5 mm is reached at the nominal pressure (for the Raptor balloon this is 6 bar).

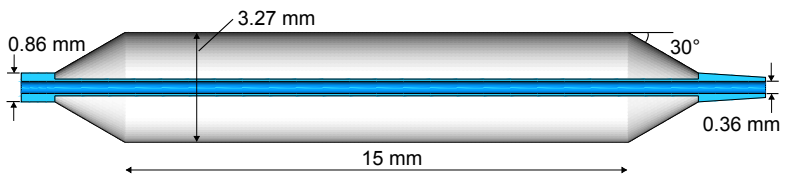

Figure 4.5: Longitudinal cross-sectional view of the unfolded balloon catheter (at 0 bar) with the related dimensions (Raptor balloon from Cordis, Johnson & Johnson; at nominal pressure the nominal diameter is 3.5 mm).

The semi-compliant Raptor balloon catheter is manufactured from a nylon-based material. The mechanical properties of the balloon membrane were derived starting from the compliance chart provided by the manufacturer. The approach, which is described in detail by De Beule [94], is based on the membrane theory and results in stress-strain data which were approximated by a Young's modulus of 850 MPa. Poisson's ratio was assumed to be 0.4. The accuracy of the applied methodology was confirmed by the pressure-diameter data obtained by simulating the unconstrained balloon expansion. The maximum difference in diameter was less than three percent when comparing the simulation results to the manufacturer's original pressure-diameter data. Catheter shafts often contain high density

polyethylene components and, therefore, a linear elastic material was used in the present case, with a Young's modulus of 1000 MPa and a Poisson's ratio of 0.4.

4.2.4 Numerical simulations

All 3.5 mm stents were advanced to the location of implantation by simulating the insertion of the stent system over a guide wire. It was not possible to immediately position the stent system at the implantation site without protruding the vessel wall because of the highly curved main branch. Guide wires are often manufactured from nitinol and typically have a diameter of 0.36 mm (i.e. 0.014 inch). The superelastic nitinol properties were neglected because the guide wire deformations were small. A Young's modulus and Poisson's ratio of 62 GPa and 0.3 were assigned, respectively, to represent the elastic behavior in the austenite phase [146]. The guide wire was fixed at both ends. Insertion was simulated by enforcing a displacement at the proximal end of the catheter shaft. An additional (equal) displacement boundary condition was imposed to the proximal stent end. Without this condition, it was impossible to adequately position the stent because sliding occurred between the balloon membrane and the inner stent surface. This sliding was due to insufficient frictional forces, although a pressure was applied to the outer stent surface during insertion to mimic the stent fixation after crimping. After positioning, the Raptor balloon was subsequently inflated and deflated to deploy the stent. The maximum balloon pressure was 12 bar. The bifurcation model was constrained at its three ends in all directions. Figure 4.6 shows the complete insertion and deployment procedure for the Taxus Liberté stent.

Implanting stents in curved vessels cause stress concentrations at the stent ends, see, for example, [147, 148]. Therefore, in order to analyze this effect with the aim to reduce stress concentration at the stent ends, two design modifications of the Cypher Select stent were generated using the parametric modeling capabilities of pyFormex. The first modification, labeled as $\mathtt{CS}_{\text{thin}}$, has a strut thickness of 100 µm everywhere (as compared to 140 µm of the original Cypher Select design). All other design parameters remain unaltered. The second modification, labeled as $\mathtt{CS}_{\text{end}}$, only differs from the original Cypher Select design at its proximal and distal ring segment. These two end rings have a reduced strut width w_1 of 90 µm (as compared to a strut width w_2 of 130 µm of the original Cypher Select design) in order to reduce the change in stiffness between the stented and non-stented vessel segments, see Fig. 4.7.

Such a modification has a relatively minor impact on the radial strength in the central region of the stent. A sufficient radial strength is required in order to resist the compressive forces of the arterial wall after deployment and

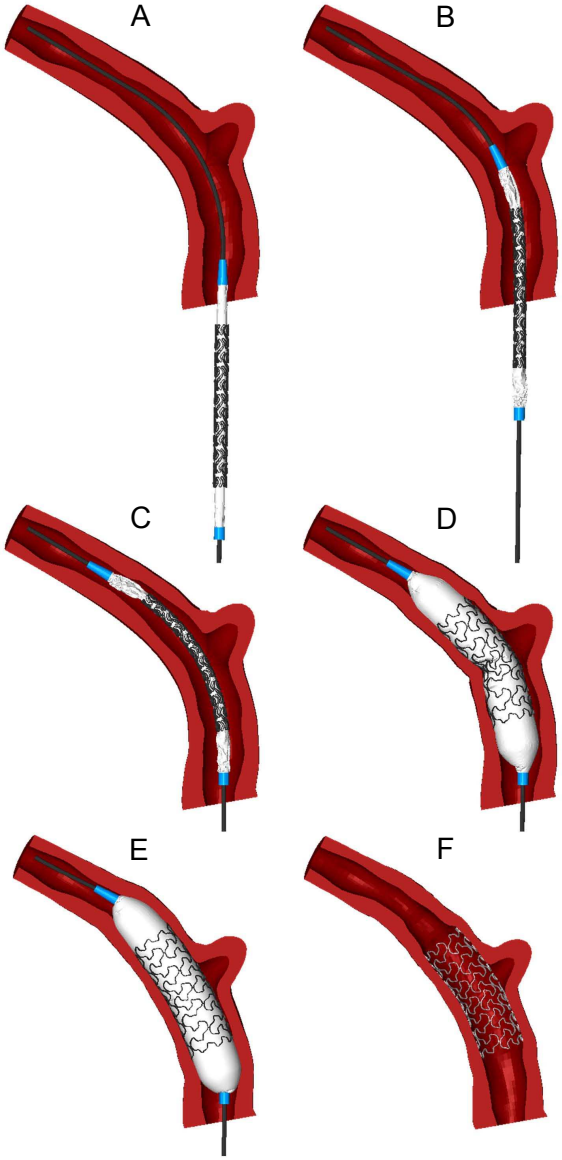

Figure 4.6: Illustration of the simulated stent insertion and deployment procedure: panel A – initial configuration; panel B – intermediate position during insertion; panel C – final position prior to expansion; panel D – partially inflated stent at a balloon pressure of 3 bar; panel E – configuration at the maximum pressure of 12 bar; panel F – final state after balloon deflation.

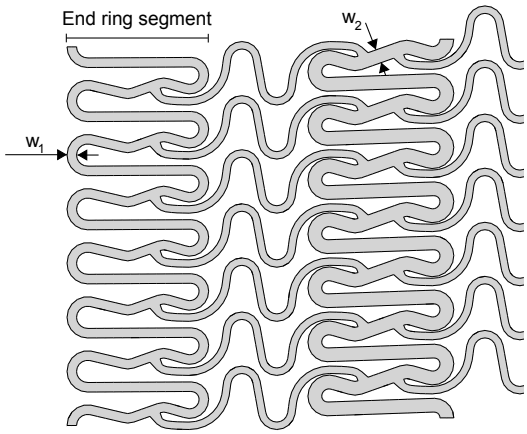

Figure 4.7: Unrolled model showing one end of the modified Cypher Select stent $\mathtt{CS}_{\mathrm{end}}$: The strut width w_1 of the proximal and distal ring segments is 90 µm, whereas all central ring segments have a strut width w_2 of 130 µm. For the original Cypher Select stent model, w_1 and w_2 are equal to 130 µm.

to guarantee a sufficient luminal area. Therefore, all original and modified stent designs with 3.5 mm nominal diameter were subjected to a 'virtual radial strength test'. The stents were expanded in a cylindrical polyurethane tube, which is 4 mm longer than the crimped stent, having an internal diameter of 3.5 mm and a wall thickness of 50 µm [149]. A displacement driven deployment method was used to expand all stents to an inner diameter of 3.5 mm [126]. The tube was fixed at both ends and the polyurethane was described by an elastic constitutive model with a Young's modulus of 40 MPa and a Poisson's ratio of 0.3 [150]. Subsequently, a gradually increasing pressure was applied on the outer tube surface. At low pressures, this typically resulted in a small, approximately linear decrease of the stent diameter. However, when the pressure exceeded a certain threshold value, the stent diameter suddenly decreased considerably. The radial strength was then defined as the pressure causing this sudden diameter decrease (or collapse of the stent structure).

All three-dimensional models with the exception of the balloon membrane are discretized using linear hexahedral elements using reduced integration and hourglass control (Cypher Select stent and the modified stent designs: 15848; Endeavor stent: 46800; Taxus Liberté: 21000; arterial model for the bifurcation: 12000; guide wire: 1500; catheter shaft: 960; tube to be used for the radial compression test: 2016). The circular cross-sections of the Endeavor stent struts require a higher number of elements as compared to the other stent models, which have struts that can be approximated with rectangular cross-sections. The meshes of the bifurcation arterial model are

generated with matching nodes on the tissue interfaces, leading to a proper connection between the individual arterial layers. The discretization of the balloon consists of both triangular (4662) and quadrilateral (10875) fully integrated linear membrane elements.

The ABAQUS/Explicit solver was used for the large deformation analyses, as this code provides a very stable general contact algorithm. Friction was included in the simulations by means of a Coulomb friction model. The coefficient used for all contact pairs was assumed to be 0.2. A well-established technique to reduce the computational effort of explicit analyses is to 'accelerate' the virtual process in comparison with the physical procedure. However, this approach can lead to unrealistic dynamic effects that may change the response of the system. Since the insertion and deployment were considered to be quasi-static phenomena, where inertial forces have a negligible impact, such an artificial acceleration was applied in a controlled manner by monitoring the kinetic energy of all components involved.

4.3 Results and discussion

4.3.1 Verification of the implemented arterial model

The numerically obtained stress-strain responses after uniaxial extensions of the arterial strips in the axial and circumferential directions are depicted in Fig. 4.8. A comparison with experimental data, as published by Holzapfel et al. [12], is also provided and shows a very good agreement with the model results.

The results of the simulated biaxial deformation of the media and the corresponding analytical results (see, for example, [144]) in terms of Cauchy stress versus stretch also show a very good correlation (see Fig. 4.9), which confirms the accuracy of the implemented constitutive model.

4.3.2 Comparison of the second generation DES

Implantation of the stents in the curved main branch changes the three-dimensional vessel geometry significantly. In particular, a straightening effect of the stented vessel was observed in all cases considered, and an illustration for the Cypher Select stent is provided in Fig. 4.10. This effect can be explained by the relatively high bending and radial stiffness of the stent as compared to the vessel. Hence, a compliance mismatch occurs at the stent ends leading to discontinuities as indicated in Fig. 4.10.

This abrupt compliance change, in combination with a slightly smaller initial luminal diameter at the distal stent end, causes the highest circumferential stresses in the vessel wall at that location (see Fig. 4.11). These results

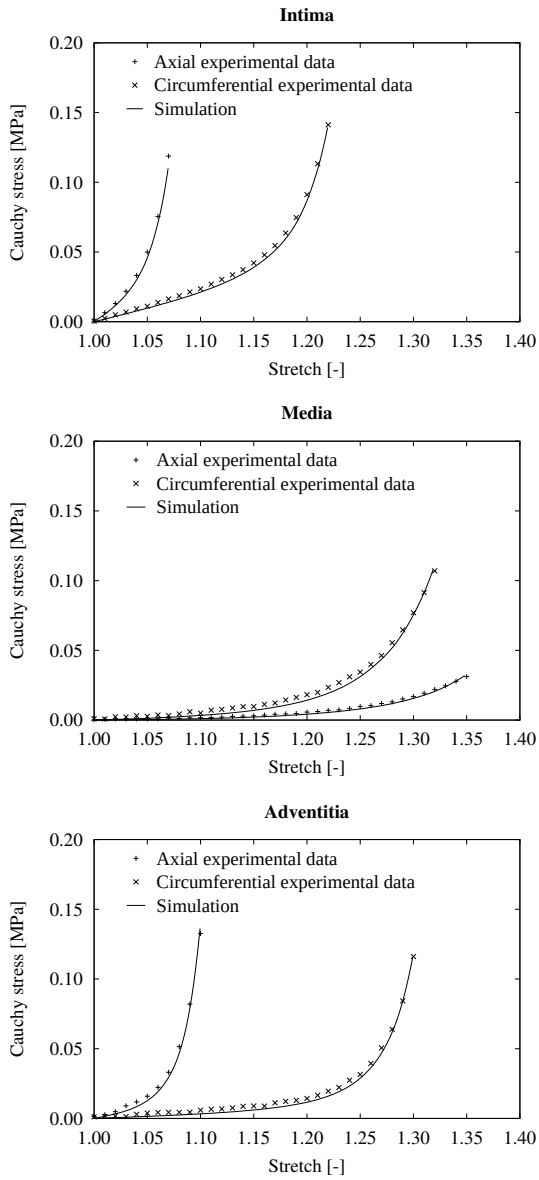

Figure 4.8: Comparison of simulated uniaxial extensions of arterial strips in the axial and circumferential directions shows very good agreement with experimental data documented in [12].

correspond in particular with the observations of Wu et al. [148], who compared the stresses in the arterial wall after stent implantation in a straight

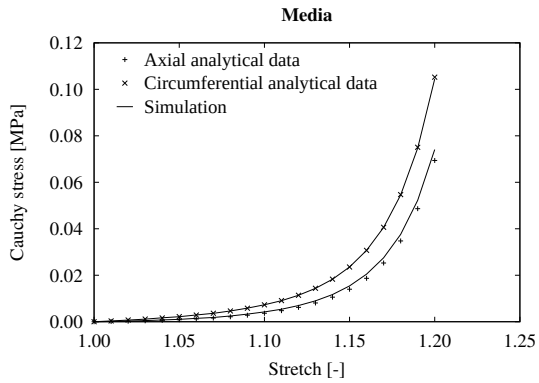

Figure 4.9: Comparison of simulated biaxial deformation of the media in terms of Cauchy stress/stretch and corresponding analytical results shows good agreement.

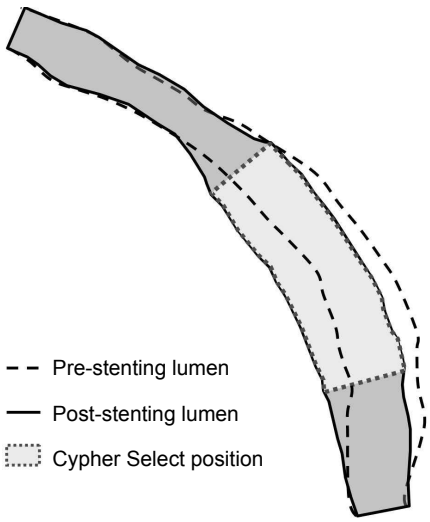

Figure 4.10: Comparison of the pre- and post-stenting luminal curvatures. Stent implantation results in vessel straightening here shown for the Cypher Select stent.

and a curved vessel. In the curved vessel model, these authors also identified the highest arterial stresses at the stent ends. The circumferential (Cauchy) stress peaks for the Cypher Select, the Endeavor and the Taxus Liberté in our simulations are 0.38, 0.15 and 0.15 MPa, respectively. The substantially higher maximum stresses for the Cypher Select stent after deployment is related to the higher stiffness of this device, which is mainly due to its closed cell design and large strut thickness (compare with Table 4.2). In contrast, the Endeavor and Taxus Liberté stents have more flexible open cell designs

and smaller strut thicknesses.

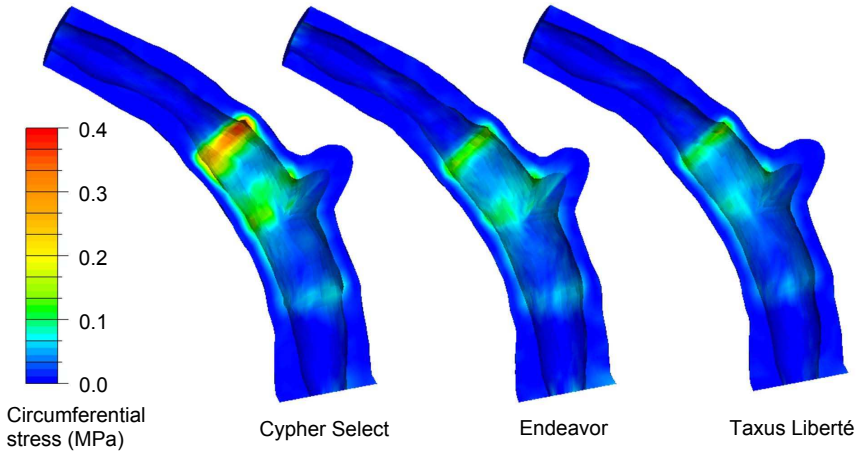

Figure 4.11: Comparison of the circumferential (Cauchy) stress distribution after implantation of the Cypher Select, the Endeavor and the Taxus Liberté stents, with maximal stresses of 0.38, 0.15 and 0.15 MPa from left to right.

Similar changes in the curvature have been reported in the past using *in vivo* imaging before and after stent deployment [151, 152]. Considerable vessel straightening was identified as a predictor for major adverse cardiac events such as death, acute myocardial infarction or revascularization [153]. This increased complication rate might be explained by the high stresses or stress gradients which occur at the stent ends in case of the vessel straightening, but the impact on the blood flow dynamics might also play an important role. For example, Wentzel et al. [152] showed that changes in vessel curvature lead to areas with decreased and increased wall shear stresses at the stent ends, and suggested that this might contribute to the occurrence of restenosis. A large randomized trial comparing sirolimus-eluting stents with bare metal stents showed an in-stent restenosis rate of 3.2% for the drug-eluting stent group [138]. However, by considering the stented vessel segment and the non-stented regions 5 mm proximal and distal to the stent, a restenosis rate of 8.9% was obtained. These results clearly demonstrate the vulnerability of the unstented segments near the stent ends. Vessel straightening and the resulting stress concentrations may have contributed to the restenotic reaction at the edges of the stent, regions that are less protected by drug delivery. Many other factors are of course involved. For example, the higher incidence of endothelial injury observed at the stent ends may also induce local reactions. Squire [33] explained this particular injury pattern to be the result of three mechanical factors: (i) direct balloon-artery contact due to a protrusion of the balloon at the stent ends, (ii) an axial contraction of the stent (foreshortening), (iii) a nonuniform

ends-first expansion behavior of the stents (dogboning). Based on finite element simulations, a reduction of the balloon overhang has been suggested to eliminate the dogboning effect, while at the same time minimizing the area with direct balloon-artery contact [127].

Figure 4.12 compares the circumferential stress distributions caused by the implantation of the two modified stent designs ($\mathtt{CS}_{\mathrm{thin}}$, $\mathtt{CS}_{\mathrm{end}}$), while the left image of Fig. 4.11 is the analogue for the original Cypher Select stent.

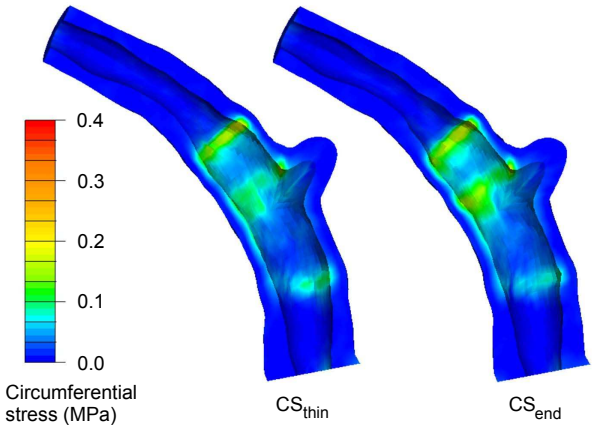

Figure 4.12: Comparison of the circumferential (Cauchy) stress distributions caused by the implantation of the two modified (Cypher Select) stent designs, $\mathtt{CS}_{\mathrm{thin}}$ and $\mathtt{CS}_{\mathrm{end}}$, while the left image of Fig. 4.11 shows the analogue for the original Cypher Select stent: a reduction of the overall strut thickness ($\mathtt{CS}_{\mathrm{thin}}$) or of the strut width of the distal and proximal ring segments ($\mathtt{CS}_{\mathrm{end}}$) leads to a bisection of the maximal stresses around one stent end.

The stress patterns are very similar, however, the maximum circumferential stresses at the distal stent end are much lower for the two modified designs. The original Cypher Select stent design caused a maximum stress of 0.38 MPa, while the maximum stresses induced by the $\mathtt{CS}_{\mathrm{thin}}$ and $\mathtt{CS}_{\mathrm{end}}$ stent are 0.19 and 0.18 MPa, respectively. Hence, a stress reduction of 50% was obtained by reducing the strut thickness of the complete stent (i.e., modification $\mathtt{CS}_{\mathrm{thin}}$) or by reducing the strut width of the distal and proximal ring segments only (i.e., modification $\mathtt{CS}_{\mathrm{end}}$). Hence, these two completely different design modifications decrease the arterial trauma caused by stent implantation for this specific vessel morphology. The $\mathtt{CS}_{\mathrm{thin}}$-design leads to an overall decrease in the bending stiffness, while the $\mathtt{CS}_{\mathrm{end}}$-design reduces the compliance mismatch at the stent ends. It should be noted that reducing the strut width or thickness will have a negative effect on the obtained luminal gain after stent implantation. This parameter was, however, not studied since the stents were implanted in a non-diseased vessel segment.

Table 4.4: Radial strength, defined to be the external pressure causing a sudden collapse of the stent structure, numerically determined for all stent designs, i.e. the original ones and the modified stents $\mathtt{CS}_{\text{thin}}$ and $\mathtt{CS}_{\text{end}}$.

Stent	Radial strength [MPa]
Cypher Select	0.15
Endeavor	0.10
Taxus Liberté	0.10
$\mathtt{CS}_{\text{thin}}$	0.11
$\mathtt{CS}_{\text{end}}$	0.14

Stent designs are always a compromise between (often conflicting) design requirements. They should be flexible enough to allow easy placement and to minimize vessel straightening after deployment, while simultaneously offering a sufficient radial strength to resist the compressive forces of the dilated vessel. Therefore, the three original DESs and the two modified stent designs ($\mathtt{CS}_{\text{thin}}$ and $\mathtt{CS}_{\text{end}}$) were subjected to a 'virtual radial compression test'. The results are reported in Table 4.4 in terms of radial strength defined as the external pressure causing a sudden large decrease of the stent diameter.

The Cypher Select stent has the highest radial strength, although being made of a weaker material than the Endeavor stent. This radial strength results from the stent's closed cell structure in combination with the robust struts (width: 130 µm, thickness: 140 µm). The modified Cypher Select design with a reduced strut thickness of 100 µm ($\mathtt{CS}_{\text{thin}}$) induces lower stresses in the vessel wall, but this modification also significantly reduces the radial strength. Therefore, the $\mathtt{CS}_{\text{end}}$ stent might represent a good design compromise since it also leads to reduced arterial stresses, while maintaining a high radial strength which might be required for certain types of lesions.

High restenosis rates up to 15% have been observed in the side branch after stenting the main vessel, even in the drug-eluting stent area [4]. Suboptimal drug delivery at the side-branch ostium due to incomplete strut coverage and disturbed blood flow have been suggested as possible causes [154]. A well-established procedure to improve the flow conditions and strut coverage involves the dilation of an angioplasty balloon through the side of stent, frequently performed simultaneously with a main branch dilation (i.e. kissing balloon inflation) to avoid undesired stent deformation [87, 155]. However, such an inflation may again cause additional endothelial damage at the unstented entry of the SB. Our results show stress concentrations in the neighborhood of the side-branch ostium for all stent designs. Hence, significant stress gradients occur since the circumferential stresses within the SB are negligible. These gradients may also contribute to or initiate the

observed restenotic processes. Two stent techniques have been proposed with the aim of providing full ostium scaffolding but they are often difficult to perform and do not improve the outcome [4].

During the last decade, many advances have been made in the field of finite element stent modeling. On the tissue level, considerable progress has been achieved regarding the accurateness of the arterial geometries and the constitutive modeling of soft biological tissues, see, for example, [113, 156]. On the device level, more realistic balloon models have been introduced and methods have been proposed to generate realistic models of existing stents [126, 127]. In this study, the insertion of the stent system was incorporated in the simulations in order to position the stents in the curved vessel. This introduces an additional level of complexity and provides more refined results with the drawback of an increased CPU time.

One limitation of the current bifurcation model is the absence of a stenotic plaque, although the feasibility of generating patient-specific stenotic geometries has been demonstrated in previous works [147, 157]. However, these stenotic models are based on high-resolution images of *ex vivo* tissue samples. Since the aim of the current study was to assess the influence of stent implantations on vessel walls with realistic curvatures, *in vivo*-based images were required. To the best of our knowledge, *in vivo*-based arterial models including the various three-dimensional diseased components have not yet been generated. Starting from luminal information originating from rotational angiography, a three-dimensional model was here generated based on assumptions regarding the wall thickness. The currently applied procedure may be further improved by combining the angiographic images with intravascular ultrasound data [98].

4.4 Conclusion

A novel simulation strategy considering the insertion of a stent system over a guide wire in a curved coronary bifurcation has been proposed; the effect of different second generation drug-eluting stents on arterial wall stresses has been analyzed. The curved MB of the three-dimensional bifurcation model was straightened after implantation of every stent investigated. The compliance mismatch at the stent ends induced stress concentrations that may cause biological responses. The maximum wall stresses caused by the analyzed drug-eluting stents differ considerably. Two modified stent designs, created by a parametric modeling technique, have been proposed as an illustration of the virtual design methodology. Both designs significantly reduce the stress peak at one stent end, demonstrating the potential of using finite element modeling during the design phase of new devices.

Chapter 5

Geometrical stent analysis

INTERVENTIONAL cardiologists are being overwhelmed by the large number of available stents offered by various medical device companies. The optimal stent to treat every lesions will probably never exist because the multitude of product requirements (e.g. optimal drug-delivery, biocompatibility, radiopacity, mechanical behaviour, etc.) turns the development into a process of making compromises and results in dedicated stents optimal for certain subsets of lesions. For example, reducing the strut thickness (and thus the crossing profile) often has a negative impact on the radial strength. This rises the question: 'Which stents are preferred for which types of lesions?' For the given, simplified example, the most flexible stent should be used when the vascular tree is highly tortuous, while the stent having a high radial strength might be preferred to treat severely stenosed vessels. In this chapter, an attempt is made to quantify and compare some design aspects important for bifurcation stenting of a number of frequently used stents[1].

5.1 Stent cell size

5.1.1 Introduction

Stenting coronary bifurcation lesions is still associated with higher restenosis rates compared to conventional stent implantation, even in the drug-eluting

[1] Parts of this chapter were published in the journal, EuroIntervention:
Comparison of drug-eluting stent cell size using micro-CT: important data for bifurcation stent selection
P. Mortier, D. Van Loo, M. De Beule, P. Segers, Y. Taeymans, P. Verdonck, and B. Verhegghe
4:391–396, 2008

stent era [41]. Adequate wall coverage and good positioning of the stent struts against the vessel wall are considered as two crucial factors for successful bifurcation stenting [41, 87]. This can be accomplished by applying a suitable stenting technique and using an appropriate stent design. Selecting a stent design with a sufficiently large cell size reduces the possibility of compromising the MB or SB lumen. For example, stent placement in the MB is often followed by inflating a balloon through the side of the stent in order to improve the SB lumen (and sometimes to create access for subsequent stent placement in the SB). In this case, the size of the cell through which the balloon is inflated should preferably be as large as the SB ostium (Fig. 5.1, panel A). The same condition applies to stents used during the so-called 'crush' procedure. This is a technique which should be ended by kissing balloon postdilatation [51] to obtain optimal deployment (Fig. 5.1, panel B). The cell opening also plays a major role for culotte stenting, during which a stent is implanted in the proximal part of the MB and in the SB. Kissing balloon postdilatation is often performed to optimize the downstream lumen. To achieve optimal results, the cell size of this stent should preferably be as large as the cross-section of the main branch (Fig. 5.1, panel C).

The size of stent cells has already been reported in previous studies, based on data provided by the manufacturers [45], or by measuring the width and height of expanded stent cells [89, 158]. To our knowledge, an independent method to measure stent cells with high precision has not been proposed yet. Therefore, we developed a methodology to accurately quantify the cell circumference of stents based on micro-CT scans. Furthermore, the size of the ostium is calculated based on diameter and angle information for several bifurcation geometries. Combining cell size with anatomical information may assist to select the appropriate stent design for the applied treatment technique and for the particular patient.

5.1.2 Materials and methods

5.1.2.1 Investigated stents

The cell circumference was determined for the following five '3 mm' stents: the sirolimus eluting Cypher (8 mm length, Cordis, Johnson & Johnson, Warren, NJ, USA), PRO-Kinetic (18 mm length, Biotronik, Berlin, Germany), the paclitaxel eluting Taxus Liberté (32 mm length, Boston Scientific, Natick, MA, USA), the everolimus eluting Promus (12 mm length, Boston Scientific, Natick, MA, USA) and the ABT-578 eluting Endeavor (12 mm length, Medtronic, Minneapolis, MN, USA) stent. The Cypher and Taxus Liberté stent are stainless steel stents, while the others are made of the stronger cobalt chromium alloy. The PRO-Kinetic stent is coated with a silicon carbide layer. The Promus stent uses the Multi-Link Vision

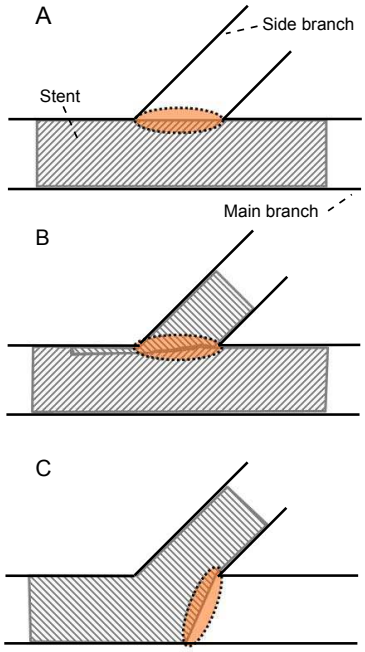

Figure 5.1: Stent cell requirements for different stenting strategies (the zone of interest is indicated with a dotted line). When performing provisional bifurcation stenting, the stent cells should be at least as large as the SB ostium (panel A). The same condition is valid for both the side and MB stent during crush stenting (panel B). The situation as shown in panel C is encountered during culotte stenting and in this case, the cells should be at least as large as the cross-section of the MB..

stent platform and is identical to the Xience V stent (Abbott Vascular, Redwood City, CA, USA).

5.1.2.2 Micro-CT

All stents were scanned as delivered by the manufacturer in their crimped, balloon-mounted state. In order to obtain accurate results on the stent cell dimensions, only 8 mm of the total stent length was scanned using a Varian Paxscan 2520V X-ray amorphous-Si flat panel detector with 1536x1920 pixels of 127 µm. With a magnification factor of 34, this results in a CT voxel size of 4.3 µm. The in-house built high resolution set-up at the UGCT facility [119] used for this investigation consists of a Feinfocus open type X-ray tube (Xylon/Feinfocus, Comet Group, Flamatt, Switzerland) with transmission target and a sample manipulator with air bearing rotation stage. The X-ray tube was used at 100 kV and 2.7 W with the resolution

of this total system under 2 µm. The scans consisted of 600 projection images (0.8 sec integration time) that were reconstructed using Octopus reconstruction software developed at UGCT [159]. The resulting dataset of cross-sectional images was imported into Mimics (Materialise, Leuven, Belgium) where a triangulated surface mesh of the stents was created and exported in the stl format.

5.1.2.3 Cell circumference determination

The triangulated surfaces representing the stents outer surfaces were imported in pyFormex [130], open-source software currently under development at our institution. pyFormex is a tool for generating, manipulating and operating on large geometrical models of 3D structures by sequences of mathematical transformations. The stent geometries were unrolled by transforming the coordinates and were cut by a plane after selection of a smaller zone in order to obtain planar line segments. Subsequently, a cell was selected for each stent from the resulting collection of two-dimensional lines and used to determine the cell circumference. This cell circumference was then used to calculate the corresponding maximum achievable diameter (D_{max}) of the cell opening that can be obtained upon inflation of a balloon through the side of the stent. This D_{max} is equal to the cell circumference divided by π.

5.1.2.4 Calculation of ostium circumference

The ostium circumference was determined for idealised bifurcations with a cylindrical MB and SB starting from a parametric description of the ostium, which is the threedimensional line indicated in Fig. 5.2. The ostium was written as a function of the MB axial position: $x = f(z)$ and $y = f(z)$ with z the MB axis. Subsequently, the ostium circumference was calculated as the sum of the length of infinitesimal small line segments. The resulting circumference depends on the MB and SB diameters and on the angle of intersection.

5.1.3 Results

5.1.3.1 Cell circumference

The different steps of the cell circumference measurement procedure are shown in Fig. 5.3 for the Cypher stent. Panel A shows the triangulated surface obtained after reconstruction and segmentation of the micro-CT images. A mathematical transformation of the coordinates of all triangles results in an unrolled stent geometry (panel B), which is still three-dimensional. Subsequently, a small zone containing one cell is selected

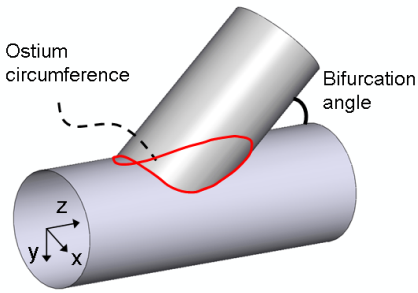

Figure 5.2: The size of the ostium depends on the bifurcation angle and the SB and MB diameters. The ostium is described by a three-dimensional curve from which the circumference can be calculated.

(panel C). The planar line segments depicted in panel D are obtained after intersection of this three-dimensional geometry with a plane. This can then be used to select a single cell and to calculate its circumference, as shown in panel E.

Applying the same methodology to the other stents results in the planar cells shown in Fig. 5.4. The cell circumferences and the corresponding maximum achievable diameters of the different stents are summarized in Table 5.1. The cells of the Cypher stent have the smallest circumference (i.e. 9.5 mm or D_{max} = 3.0 mm), whereas the Endeavor stent has the largest openings (circumference = 19.8 mm or D_{max} = 6.3 mm).

Table 5.1: Overview of the cell circumferences and the corresponding equivalent diameters. These are the maximum diameters of the strut openings that can be obtained upon inflation of a balloon through those openings.

Stent	Cell circumference	Maximum achievable cell diameter D_{max}
Cypher	9.5 mm	3.0 mm
Endeavor	19.8 mm	6.3 mm
PRO-Kinetic	10.8 mm	3.4 mm
Promus	12.6 mm	4.0 mm
Taxus Liberté	12.6 mm	4.0 mm

5.1.3.2 Ostium circumference

The ostium circumference is displayed as a function of the angle of intersection for a 3 mm MB (Fig. 5.5). The results are shown for three possible

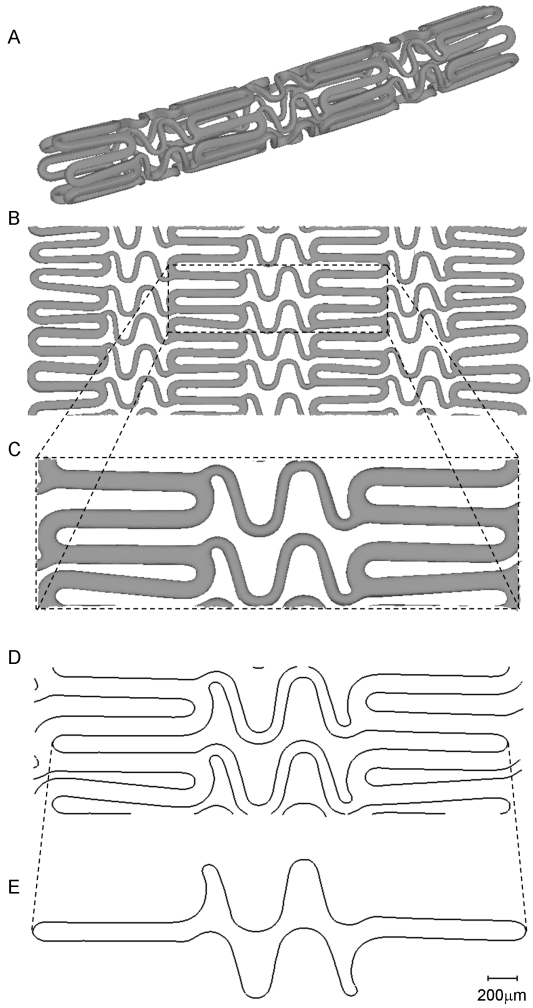

Figure 5.3: Demonstration of the complete procedure to obtain a single cell of the Cypher stent. The cell circumference can then easily be calculated as the sum of the length of all planar line segments of this cell.

SB diameters (i.e. 2.25, 2.50 and 2.75 mm).

5.1.4 Discussion

Cell circumferences of the studied DES designs differ considerably, with values ranging from 9.5 to 19.8 mm or with a maximal achievable cell diameter

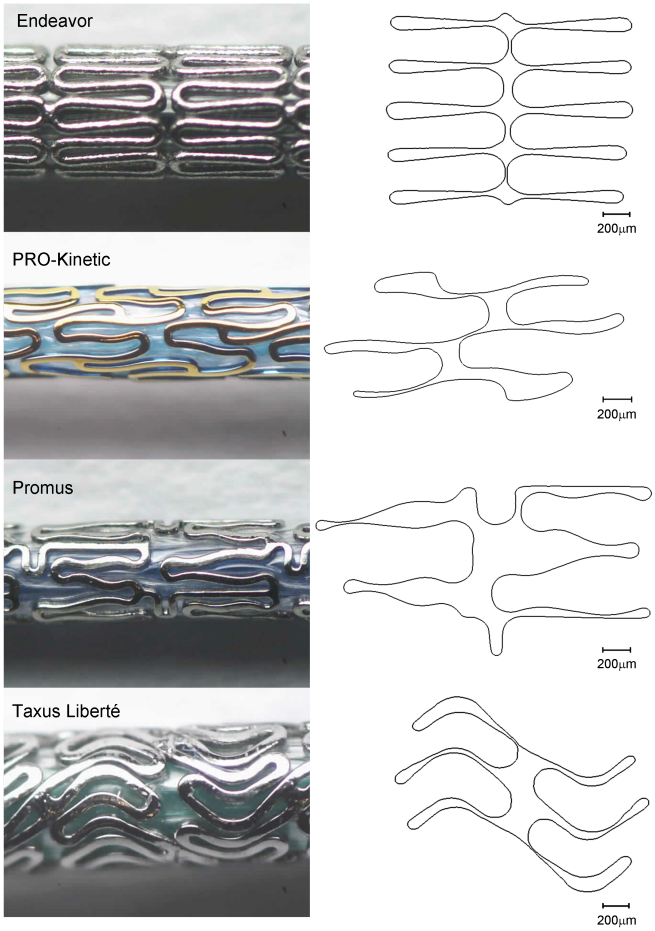

Figure 5.4: Comparison of microscopic images with the resulting planar representations of the cells. The microscopic images do not have the same scale. From top to bottom: Endeavor, PRO-Kinetic, Promus and Taxus Liberté.

(D_{max}) varying between 3.0 and 6.3 mm. These stent openings play an important role, especially during bifurcation stenting [45, 89]. For example, dilating a balloon through the side of a main branch stent with openings that are too small will fail to completely restore the SB lumen due to obstructing stent struts. Struts not in contact with the vessel wall should be avoided as this may cause thrombus formation [87]. The large variation of the cell sizes of the investigated stents are explained by the different design concepts. The Cypher stent is a typical example of a closed cell design, whereas all other stents can be classified as open cell designs.

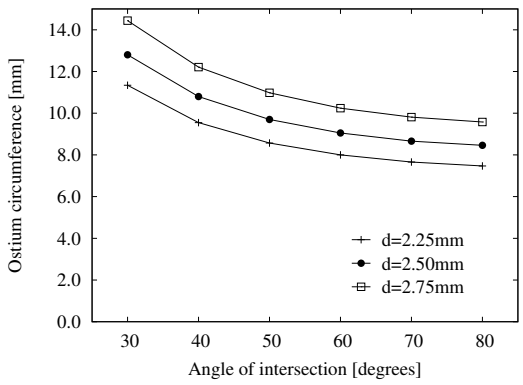

Figure 5.5: The ostium circumference of a 3 mm parent vessel is shown as a function of the SB diameter and the bifurcation angle.

Combining cell size with anatomical data may assist to select a stent for a given bifurcation stenting problem. This requires knowledge of the ostium circumference, which, as we have shown, can be mathematically calculated when idealizing the bifurcation geometries with a cylindrical MB and SB. Real-life bifurcations will certainly have a more complex anatomy [11] (e.g. ostial calcification and/or tortuosity), but these calculated values are still valuable as they are at least indicative and provide an idea of the order of magnitude. In the idealized case, the ostium circumference depends on the MB and SB diameter and on the angle of intersection. The relation between the angle and the ostium circumference is clearly nonlinear (Fig. 5.5) as the circumference varies more rapidly at small angles. This indicates that special attention should be paid to the selection of a stent which will be implanted in the MB of a small angled bifurcation. In Fig. 5.6, the stent cell circumferences are plotted on these graphs. The dark zones show the cases in which the ostium circumference is larger than the cell circumference when the stents are deployed in a 3 mm MB (for three different SB sizes). For example, when a Cypher stent is implanted in a bifurcation with a 3 mm MB, 2.5 mm SB and a 40 degree angle, the ostium circumference (10.8 mm) is larger then the cell circumference (9.5 mm). Therefore, it is highly likely that in these cases the cells will not be sufficiently enlarged by balloon dilatation through the side (and final kissing balloon postdilatation) and that not all stent struts will be in contact with the vessel wall.

The presented cell data are also useful for stents partially deployed in the MB and SB as encountered during culotte stenting. These stents should preferably have cells with a D_{max} greater than the distal MB diameter. If this condition is not respected, it is highly likely that gaps will occur between some struts and the vessel wall.

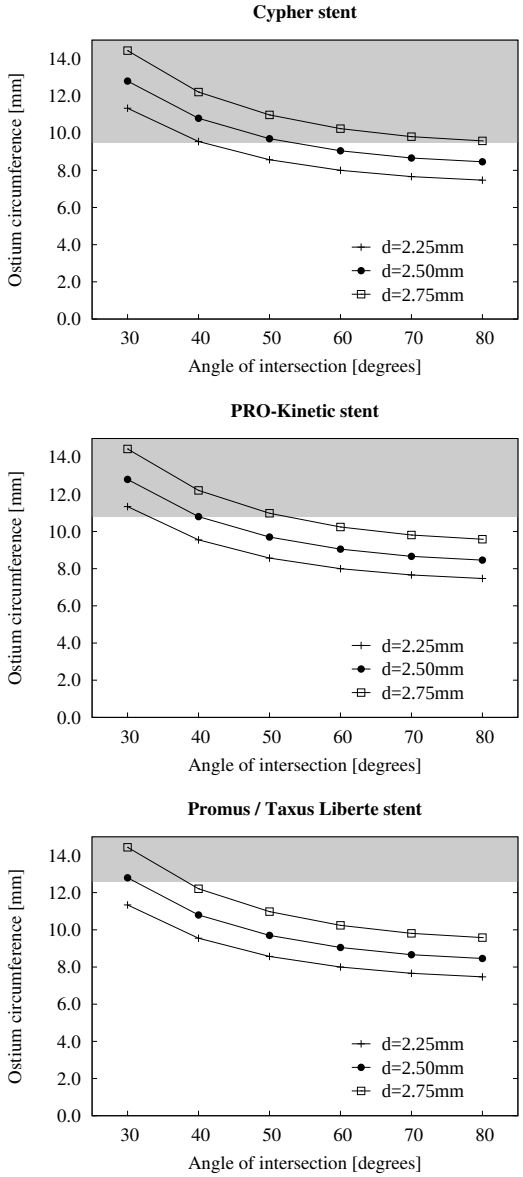

Figure 5.6: The grey zones indicate the cases in which the ostium circumference is larger than the cell circumference when the stents are deployed in a 3 mm MB (for three different SB sizes). Therefore, it is highly likely that in these cases (i.e. cases within grey zone) the cells will not be sufficiently enlarged by balloon dilatation through the side. The Endeavor stent is not shown because the cells can be sufficiently enlarged in all cases.

Accurate geometrical information of the bifurcation (MB and SB diameters and angle) is very important in order to apply the presented stent selection method in clinical practice. The most critical parameter is the angle of intersection. Dedicated software may help to accurately determine this bifurcation angle [160].

Selecting stents with large openings will reduce the risk of limited side (or main) branch patency after dilating through the side, but using such stents may result in inferior wall scaffolding/coverage and larger tissue prolapse [161]. Besides the stent cell size, a large number of other stent properties influence the choice for a particular stent, such as flexibility, conformability, trackability and radial strength. Furthermore, such careful selection based on cell size does not guarantee optimal stent deformation as these stents are not developed to treat bifurcation lesions. There is clearly a need for dedicated devices allowing easy and safe treatment while providing optimal scaffolding and minimizing luminal obstruction.

5.1.5 Limitations

Although the proposed method gives additional information to interventional cardiologists, it should be stressed that selecting an appropriate stent is more complex than depicted by mathematical modelling. For example, bifurcation angles may change following stent implantation. In addition, stent selection in clinical practice is based on a large number of design aspects and cell size is only one of them (e.g. flexibility, radial strength, etc.).

It has been shown that strut fracture may occur after SB dilatation [87] at high pressures using a large balloon (e.g., 4 mm nominal diameter). Such behaviour is not taken into account by the proposed methodology, which uses the original (non-fractured) cells as input. However, strut fracture should be avoided since it has been suggested for peripheral vessels that stent fracture is related to higher restenosis rates [162].

The proposed criterion to select stents with a cell circumference which is larger than the ostium circumference is too strict in case of partial stent deployment within the SB as demonstrated in Fig. 5.7. This means that the criterion is worst-case and guarantees the selection of stents with sufficiently large openings independent of the deployment behaviour of the stent (partial deployment within side branch or not).

5.1.6 Conclusion

We applied an innovative measurement technique based on micro-CT images to assess cell sizes of five 3 mm stents, and observed a considerable variation. This should be taken into account when applying a particular bifurcation stenting technique for a specific lesion as the selection of a stent

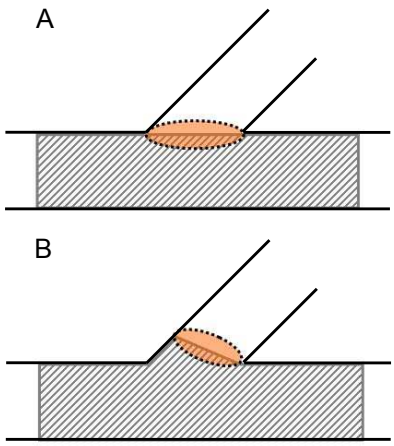

Figure 5.7: Panel A shows the worst-case situation which was used in this work (no partial stent deployment in the SB). This situation requires larger cells (at least as large as ostium) than in case of partial stent deployment in the SB (panel B).

with cells that are too small will inherently lead to suboptimal deployment and obstructing struts.

5.2 Strut density

5.2.1 Introduction

The cell size is not the only important design parameter for bifurcation stenting. At the European Bifurcation Club in Prague (2008), dr. van Geuns (Erasmus Medical Center, Rotterdam, The Netherlands) mentioned that he experienced a different level of complexity when inserting a balloon catheter into the SB through the struts of a MB stent, depending on the implanted stent design. This could be explained by the observation that some stents lead to more obstructing struts at the SB ostium, as depicted in Fig. 5.8. Of course, the number of obstructing struts will also depend on the relative position of the stent with respect to the SB ostium. The degree of obstruction is related to the size of the gaps between individual struts. Some expanded stents display a high strut density, meaning that the gaps between the struts are small, while the Cypher Select leads to a lower strut density.

Beside the SB accessibility, the strut density also affects a number of other parameters, such as drug delivery, tissue scaffolding and balloon-artery con-

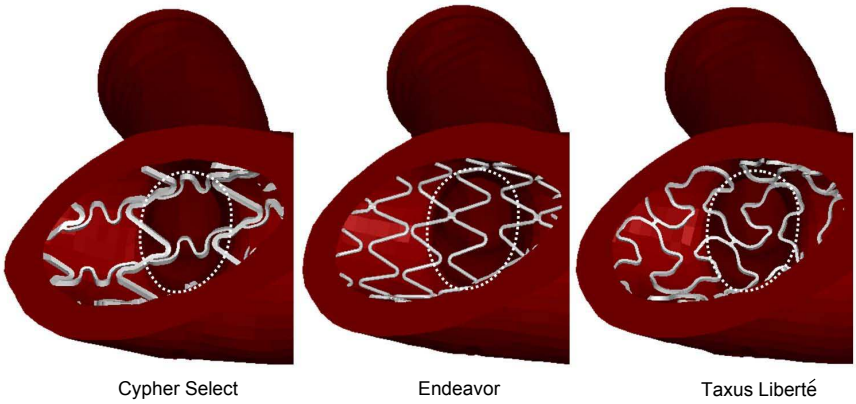

Figure 5.8: View into the SB after virtual implantation of three different DES in the MB. The number of struts at the SB ostium, which is indicated with a dotted line, is totally different for the three stent designs. Intuitively, it seems easier to advance a guide wire and a balloon catheter into the SB after implantation of the Cypher Select stent.

tact. Stent designs with a high strut density will lead to a more uniform drug delivery and will minimize the tissue prolapse between the struts. A higher strut density also reduces the contact area between the balloon and the endothelial cells. This is important since Squire [33] has shown that direct balloon-artery contact leads to endothelial denudation. This parameter clearly illustrates the conflicting design requirements which are often encountered. On one hand, strut density should be as high as possible for optimal drug delivery and tissue scaffolding, while on the other hand, good SB accessibility requires a low strut density.

A novel methodology is proposed to quantify the strut density, as this is an important design parameter. Different stent designs are compared and also the impact of the stent expansion diameter is investigated.

5.2.2 Materials and methods

Five coronary balloon-expandable '3 mm' stents were included in this study: the Taxus Liberté stent (Boston Scientific), the Cypher stent (Cordis, Johnson & Johnson), the Coroflex stent (BBraun), the Endeavor stent (Medtronic) and the Promus stent (Boston Scientific). Two micro-CT scans were performed on each crimped stent in order to get accurate geometrical information. The in-house built high resolution set-up at the UGCT facility [119] was used for the scans. All stents were first scanned at lower resolution (7 µm voxel pitch) in order to obtain the entire geometry of the

stents and subsequently at high resolution (1 µm voxel pitch) to obtain more detailed information on the stent strut dimensions.

The CT data was used to generate parametric models in pyFormex [130], which are easily adaptable and readily converted to high quality hexahedral meshes which are used for the finite element simulations in ABAQUS (Dassault Systèmes). A displacement driven simulation strategy was adopted to virtually expand the stents up to 3.5 mm inner diameter as shown in Fig. 5.9 for the Coroflex stent [126].

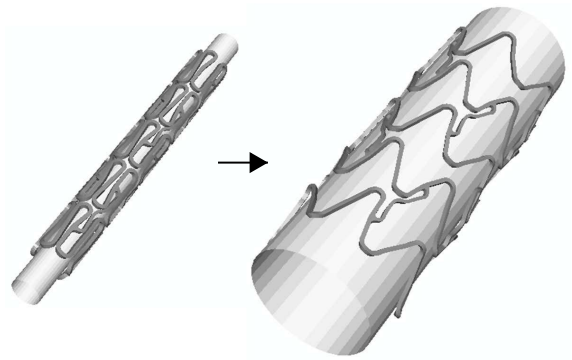

Figure 5.9: Illustration of the cylindrical, displacement driven expansion procedure for the Coroflex stent. The crimped stent is shown in the left panel, while the right panel depicts the deformed stent when the cylindrical tube has a diameter of 3 mm.

The strut density was quantitatively analyzed by calculating the maximum inscribed circle for a deformed, unrolled cell of the virtually expanded stent. This approach clearly has a number of limitations but is straightforward to calculate. The most important disadvantage is that stent A with completely circular cells with a certain radius R will have the same maximum inscribed circle as design B with ellipsoid cells with small radius R. Although both designs have the same maximum inscribed circles, design B will lead to more tissue protrusion and lower drug concentrations.

The maximum inscribed circle was determined for every output frame and thus the strut density could be monitored as a function of the stent diameter. The main steps to calculate the maximum inscribed circle are listed below:

1. A deformed stent cell was selected and unrolled in order to obtain a planar curve.
2. A regular grid was generated within the bounding box of the unrolled cell.
3. The set of grid points was split into two subsets, the points within the cell and the points outside the cell.

4. For every point lying within the cell, the minimal distance from that point to the stent cell was calculated. This gives a list with minimal distance values.

5. From the list with the minimal distance values, the maximum value gives the radius of the maximum inscribed circle.

The grid density was increased until the radius of the maximum inscribed circle converged. The applied procedure to determine the maximum inscribed circle is illustrated in Fig. 5.10.

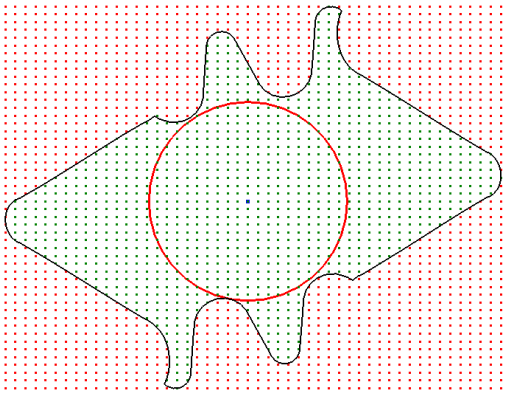

Figure 5.10: Illustration of the procedure to determine the maximum inscribed circle for the Cypher stent. The black line represents an unrolled stent cell at a stent diameter of 3 mm. The generated regular grid of points is divided into the points within (green) and outside (red) the cell. From all inner points, the point lying at the maximum distance from the cell is selected. This point is the center of the maximum inscribed circle. The grid used to generate this figure is clearly not fine enough, since the circle only touches the cell at one location.

5.2.3 Results and discussion

The basic principle of all balloon-expandable stents is identical. Inflation of a balloon leads to an important diameter increase of a cylindrical (mostly metal) strut pattern by plastic deformation. But the number of possible strut patterns is almost infinite, and this leads to important differences in the (mechanical) characteristics of these types of stents. This is also reflected in Fig. 5.11, which shows the deformed cells and the associated maximum inscribed circles at a stent diameter of 3 mm. Analyzing one cell per stent seems sufficient for these stents, since they have a very regular design with one type of cell. In addition, the displacement driven expansion mechanism leads to almost identical deformations of all the cells. This is,

of course, a simplification of reality, since non-uniform stent deformations occur, caused for example by the folded shape of the balloon and the non-uniform stent deformation after crimping.

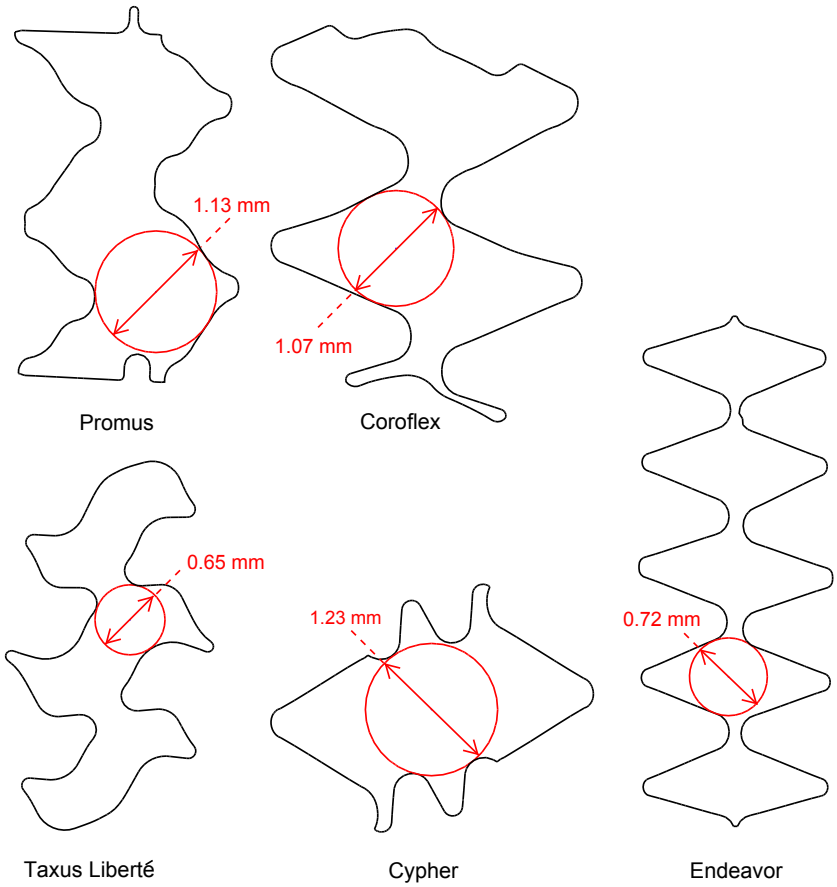

Figure 5.11: Comparison of the deformed cells of the five investigated stents at an inner stent diameter of 3 mm. The maximum inscribed circle and the corresponding diameter are drawn in red.

Figure 5.11 only shows the cell deformation for one particular stent diameter (i.e., 3 mm), but stents may be underexpanded or overdilated in clinical practice. Therefore, it is important to know how the cells deform and how the maximum inscribed circles change when the stent diameter varies. Figure 5.12 shows the deformed cell of the Taxus Liberté stent at a diameter of 2.5, 3.0 and 3.5 mm. The diameter of the maximum inscribed circle increases considerably as the individual struts tend to move away from each other.

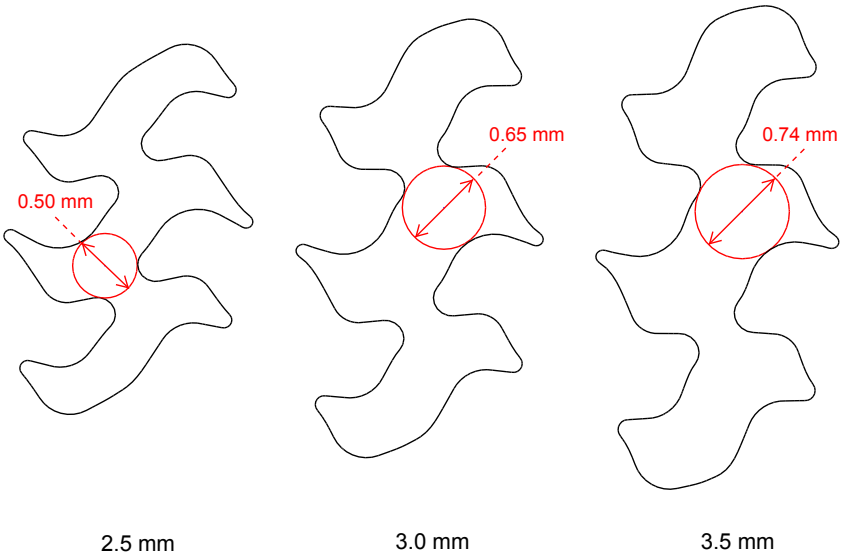

Figure 5.12: Comparison of the deformed cell of the Taxus Liberté stent at different stent diameters. The corresponding stent diameter is indicated below every cell.

The observation that the diameter of the maximum inscribed circle increases when the stent diameter enlarges is true for all investigated stents as quantitatively illustrated in Fig. 5.13 since the slope of all the curves is positive. This observation has an important clinical consequence as it means that an overdilation of the main vessel stent may facilitate guide wire and balloon catheter introduction into the SB. Ideally, this should be done by postdilating the expanded stent with a short dedicated balloon in order to minimize the arterial trauma. This effect may be less pronounced for the Promus stent, since the strut density seems quite constant in the considered stent diameter interval. A constant strut density may be preferred for unbranched vessels since this results in the same amount of tissue scaffolding, independent of the stent diameter. Figure 5.13 also shows that the strut density is markedly higher for the Endeavor and Taxus Liberté stent. Advancing a balloon catheter through the struts of these cells may be more difficult then for the other three stents.

5.2.4 Limitations

This purely geometrical analysis clearly has a number of limitations. The maximum inscribed circle gives some information about strut density, but

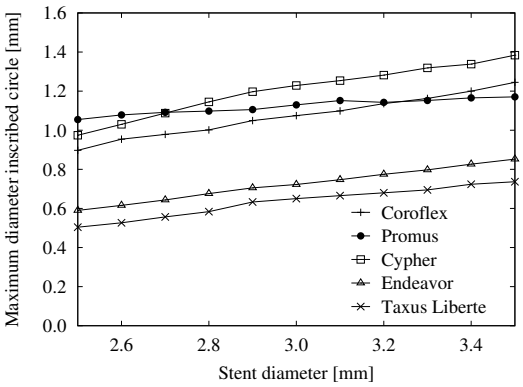

Figure 5.13: Quantitative comparison of the impact of the stent diameter on the strut density which is here reflected by the diameter of the maximum inscribed circle.

does not take into account some other aspects which also might have an impact on the SB accessibility. For example, a particular stent design can have cells with a large maximum inscribed circle with a lot of struts between the individual cells. If one of the cells is aligned with the SB ostium, then it should be relatively easy to insert a balloon catheter into the SB. But, on the other hand, when one of the zones between these large cells is positioned at the SB ostium, then the SB accessibility will be much lower. In addition, the side branch accessibility may also be influenced by the stent material, strut thickness and strut shape.

Strut deformations during the insertion of the SB balloon catheter through the MB stent were neglected. However, this insertion might exert forces on some struts and lead to strut deformations and improved SB accessibility. Parameters such as strut thickness and stent material will probably have an effect on these deformations.

5.2.5 Conclusions

Strut density is an important design parameter which affects the SB accessibility during provisional stenting, drug delivery and tissue scaffolding. An attempt was made to quantify the strut density of five different stents by calculating the maximum inscribed circle for the deformed stent cells. This parameter varied considerably among the considered stents. An important observation is that the size of the maximum inscribed circle increases when the stent diameter enlarges. Translated into practice, this means that over-expansion may help to advance a balloon catheter into the SB after stenting the MB.

Chapter 6

Virtual investigation of a novel provisional bifurcation stent system

THE usefulness of the developed finite element simulation techniques was clearly demonstrated in the previous chapters, where they were applied in the field of bifurcation stenting to compare different existing stent designs. But besides using these models to better understand the mechanics of currently available stents, they can also be incorporated in the design process of new devices to perform virtual prototyping and design optimization. This virtual approach can lead to a reduced time-to-market and to better performing device designs as it avoids the need to manufacture every design iteration and provides a better understanding of the device mechanics, especially when the device dimensions are small as is the case for stents. This is illustrated in this chapter where finite element simulations were employed during the initial design phase of a novel provisional bifurcation stent system[1].

6.1 Introduction

6.1.1 Current limitations of provisional stenting

Although the provisional approach is currently the gold standard to treat bifurcation lesions, it still faces a number of challenges. First, recrossing

[1] There is a conflict of interest regarding the study described in this chapter, as it is based on investigations carried out as a consultancy project for Boston Scientific.

into the SB with a guide wire and balloon catheter to perform final kissing balloon inflation can sometimes be time consuming due to the obstructing floating struts at the SB ostium. This was discussed in chapter 5 where the strut density of different expanded stents was compared. A lower strut density improves the SB accessibility but negatively affects the drug delivery and tissue scaffolding. This immediately leads to the second limitation of using current DES for provisional stenting. If the proximal or distal MB diameter is used to determine the stent diameter, then the stent will be overexpanded in the bifurcation region where the vessel cross-section is much larger. This leads to a lower strut density in the bifurcation region as compared to the proximal and distal segment and therefore, results in suboptimal tissue scaffolding and drug delivery. A denser packing of the struts is required in the bifurcation region in order to obtain the same level of tissue scaffolding after final kissing balloon inflation as compared to the proximal and distal section. This obviously leads to conflicting design requirements with respect to the SB accessibility. A denser packing of the struts will lead to a higher strut density after the initial MB stent expansion and thus increase the degree of obstruction at the SB ostium. The third limitation is related to the introduction of the guide wire into the SB. It has been shown by bench testing that this wire has to be advanced through the most distal cell at the SB ostium in order to obtain optimal strut positioning after final kissing balloon inflation [163]. However, doing this in clinical practice may not always be obvious.

In order to minimize the previously mentioned limitations, Boston Scientific currently investigates the feasibility of a novel dedicated stent design and procedure for provisional stenting, that has been developed in conjunction with dr. Sjögren (Falun Hospital, Falun, Sweden).

6.1.2 Dedicated bifurcation stent design

The design of the dedicated bifurcation stent is based on the Liberté stent (Boston Scientific, Natick, MA, USA), though has an adapted denser strut pattern in the central stent region. The ring elements in this central zone (one ring is indicated with a red line in Fig. 6.1) can be expanded to a larger diameter as compared to the ring elements in the distal and proximal stent sections because the circumference of these rings is larger. Therefore, this central part of the stent should be positioned at the bifurcation ostium. Within this denser central part, the circumference of the ring elements gradually increases from the proximal to the distal side in order to provide optimal ostium scaffolding. The distal and proximal stent sections are identical to the Liberté design. The complete single wire stent system is further characterized by a low crossing profile (similar to conventional stents), and does not require rotational orientation.

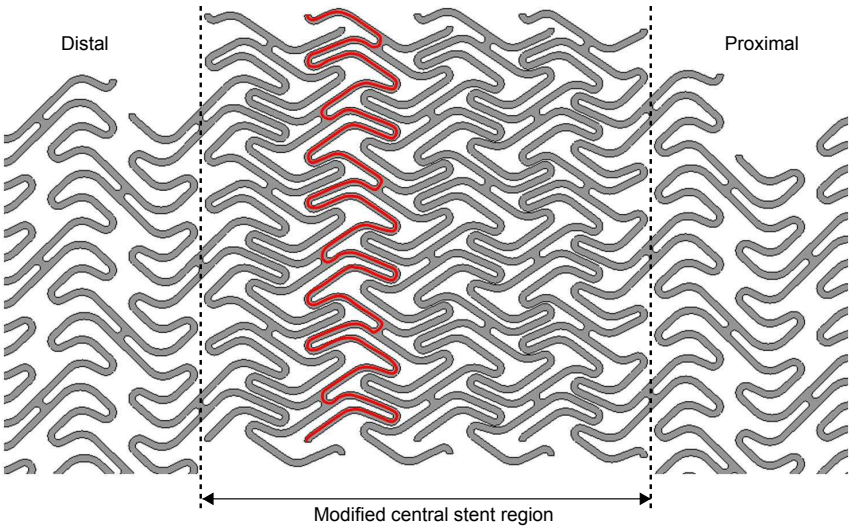

Figure 6.1: Unrolled bifurcation stent geometry which is based on the Liberté design with an altered central strut pattern. One ring element in the central zone is indicated with a red line. The length of this red line or ring element is larger then the length of similar ring elements in the distal or proximal zone. Therefore, the central part can be expanded to a larger diameter which is necessary at the location of the bifurcation in order to provide at least partial support to the SB.

6.1.3 Bifurcation stenting procedure

In an attempt to overcome the current limitations of provisional stenting, Boston Scientific investigates the feasibility of applying a slightly modified provisional stenting procedure which involves the following steps:

- First, the dedicated stent is deployed within the MB using a standard non-compliant 72D PEBAX balloon (i.e. provisional stenting).
- During a second step, a dedicated balloon (a compliant 63D PEBAX balloon or a bulge balloon) will be inflated within the already expanded stent with the aim of (i) causing strut protrusion within the SB, hereby improving the SB accessibility; (ii) providing ostium scaffolding and (iii) facilitating guide wire and balloon catheter insertion through a distal cell at the ostium as this is not always trivial in current clinical practice.
- Finally, single or kissing balloon inflation should be performed to push all struts against the vessel wall. In some cases, it might be necessary to implant a second stent in the SB.

6.1.4 Objectives

The previously described device and procedure was investigated using finite element simulations in which balloon materials and size, inflation pressure, stent design and target vessel geometry were varied with the aim of assessing the most important design and or procedural parameters. Furthermore, the impact of small positioning inaccuracies was investigated.

6.2 Materials and methods

6.2.1 Geometrical models

6.2.1.1 Stent

The unrolled geometrical model[2] of the dedicated bifurcation stent is depicted in Fig. 6.1. This CAD model was imported into pyFormex [130] and subsequently approximated by a hexahedral mesh which was created using a sweep based meshing approach. Finally, the cylindrical stent structure was obtained by performing a mathematical transformation of the nodal coordinates of each element.

6.2.1.2 Balloon

Three balloon geometries were created (see Fig. 6.2): (i) The bifurcation stent is crimped on a non-compliant 72D PEBAX balloon (3.31 mm initial diameter, 3.5 mm nominal diameter, 16 mm length), which is pleated with 5 folds around the catheter. During a first step, a hybrid mesh (i.e. both triangular and quadrilateral elements) of the unfolded balloon was created using pyFormex. Subsequently, a mathematical transformation as described by Laroche et al. [123] was used to obtain the 5-folded balloon. (ii) An identical method was used to generate the folded geometry of a compliant 63D PEBAX balloon (4.24 mm initial diameter, 4.5 mm nominal diameter, 8 mm length). (iii) The unfolded geometry of the bulge balloon was created with ABAQUS/CAE (a folded configuration was not necessary for both the compliant and the bulge balloon as these balloons are inflated within an already expanded stent). A uniform wall thickness of 17.78 µm was assumed for all the investigated balloons[3].

[2] Data provided by Boston Scientific

[3] Data provided by Boston Scientific

Figure 6.2: Non-inflated unfolded balloon geometries (left panel: standard non-compliant 72D PEBAX balloon, middle panel: compliant 63D PEBAX balloon, right panel: non-compliant bulge balloon). The scale of the different balloons is not exactly the same.

6.2.1.3 Arterial bifurcation

The hexahedral meshes of the bifurcation models were created using the isoparametric transformations, which are implemented in pyFormex. The reference bifurcation model has a proximal MB diameter of 3.5 mm, a distal MB diameter of 2.8 mm and a SB diameter of 2.4 mm which is in accordance with the anatomical analysis of Finet et al. [11]. The bifurcation angle is 50 degrees and the outer diameter was determined as 1.6 times the inner diameter [12]. The complete bifurcation is shown in Fig. 6.3.

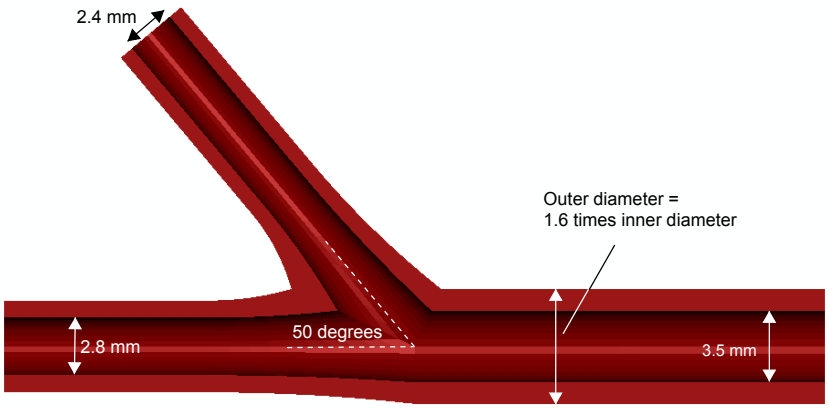

Figure 6.3: Reference bifurcation model.

6.2.2 Constitutive models

6.2.2.1 Stent

The bifurcation stent is made of stainless steel, which is characterized by a Young's modulus of 213756 MPa, a Poisson's ratio of 0.25 and a yield stress of 210 MPa.

6.2.2.2 Balloons

The applied constitutive models of the three balloons are based on the experimentally observed pressure/diameter relationship of each balloon[4]. The methodology to derive the material behaviour from pressure/diameter data is based on the thin shell membrane theory [94, 126, 127]. The Poisson's ratio was assumed to be 0.4 for all balloons and the resulting elastic material properties are summarized in Table 6.1. Since the material of the non-compliant bulge balloon is identical to the one of the standard non-compliant balloon used for the initial stent expansion, it was expected to obtain a similar Young's modulus (i.e. 970 MPa). However, using a Young's modulus of 970 MPa makes the bulge balloon too stiff as compared to the experimental data provided by Boston Scientific. This is probably related to the manufacturing procedure of the bulge balloon, which may result in modified material properties and/or membrane thickness. Using a value of 700 MPa provided pressure-diameter data matching the experimental data. As such, a value of 700 MPa was further assumed.

Table 6.1: The material properties of each balloon were calculated based on the provided pressure/diameter data. This calculation results in stress/strain data, which are approximated by a Young's modulus. However, the compliant balloon demonstrates a considerable non-linear behaviour, and therefore, the constitutive behaviour is approximated by a first Young's modulus in the low pressure range (i.e. 465 MPa) and a second Young's modulus in the high pressure range (i.e. 700 MPa).

Balloon	Young's modulus [MPa]
non-compliant 72D PEBAX balloon	970
compliant 63D PEBAX balloon (low pressures)	465
compliant 63D PEBAX balloon (high pressures)	700
non-compliant 72D PEBAX bulge balloon	700

6.2.2.3 Arterial wall

The arterial wall behaviour was modelled using a homogeneous hyperelastic law as described by Prendergast et al. [136]. The strain energy function has a polynomial structure of the third order and the non-zero coefficients are given in Table 6.2.

[4] Data provided by Boston Scientific

Table 6.2: Non-zero coefficients of the third order polynomial strain energy function used to describe the mechanical behaviour of the arterial wall (according to the ABAQUS conventions).

C_{10}	0.0189
C_{01}	0.00275
C_{20}	0.59043
C_{11}	0.08572

6.2.3 Discretization

The finite element mesh of the stent model consisted of 33444 8-node hexahedral elements with reduced integration (C3D8R). The same element type was chosen for the arterial wall mesh, which contains 5760 hexahedrons. The balloons were meshed with membrane type elements and both triangular (M3D3) and quadrilateral elements were used (M3D4). The mesh of the non-compliant 72D PEBAX balloon consisted of 11305 M3D4 and 2640 M3D3 elements, whereas the compliant 63D PEBAX balloon model contained 7370 M3D4 and 4590 M3D3 elements. Only quadrilateral M3D4 elements were used to mesh the non-compliant 72D PEBAX bulge balloon (i.e. 5796 elements).

6.2.4 Simulation steps

ABAQUS/Explicit was used to solve the large deformation problems, as this solver provides a very stable general contact algorithm. A static friction coefficient of 0.2 was used to define all contacts. This penalty factor is acceptable for steel-steel and nylon-steel contact [94]. The friction coefficient for stent-artery interactions however is unknown, though assuming frictionless behaviour would also be incorrect. The balloon and arterial ends were completely constrained during the analyses. No boundary conditions were imposed on the stent.

The simulation of the complete bifurcation stenting procedure was performed in a number of steps (see Fig. 6.4):

1. The stent is crimped on the folded balloon by reducing the diameter of a semi-rigid cylinder.

2. A gradually increasing pressure acts on the inner surface of the folded balloon in order to expand the crimped stent in the bifurcated blood vessel. After reaching the maximum (i.e. 1.8 MPa), the pressure was slowly removed to account for the recoil of the system.

3. The unfolding of the balloons (i.e. bulge and compliant balloon) used for the postdilatation was not simulated in order to decrease the complexity of the computations. The diameter of the unfolded unpressurized balloon geometry was decreased by reducing the diameter of a semi-rigid cylinder. This was necessary as the unfolded balloon diameter was larger then the expanded stent diameter.

4. Finally, the postdilatation balloon was gradually inflated and subsequently deflated.

The semi-rigid cylinders used for the crimping of the stent and for the diameter reduction of the bulge balloon are not shown in Fig. 6.4 in order not to overload the figure.

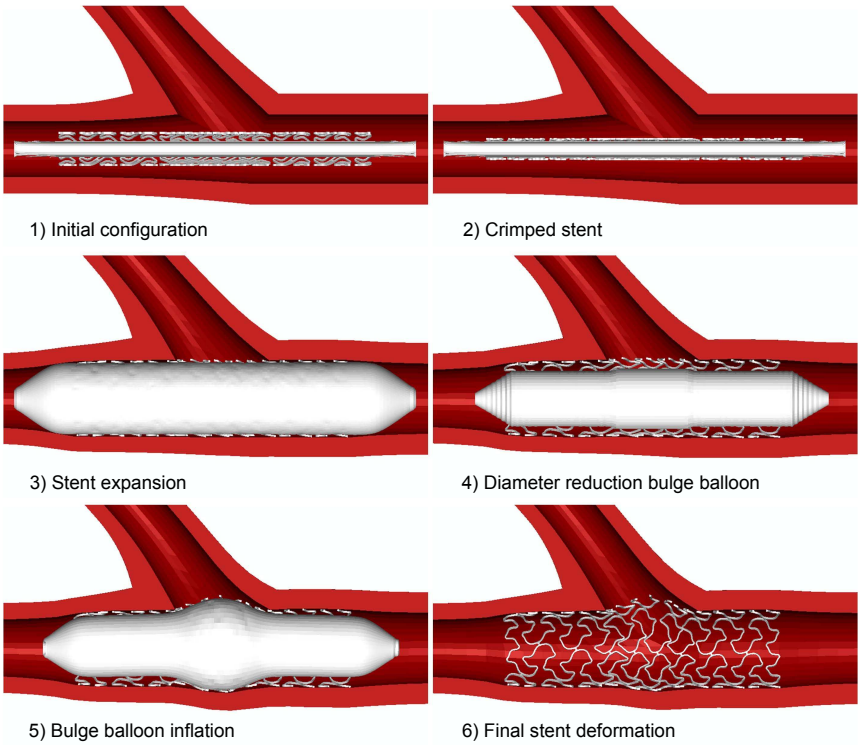

Figure 6.4: Schematic overview of the different simulation steps.

6.2.5 Finite element simulations

First, the accuracy of both the simulations and the calculated balloon material models was verified. Therefore, all three balloon models were inflated

and the compliance behaviour (i.e. pressure-diameter relation) was compared with experimental data[5]. Similarly, the free stent expansion was validated using experimental pressure-diameter data. Finally, the expansion of the stent within a rigid bifurcation (the diameter of all branches was 3 mm and a bifurcation angle of 45 degrees) followed by a postdilatation with the non-compliant bulge balloon was simulated. The same procedure was carried out experimentally in a similar rigid in vitro model. The resulting strut protrusions into the SB are compared to assess the accuracy of the finite element simulation of the complete bifurcation stenting procedure.

Based on preliminary animal experiments and on two simulations comparing the non-compliant bulge balloon with the compliant balloon for postdilating the expanded stent (see section 6.4), Boston Scientific decided to only continue with the compliant balloon in the subsequent investigation and optimization phase. In this final phase, the effect of the following design and procedural parameters was quantified:

- Stent design: the stiffness of central stent region was decreased by reducing the strut width in that area to 60 and 80 percent of the original strut width (see Fig. 6.5).

- Pressure: the maximum inflation pressure within the compliant balloon was modified (0.8, 1.1, and 1.4 MPa).

- Balloon size: compliant balloons with different sizes were compared (initial diameter 4.0, 4.24 and 4.5 mm).

- Balloon compliance: the Young's modulus of the compliant balloon was varied (Young's modulus of 400, 500, 600 and 700 MPa).

- Bifurcation anatomy: both the impact of bifurcation angle and vessel diameters was investigated by comparing the bifurcation stenting technique for six bifurcation models (see Table 6.3 and Fig. 6.6). All bifurcation models are in accordance with the anatomical data of Finet et al. [11].

- Positioning inaccuracies: two simulations were performed to examine the impact of inaccurate placement. In the first one, the stent was translated over 4 mm resulting in misplacement of the central stent zone. This modified part of the stent design was then no longer located at the bifurcation ostium. During a second simulation, the stent was accurately positioned but the compliant balloon was translated over 6 mm.

[5] Data provided by Boston Scientific

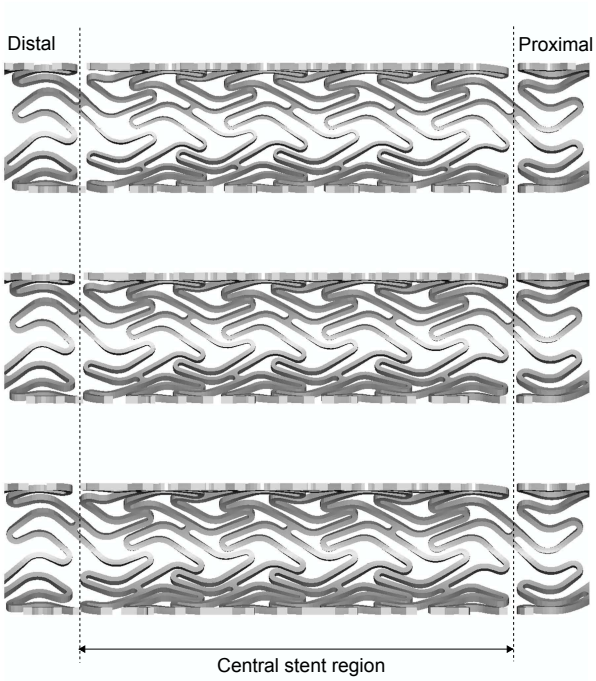

Figure 6.5: The three depicted stent designs have a different strut width in the central stent region, but the distal and proximal ends are identical. The upper panel shows the design where the strut width has been reduced to 60 percent of the original width, whereas the middle panel shows the design with a reduction to 80 percent of the original width. The bottom panel depicts the original design as shown in Fig. 6.1 without reduced strut width.

Unless otherwise stated, the stent is expanded in the reference bifurcation model (see Table 6.3) and the postdilatation is carried out using a compliant balloon with an initial diameter of 4.24 mm and a Young's modulus of 700 MPa.

6.2.6 Postprocessing

Comparison and quantification of different design and/or procedural parameters requires the introduction of operator independent criteria. As the aim of postdilatation is to obtain partial ostium scaffolding and strut protrusion into the SB, a first new quantification parameter is introduced: the maximal strut protrusion (MSP). The MSP is the maximum distance from the centerline of the MB to a stent strut at the location of the ostium minus the radius of the proximal main vessel. Figure 6.7 shows the MSP schematically.

Table 6.3: Overview of the investigated bifurcation models (D_{PMB} = proximal MB diameter, D_{DMB} = distal MB diameter, D_{SB} = SB diameter). The model abbreviation is related to the model size (Small, Medium and Large) in combination with the bifurcation angle (50 or 80). The reference bifurcation model is indicated in bold (i.e. M50).

D_{PMB} / D_{DMB} / D_{SB}	50 degrees bifurcation angle	80 degrees bifurcation angle
3.0 mm / 2.4 mm / 2.0 mm	S50	S80
3.5 mm / 2.8 mm / 2.4 mm	**M50**	M80
4.0 mm / 3.2 mm / 2.7 mm	L50	L80

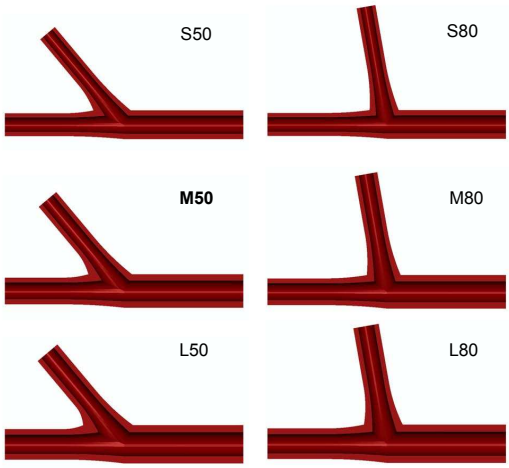

Figure 6.6: Overview of the different bifurcation models (the abbreviations are explained in Table 6.3).

A second quantification parameter reflects the overdilatation of the distal MB, because using an oversized compliant balloon at too high pressure might result in too large distal MB diameters and potentially in rupture of the vessel. Therefore, the overdilatation coefficient (OC) is the percentage increase of the distal MB diameter:

$$OC = \frac{D_{DMB,post} - D_{DMB,pre}}{D_{DMB,pre}} \tag{6.1}$$

$D_{DMB,pre}$ is the distal MB diameter prior to stenting, whereas $D_{DMB,post}$

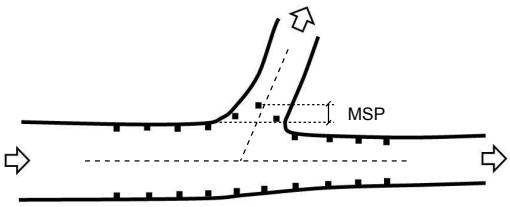

Figure 6.7: Schematic illustration of the maximal strut protrusion (MSP). The MSP is the maximal distance from the axis of the main vessel to a stent strut at the SB ostium minus the radius of the proximal main vessel.

is the distal MB diameter after stenting and subsequent postdilatation. This distal MB diameter is measured 7 mm distal to the bifurcation center as indicated in Fig. 6.8.

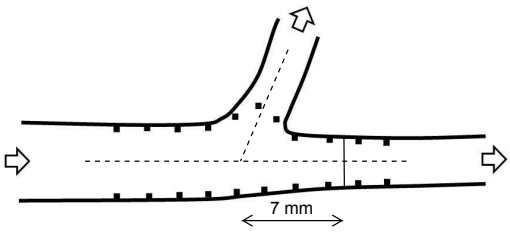

Figure 6.8: Schematic illustration of the overdilatation coefficient (OC). The vertical line within the distal MB indicates the cross section used for the calculation of the overdilatation coefficient (OC).

6.3 Validation of the finite element simulations

6.3.1 Validation of free balloon expansion

The calculated material properties for all balloons were validated by comparing the numerical results of a free balloon expansion with experimental data (i.e. pressure-diameter relationship)[6].

[6] Data provided by Boston Scientific

6.3.1.1 Non-compliant 72D PEBAX balloon

The validation of the compliance behaviour of the non-compliant 72D PEBAX balloon is depicted in Fig. 6.9. The maximum percentage difference in diameter is less than 6 percent and occurs at a pressure of 0.1 MPa. At this pressure, the balloon is already unfolded but is still in a transient state as shown in Fig. 6.9 (right panel). The experimental values and the numerically predicted behaviour correspond well in the low (between 0.2 and 0.6 MPa) and high pressure range (above 1.6 MPa). However, at average pressures, the numerically predicted diameters underestimate the experimentally determined diameter and this is probably the result of the linear elastic material behaviour that was assigned to the balloon membrane (for detailed information about this linear elastic approximation, please see [94]).

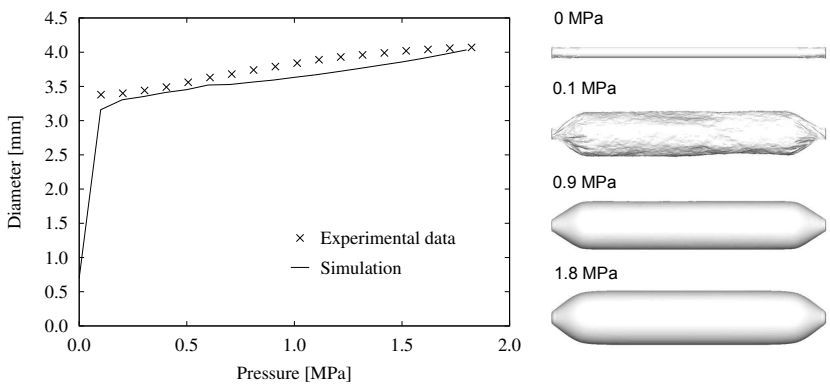

Figure 6.9: Comparison of the experimental data with the numerical results for the non-compliant 72D PEBAX balloon.

6.3.1.2 Compliant 63D PEBAX balloon

The validation of the compliance behaviour of the compliant 63D PEBAX balloon is depicted in Fig. 6.10. This compliant balloon material can not be accurately approximated by a single elastic modulus as it is highly non linear. As introducing hyperelastic material models increases the complexity and computational cost, two Young's moduli were used. A first one (465 MPa) was chosen in order to obtain acceptable compliance behaviour in the low pressure range (i.e. pressure below 0.8 MPa) and a second one (700 MPa) that resulted in a good match for high pressures (i.e. pressure above 0.8 MPa).

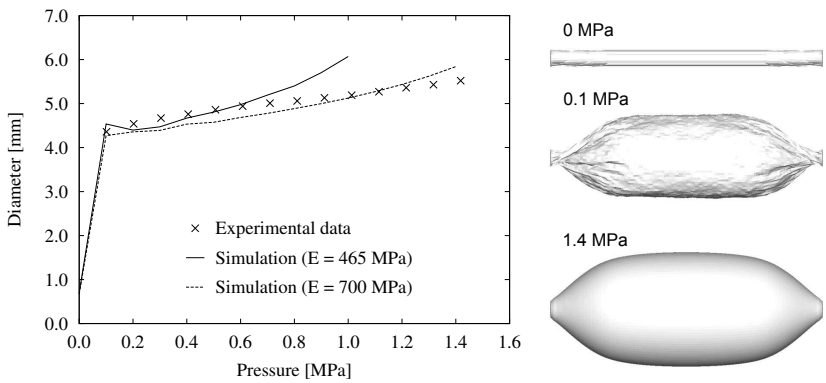

Figure 6.10: Comparison of the experimental data (filled diamonds) with the numerical results (solid line corresponds with a Young's modulus of 465 MPa, the dashed line corresponds with a Young's modulus of 700 MPa). The balloon unfolding and stretching is shown on the right for the simulation with the Young's modulus of 700 MPa.

6.3.1.3 Non-compliant 72D PEBAX bulge balloon

The validation of the compliance behaviour of the non-compliant 72D PEBAX bulge balloon is depicted in Fig. 6.11. The maximum diameter of the bulge balloon was used. The maximum percentage difference in diameter is 2 percent and occurs at a pressure of 1.4 MPa.

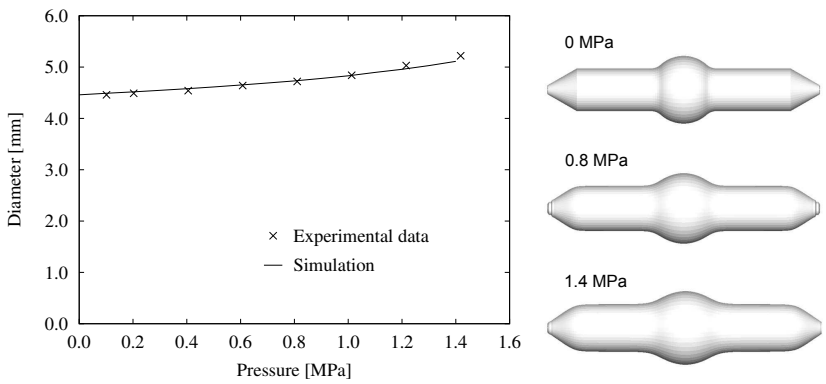

Figure 6.11: Comparison of the experimental data with the numerical results. The diameter refers to the maximum diameter of the bulge balloon.

6.3.2 Validation of free stent expansion

The validation of the free expansion (i.e. pressure-diameter relationship) of the dedicated stent using the non-compliant 72D PEBAX balloon is depicted in Fig. 6.12. The maximum percentage difference in diameter is 3 percent and occurs at a pressure of 0.8 MPa. Although there was a small discrepancy between the numerical and experimental compliance behaviour of the balloon itself (see section 6.3.1.1), the simulated compliance behaviour of the balloon-stent system corresponds well with the experimental data.

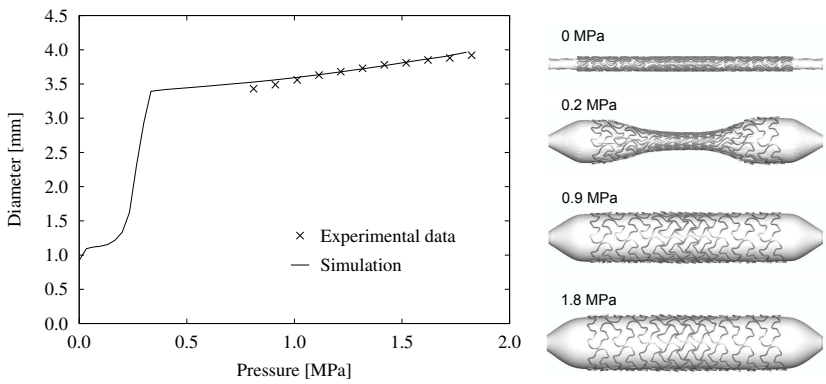

Figure 6.12: Comparison of the experimental data with the numerical results.

6.3.3 In vitro validation of the complete bifurcation stenting procedure

The dedicated bifurcation stent was numerically and experimentally deployed within a rigid bifurcation model. After inflation of the bulge balloon (1.0 MPa) within the deployed stent, the maximal stent diameter was measured. For the in-vitro experiment which was only performed once, this diameter was equal to 3.56 mm. The numerically predicted maximum stent diameter was equal to 3.66 mm. Consequently, we concluded that the complete procedure (including postdilatation with a dedicated balloon) can be simulated with good accuracy (see Fig. 6.13).

6.4 Strut protrusion: compliant versus bulge balloon

Inflating both the bulge and the compliant balloon at 1.1 MPa within an already expanded stent (in bifurcation M50) clearly reveals the major dif-

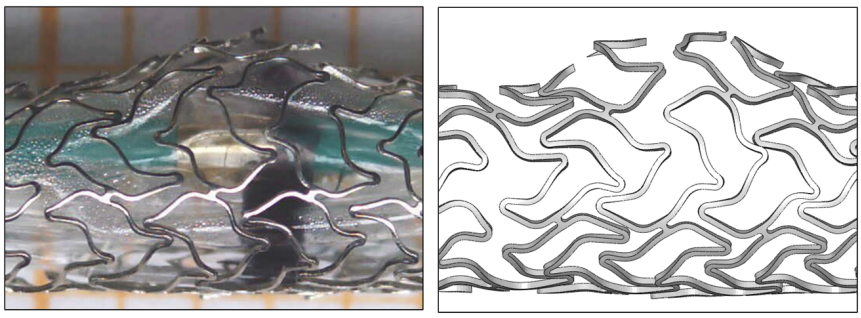

Figure 6.13: Comparison of the experiment (left panel) with the numerical results (right panel). Due to a different initial position of the expanded stent in the experiment and in the simulation, it is difficult to identify the corresponding stent struts.

ferences between both approaches (see Fig. 6.14). Using the bulge balloon results in a local overdilatation of the parent vessel, whereas the overdilatation after inflating the compliant balloon affects a larger vessel section. A local overdilatation may cause additional damage to the vessel wall and unwanted disturbances of the blood flow. In addition, using the bulge balloon results in floating stent struts which are not in contact with the vessel wall (indicated in Fig. 6.14). Such floating struts should be avoided as they increase the thrombosis risk, reduce the effectiveness of the drug release in case of drug eluting stents and amplify the disturbance of the blood flow.

Furthermore, performing the investigated bifurcation stenting technique in vivo in porcine coronary arteries (these animal tests were carried out at the Erasmus MC, Rotterdam, The Netherlands) revealed another limitation of using the bulge balloon: it is extremely difficult to inflate this bulge balloon exactly at the location of the bifurcation. As observed by IVUS, small placement errors result in an overdilatation of the proximal or distal MB, and do not cause strut protrusion into the SB (cfr. meeting in Erasmus MC on 21 October 2008).

Based on the limitations of the bulge balloon that were observed both by computer simulations and by performing animal tests, Boston Scientific decided to abandon this bulge balloon and to only further investigate and optimize the compliant balloon for this study. The preliminary animal experiments also highlighted the importance of accurate selection of the balloon size and the applied pressure when using the compliant balloon. Too high pressures and too large balloons may result in excessive overdilatation. Therefore, the impact of the balloon size and pressure was investigated in the next section and the standard applied pressure for the compliant balloon was reduced to 0.8 MPa unless otherwise stated.

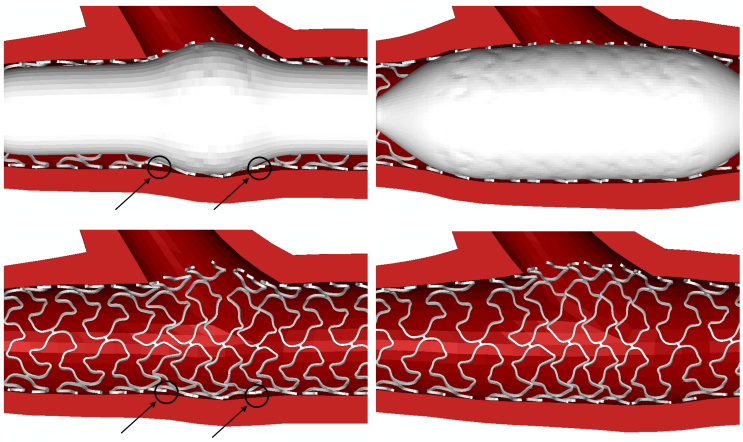

Figure 6.14: Comparison of the effect of postdilating the stent with a non-compliant bulge balloon (left side) or with a compliant balloon (right side). The upper panels show the stent deformation and the inflated balloons at 1.1 MPa. The final configuration after balloon deflation is depicted in the bottom panels. The circles indicate the floating stent struts (i.e. struts not in contact with the vessel wall).

6.5 Parametric analyses

The first part of this section contains qualitative information regarding the impact of a number of design and procedural parameters. Quantitative information (MSP and OC) are given at the end of the section for all simulations.

The M50 bifurcation model and the standard compliant balloon (initial diameter of 4.24 mm, a Young's modulus of 700 MPa and inflation at 0.8 MPa) will be used unless otherwise stated.

6.5.1 Stent geometry

The stiffness of the central stent section was decreased by reducing the strut width in this section to 60 and 80 percent of the original width (see Fig. 6.15). Reducing the strut width clearly improves the strut protrusion and ostium scaffolding as intuitively expected. Therefore, all simulations from now on are carried out with the modified design with a strut width reduction in the central section to 80 percent of the original width. Postdilatation at 0.8 MPa of this modified design with a compliant balloon (Young's modulus of 700 MPa, initial diameter of 4.24 mm) in the M50 bifurcation model will be termed 'reference simulation (or REF)'.

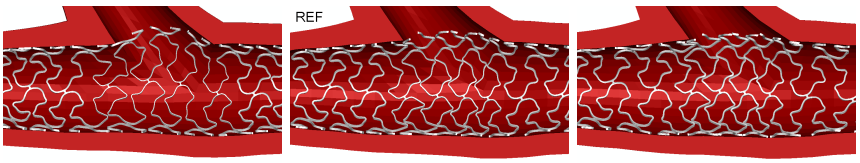

Figure 6.15: Impact of strut width reductions in the central stent section (left panel: reduction to 60 percent of the original width, middle panel: reduction to 80 percent of the original width, right panel: original design).

6.5.2 Balloon pressure

Increasing the maximal pressure in the compliant balloon improves the strut protrusion as depicted in Fig. 6.16, but as already mentioned, higher pressures probably increase the risk of excessive overdilatation. The initial balloon diameter (i.e. at zero pressure) and the Young's modulus were kept constant at respectively 4.24 mm and 700 MPa.

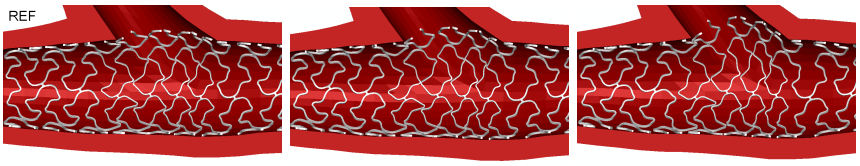

Figure 6.16: Impact of the inflation pressure (left panel: reference simulation with inflation at 0.8 MPa, middle panel: inflation at 1.1 MPa, right panel: inflation at 1.4 MPa).

6.5.3 Balloon size

Increasing the size of the compliant balloon improves the strut protrusion, but again, larger balloons might increase the risk of excessive overdilatation (see Fig. 6.17). The elastic modulus of the balloon and the inflation pressure were kept constant at respectively 700 MPa and 0.8 MPa.

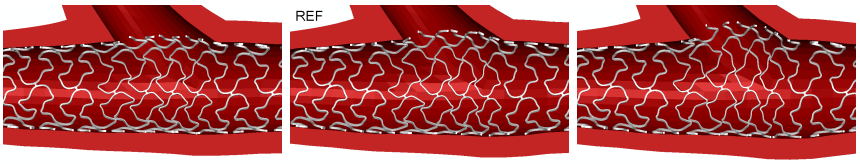

Figure 6.17: Impact of the balloon size (left panel: initial balloon diameter of 4 mm, middle panel: reference simulation with initial balloon diameter of 4.24 mm, right panel: initial balloon diameter of 4.5 mm).

6.5.4 Balloon compliance

Decreasing the stiffness of the compliant balloon (i.e. Young's modulus) improves the strut protrusion (see Fig. 6.18). The initial balloon diameter and the inflation pressure were kept constant at respectively 4.24 mm and 0.8 MPa.

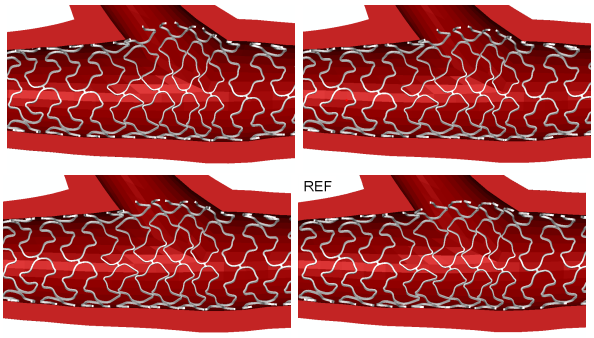

Figure 6.18: Impact of the balloon compliance (top left panel: elastic modulus of 400 MPa, top right panel: elastic modulus of 500 MPa, bottom left panel: elastic modulus of 600 MPa, bottom right panel: reference simulation with an elastic modulus of 700 MPa).

6.5.5 Impact of vessel anatomy

The same stent design and postdilatation procedure were applied using different bifurcation geometries. The strut protrusion is much more expressed when the same stent and compliant balloon are used in a smaller bifurcation (see Fig. 6.19). Logically, using oversized stents/balloons increases the risk of excessive overdilatation or vessel rupture. The bifurcation angle seems to have a minor impact on the strut protrusion.

6.5.6 Quantification

The previous sections clearly showed the impact of the different investigated parameters on the strut protrusion but the overview is purely qualitative and assessing the overdilatation is impossible. Therefore, the MSP and the OC were determined for every simulation (see Fig. 6.20 and 6.21) and analysis of these graphs provides the following information:

- Changing balloon parameters (size, compliance, pressure) has a larger effect on the MSP than reducing the strut width of the central stent section.
- Selecting an oversized balloon/stent for a particular bifurcation has a positive effect on the MSP but logically results in a larger OC.

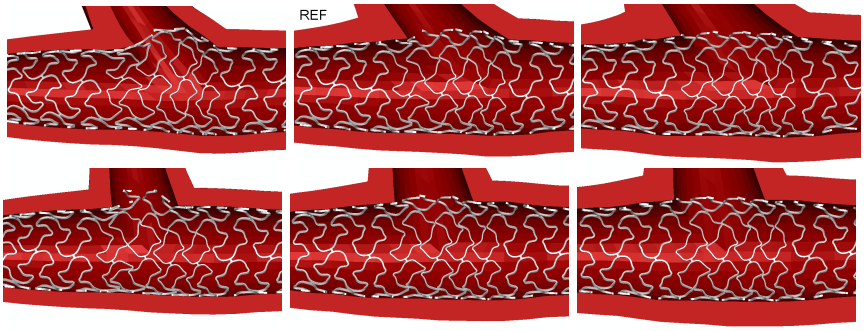

Figure 6.19: Impact of the bifurcation geometry (top left panel: S50, bottom left panel: S80, top middle panel: reference simulation with M50, bottom middle panel: M80, top right panel: L50, bottom right panel: L80).

- The OC seems insensitive to changes in the balloon or stent parameters. This is a limitation of the model that uses a purely hyperelastic model for the vessel wall. Consequently, effects such as permanent deformation due to remodelling or rupture are not included in the simulations. Using a higher pressure in a real vessel will cause more permanent deformation and/or rupture and therefore, this will enlarge the finally obtained lumen.

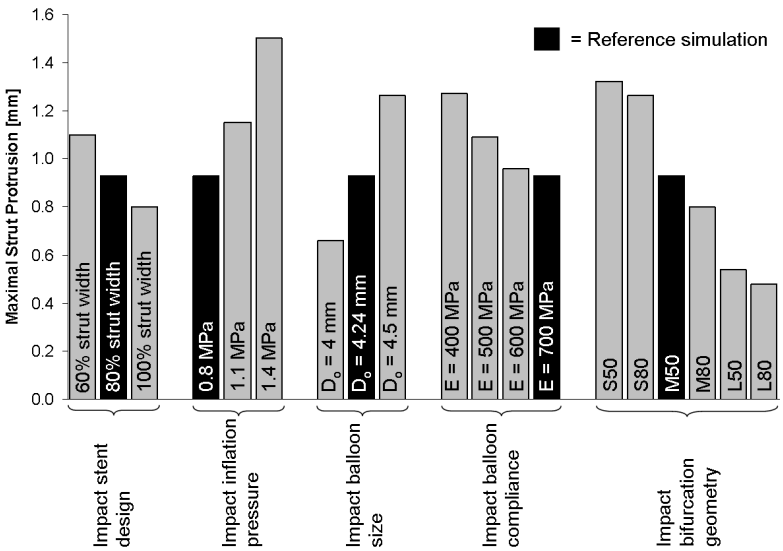

Figure 6.20: Maximal Strut Protusion (MSP) for all the simulations (D_o = original balloon diameter at zero pressure, E = Young's modulus)

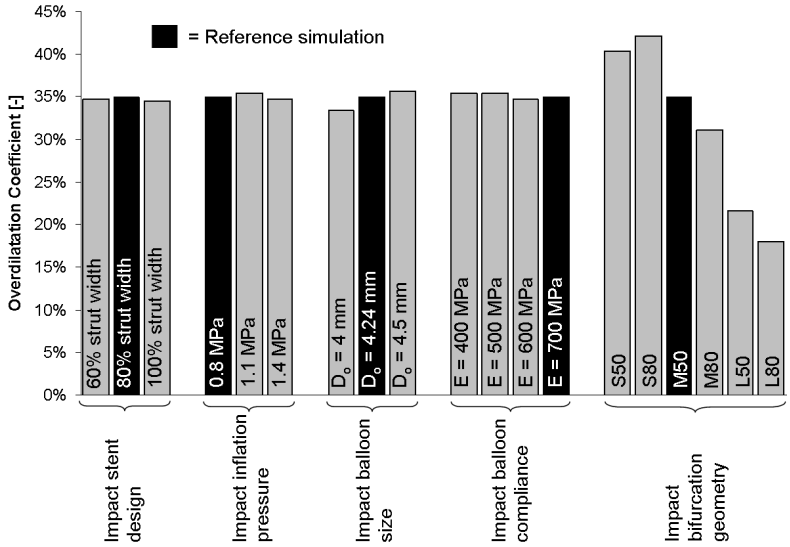

Figure 6.21: Overdilatation coefficient (OC) for all the simulations (D_o = original balloon diameter at zero pressure, E = Young's modulus)

6.6 Mechanism of strut protrusion

Figure 6.22 shows cross sectional views at the location of the bifurcation for the simulation in which the Young's modulus of the compliant balloon was reduced to 400 MPa. Deflating the compliant balloon results in an increased strut protrusion as indicated by the vertical line in figure 22. This interesting observation can be explained by the radial compression acting on the struts in contact with the parent vessel. As such compression is not acting on the struts pushed into the SB, the stent shape changes from circular to ellipsoid. No in-vivo imaging data were available to experimentally validate this observation.

6.7 Positioning inaccuracies

6.7.1 Impact of balloon misplacement

Inflating the compliant balloon not exactly at the location of the bifurcation yields minimal strut protrusion. In addition, such inaccurate placement may result in a considerable area with direct balloon-artery interaction outside the deployed stent (see Fig. 6.23). This is pure balloon angioplasty which is associated with high restenosis rates. It can be noticed that the section which was subjected to direct balloon contact springs back to its original

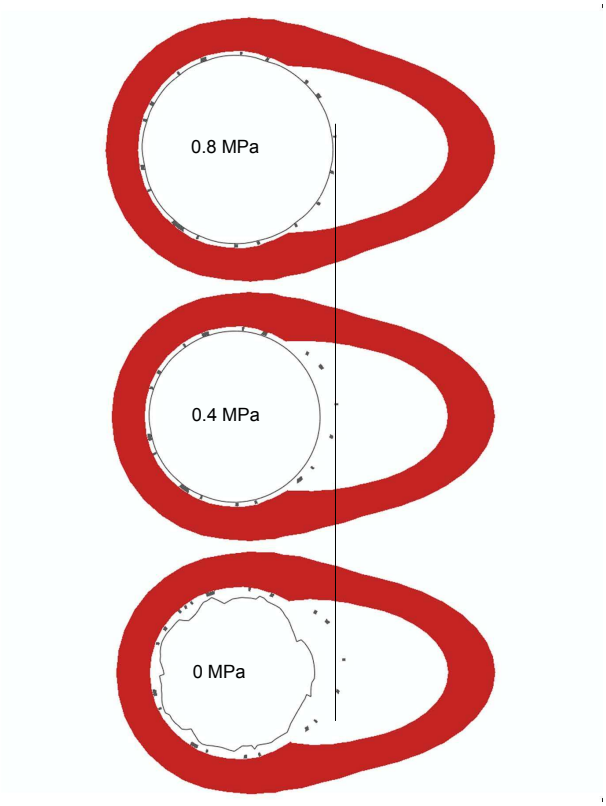

Figure 6.22: The stent struts are moving into the SB during deflation of the compliant balloon.

diameter after deflating the balloon. As already mentioned, this is related to the simplified material model used for the vessel wall.

6.7.2 Impact of stent misplacement

Inaccurate placement of the stent is suboptimal as the standard Liberté strut design may be located at the bifurcation ostium instead of the modified central stent structure which was specifically designed for this region. The modified region has a higher expansion range which is necessary to provide optimal support in the bifurcation region. Increasing the length of the modified stent region may limit the effect of inaccurate placement, but also increases the total metal volume as this stent section has a much denser strut pattern. Again, direct balloon-artery contact may occur outside the stented vessel section (see Fig. 6.24).

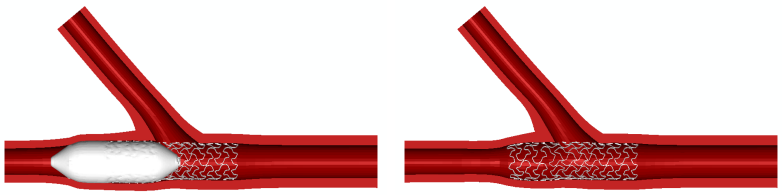

Figure 6.23: The compliant balloon should be positioned as precise as possible, because inaccuracies limit the strut protrusion and may damage the vessel wall outside the stented region.

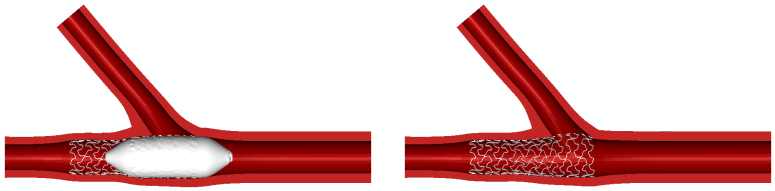

Figure 6.24: The modified stent pattern has no effect when it is placed outside the bifurcation region.

6.8 Limitations

The vessel wall is modelled as an homogeneous isotropic hyperelastic material which is clearly an important approximation of the complex mechanical behaviour of real blood vessels which demonstrate anisotropic, viscoelastic and inhomogeneous behaviour. Furthermore, residual stresses were not included and the bifurcation models were non-stenotic.

The finite element simulations were optimized to study the global stent deformation patterns and the accuracy of the predicted deformations was validated for several simulations. Detailed stress-strain analyses were not performed but may be necessary in case of very large strut deformations that might lead to strut fracture.

6.9 Conclusions

The finite element simulations provided interesting insights regarding the innovative bifurcation stent design and stenting procedure:

- Performing the postdilatation with the bulge balloon has important limitations (e.g. resulting floating struts) and was therefore not further

optimized and investigated.

- The parameters related to the compliant balloon used for postdilatation, such as balloon size, compliance and inflation pressure have a higher impact on the strut protrusion than modifications of the strut width in the central stent section.
- The procedure was repeated for a number of bifurcation models and this study showed the considerable impact of balloon and stent size in comparison with the MB diameter on the overdilatation of the parent vessel.
- The strut protrusion is further improved during the deflation of the compliant balloon.
- Accurate placement of both the stent and the compliant balloon are crucial factors for a successful procedure. Decreasing the length of the compliant balloon and/or increasing the length of the modified stent structure may limit the effects of small positioning inaccuracies.

Chapter 7

Stent design guidelines and final remarks

The work described in this thesis provides novel strategies to investigate the complex problem of bifurcation stenting. The application of these tools has led to a number of useful insights that are summarized in this chapter. Some suggestions for future research are also included as this work is certainly not an endpoint.

7.1 Conclusion

In chapter 2, a finite element model is described that allows to investigate the free expansion of balloon-expandable stents. The numerical results of this model correspond very well with both qualitative and quantitative experimental data, and therefore this model serves as a solid basis to study and optimize the mechanical behavior of this kind of stents. It has for example been observed that many balloon-expandable stents deploy in a non-uniform way, both in longitudinal and in circumferential direction. However, the preferred stent expansion would be perfectly uniform as this minimizes the endothelial damage and leads to a more uniform drug delivery in the case of drug eluting stents. Using the validated model, a parametric study has been conducted and the results show that both the balloon length and the folding pattern have an enormous impact on the uniformity of the expansion. A reduced balloon length leads to a more uniform deployment in longitudinal direction, whereas an increased number of balloon folds positively influences the uniformity in circumferential direction.

We investigated the most frequently applied bifurcation stenting technique in chapter 3 (i.e. provisional stenting). This technique involves the implan-

tation of a stent in the MB, followed by subsequent inflation of a balloon (which is positioned in both the MB and the SB) through the side of the stent. This postdilation through the side of the stent is performed with the aim of improving the SB patency by pushing the obstructing struts against the vessel wall. Bench testing results have shown that such inflation indeed has a positive effect on the SB access, but may lead to floating struts in the MB lumen. Very similar results were obtained using finite element analysis. This clearly demonstrates the feasibility of using computer simulation to investigate bifurcation stenting techniques. Furthermore, it was also observed that different stent designs may lead to very different strut deformation patterns, showing the importance of thorough design efforts by stent manufacturers and of appropriate stent selection in clinical practice.

The study described in chapter 4 investigates and compares three different second generation drug-eluting stents when being implanted in the curved MB of a coronary bifurcation. The three-dimensional bifurcation model is based on patient-specific angiographic data that accurately reproduce the in vivo curvatures of the vessel segments. The layered structure of the arterial wall and the anisotropic mechanical behavior of each arterial layer are taken into account by using an existing advanced constitutive model. This constitutive model was implemented as a user-defined material for Abaqus and the accuracy of the implementation is verified by comparing the virtual mechanical behavior with experimental and analytical data. The use of anisotropic materials requires a proper definition of the local material orientations and therefore, a novel algorithm has been developed to automatically define the fiber orientations. In addition, an innovative simulation strategy considering the insertion of a folded balloon catheter over a guide wire has been developed in order to position the stents within the curved vessel. The results show that all stents lead to more or less the same amount of vessel straightening after implantation, but the resulting distributions of the wall stresses are strongly dependent on the stent design. Using a parametric modeling approach, two design modifications, which reduce the predicted maximum values of the wall stress, are proposed and analyzed. This illustrates the added value of using computer simulations during the design phase as many design variants can be analyzed without having to manufacture every design iteration.

In chapter 5, we quantitatively analyzed the geometry of different existing stents. Such objective comparisons allow interventional cardiologists to select appropriate devices for a particular stenotic lesion. The maximum size of the openings (i.e. cell size) is an important design parameter when stenting bifurcation lesions because these openings are often enlarged by a balloon inflation through the side of the stent. An innovative technique, based on micro-CT images and using the pyFormex software, was developed to accurately measure the cell size. A considerable variation of the cell size of the different investigated stents was observed. By combining the cell size

data with anatomical information (MB diameter, SB diameter and bifurcation angle) we proposed a technique that may help to select the appropriate stent for a particular lesion. Implanting a stent with a cell circumference which is smaller then the ostium circumference will almost inevitably result in a suboptimal deployment and obstructing struts.

In chapter 6, computer simulations are being used to investigate the feasibility of a new dedicated bifurcation stent and a modified procedure for provisional stenting. The stent is intended for the MB and has a modified strut pattern in the central stent region, which allows the stent to reach a larger diameter at the location of the bifurcation. This is important to provide partial scaffolding at the SB ostium. The modified procedure consists of a postdilation with a dedicated balloon within the already expanded MB stent (for example, a bulge or a compliant balloon). The two motivations for such postdilation are: (i) to open the stent cells obstructing the SB access in order to facilitate the insertion of a balloon catheter into the SB and (ii) to cause strut protrusion into the SB to provide partial ostial scaffolding. We were able to develop accurate models of the different balloon models and of the free stent expansion. These validated models were then used to simulate the complete bifurcation stenting procedure. The results of an in-vitro experiment also demonstrated the accuracy of the predicted deformation patterns after the postdilation. Based on the finite element model, the impact of a number of device and procedural parameters (such as balloon pressure, balloon compliance, balloon size, stent design, bifurcation geometry) on the final strut deformation have been examined. These results provided new insights and allow to further optimize the stent design and the proposed procedure.

In conclusion, the main achievements of the work described in this thesis are (i) the development of new simulation strategies allowing to study complex bifurcation stenting techniques, (ii) the new insights into the shortcomings of currently applied techniques, (iii) the objective comparison of existing stents, (iv) the application of subject-specific modelling (morphological and constitutive) in the field of coronary bifurcation stenting, and (v) the use of simulations to optimize a new dedicated bifurcation stent and a modified stenting procedure.

7.2 Future work

The findings and methods of this thesis can be used as a starting point for further research topics. Without the aim of being complete, some suggestions are made in this section.

Patient-specific (or location-specific) modelling provides the possibility to assess the impact of stent implantations in realistic environments. However,

the widespread use of this patient-based approach for bifurcation stenting is limited by the required significant amount of pre-processing. For example, the use of high quality hexahedral meshes is crucial for many reasons but the generation of such meshes is currently time-consuming. Therefore, automation of this process (including the subdivision of the grid in the different arterial layers) is a very important step if we want to study multiple bifurcations, which would considerably increase the value of these patient-specific simulations. Including multiple bifurcations is necessary if one wants to make more (scientific) general conclusions using common statistical methods. Similarly, each morphology should be combined with multiple sets of material data as these data show a considerable variation.

With respect to constitutive modelling, an infinite list of suggestions can be made to further improve the models used in this work. Therefore, we just list a few items:

- To date, residuals stresses have not yet been included in (patient-specific) bifurcation models.
- Some work has been done on the numerical modelling of dissection and rupture of the arterial tissue, phenoma which are frequently observed in clinical practice. However, further efforts are required in order to include such models in large-scale applications.
- Stent implantation and balloon angioplasty leads to permanent deformations of the vessel wall. Attempts have been made to include these permanent deformations, but again, more experimental research needs to be done to improve the quality of the proposed models.
- The remodelling of the vessel wall after stent implantation is a time-dependent process. Including this temporal component in the simulations would be very interesting.

There is also a need for a better integration of in-vitro experiments during the virtual design process. In addition, these in-vitro experiments should be further improved. For example, both the morphology and material of the silicon arteries are currently not realistic.

Numerous bifurcation stenting techniques have been proposed in literature, but only the provisional approach has been studied in this thesis. Applying the developed models to address other stenting techniques would be very interesting. Lastly, only conventional stents (intended for unbranched vessels) have been compared with each other. Providing objective comparisons of the different dedicated bifurcation stent systems is of course a next step.

List of Figures

1.1 Schematic overview of the main coronary arteries (RCA = right coronary artery, LCA = left coronary artery, LM = left main artery, LCX = left circumflex artery, LAD = left anterior descending artery). 2

1.2 Schematic representation of a coronary bifurcation with inflow in the proximal main branch (PMB) and outflow at the distal main branch (DMB) and the side branch (SB). α indicates the bifurcation angle. The SB ostium and the carina are represented by a dotted line and a small circle respectively. . 3

1.3 Comparison of the relation between bifurcation vessel diameters proposed by Murray [10] and Finet et al. [11] when assuming equal distal branch diameters. 4

1.4 Layered structure of young and healthy arteries [15]. 5

1.5 Schematic illustration of the blood flow in a bifurcation. . . 6

1.6 Medina classification for coronary bifurcation lesions. 6

1.7 Unconstrained expansion of the Endeavor stent (Medtronic): Panel A shows the stent, crimped around a folded angioplasty balloon. The deployment starts at the stent ends (panel B) and continues towards the stent center (panel C). 9

1.8 Schematic illustration of a balloon-expandable stent placement. After correct positioning of the crimped stent (panel A), the balloon is inflated at high pressure leading to the expansion of the device and to an improved luminal area (panel B). Finally, the procedure is completed by deflating and extracting the balloon catheter. The stent remains in place to keep the vessel open (panel C). 10

1.9 Schematic illustration of stent recoil and foreshortening (L_o and D_o denote the length and diameter of the crimped stent, L_f and D_f denote the length and diameter of the final stent shape after balloon deflation and D_i refers to the intermediate stent diameter at the maximal balloon pressure). 12

1.10 Examples of balloon-expandable stents. A: Endeavor (Medtronic), B: Taxus Liberté (Boston Scientific), C: Promus (Boston Scientific), D: PRO-Kinetic (Biotronik). The images do not have the same scale. 13

1.11 Examples of self-expandable stents. A: Wallstent (Boston Scientific), B: RX Acculink (Abbott Vascular), C: Xact (Abbott Vascular), D: SelfX (Abbott Vascular). The images do not have the same scale. 13

1.12 MADS classification of the different bifurcation stenting techniques (adapted from [18]). Clarification of the abbreviations: MB = main branch, PMB = proximal main branch, DMB = distal main branch, SB = side branch, prox = proximal, TAP = T-stenting and small protrusion technique, SKS = simultaneous kissing stents. 15

1.13 MADS classification of the inverted techniques (adapted from [18]). Clarification of the abbreviations: MB = main branch, PMB = proximal main branch, DMB = distal main branch, SB = side branch, prox = proximal, TAP = T-stenting and small protrusion technique, SKS = simultaneous kissing stents, inv = inverted. 16

1.14 Schematic overview of the insertion and deployment procedure of the Antares stent system (Trireme Medical). The top panel shows the device when the stabilizing SB wire is still within the dedicated lumen. Following to correct positioning, the stabilizing wire is advanced into the SB (middle panel) and the stent is finally deployed by inflating a single balloon (bottom panel). Adapted from [66]. 23

1.15 The design of the self-expandable Axxess stent (Devax) aims at providing adequate coverage in the bifurcation region. Placement is facilitated by the four radiopaque markers (three distal and one proximal). Adapted from [70]. 24

1.16 The Multi-Link Frontier stent (Abbott Vascular) is deployed by the simultaneous inflation of two balloons [73]. 25

1.17 Schematic illustration of the deployment of the Nile Croco bifurcation stent (Minvasys). Courtesy Minvasys. 26

1.18 The Petal stent (Boston Scientific) has a side aperture with struts (the so-called petal elements) that deploy into the SB by inflation of the particular secondary balloon. Adapted from [66]. 27

1.19 Illustration of the Sideguard ostium protection device (Cappella). Adapted from [76]. 28

1.20 Comparison of two SideKick stent systems (Y-Med) with a different location of the exit port (left panel: central location, right panel: proximal location). Adapted from [79]. 29

1.21 Schematic illustration of the implantation of the self-expandable Stentys device (Stentys) in the MB (top left), followed by the insertion and inflation of an angioplasty balloon through the cell closest to the carina (top right and bottom left). This dilation disconnects the struts (the drawings do not show the bridge elements) and results in improved SB access and ostium scaffolding. The bottom right panel shows the final stent shape. Courtesy Stentys. 30

1.22 Schematic illustration of the Tryton device (Tryton Medical). The implantation of the Tryton stent using a stepped balloon is depicted in the left panel, which also indicates the three stent zones. The right panel shows the placement of a conventional MB stent through the struts of the Tryton stent. Courtesy Tryton Medical. 31

1.23 Twin Rail bifurcation stent system (Invatec). Adapted from [66]. 32

1.24 Micro-CT visualization of a Promus stent (Boston Scientific) after kissing balloon postdilatation. The left panel shows a top view on both branches of the bifurcation, while the right panel gives a view into the SB. The floating struts at the SB ostium are clearly visible after removal of the struts at the opposite MB wall. 35

2.1 Numerical inflation of a cylindrical balloon (only half of the balloon was simulated because of symmetry). 45

2.2 Meshed section of the balloon-catheter-stent model. 46

2.3 Comparison of a trifolded (left) and a sixfolded (right) balloon. Both folding patterns are based on the same initial balloon diameter, namely, $D_o = 2.85\,\mathrm{mm}$. 48

2.4 Expansion of the reference model (trifolded balloon with a length of 10.5 mm): before inflation (top); transient phase (middle) corresponding to a pressure between 0.3 MPa and 0.4 MPa (during the transient expansion phase, the balloon unfolds and the stent diameter rapidly increases); situation after this transient expansion (pressure higher than 0.4 MPa, bottom). 49

2.5 Quantitative validation of the reference model: the maximum percent difference in diameter between the numerical results and the compliance chart provided by the manufacturer is 4.1% and occurs at a pressure of 1.4 MPa. The steep part (pressure between 0.3 MPa and 0.4 MPa) of the curve obtained by simulation corresponds to the transient central shape from Fig. 2.4. 49

2.6 Qualitative validation of the Cypher stent expansion: the left side shows the virtually predicted deformations while the right part of the image displays the micro-CT visualization of the stent deployment. 50

2.7 Transient expansion shape for Model J (top), Model E (center), and the reference model (bottom). A shorter balloon length results in a decreased dogbone effect. 51

2.8 Relationship between the balloon length and the maximal dogboning coefficient during the transient expansion phase. A more uniform expansion is obtained by decreasing the balloon length. 51

2.9 Cross section at the end of the transient expansion phase, showing that a trifolded balloon causes a nonuniform strut distribution (left panel: simulation; center panel: experiment), whereas a sixfolded balloon (right panel: simulation) results in a homogeneous strut placement. 52

2.10 Transient expansion shape for Models L and M. A noncentrally placed stent results for both folding patterns in a strongly asymmetric expansion. 53

2.11 Two different strategies can be used to obtain a finite element mesh starting from a stent sample. The left pathway illustrates the previously used methodology, which involves several manual steps. The different steps of the alternative (semi-automated) strategy presented here are shown in the right pathway. 56

2.12 The top panel shows a photograph of the stent. The surface mesh obtained after segmentation of the CT-images is shown in the middle panel. The resulting finite element beam mesh obtained by centerline determination is depicted in the bottom panel. 58

2.13 Comparison of the simulation results using two different methods to create the stent geometry. The simulation based on the traditional approach is depicted in the left panel, whereas the beam mesh in the right panel is based on the new approach involving the centerline computation. 59

2.14 A and B: The same stent geometry using a different segmentation threshold. The resulting centerline in both cases is almost identical and therefore, the applied threshold has a limited impact on the resulting centerline. However, the centerline can be modified by the segmentation threshold in case that the reconstructed stent geometry contains connections between different struts which are not connected in reality (C). 60

2.15 A second micro-CT scan was performed using a higher resolution (CT voxel size of 1.05 µm) in order to obtain a more accurate estimate for the strut cross-section (see right panel). Only a small portion of the stent was scanned at this resolution. 60

3.1 Concept of SB balloon dilatation through the MB stent. . . . 64

3.2 3D model of Cypher (left) and MULTI-LINK Vision (right) stent. 65

3.3 Geometrical models representing trifolded Raptor balloon catheters with a nominal diameter of 2.5 mm (left panel) and 3 mm (right panel). 66

3.4 Illustration of the simulation procedure for the Cypher stent (panel A: initial configuration, panel B: fully expanded stent, panel C: stent configuration after recoil, panel D: initial position of the 2.5 mm SB balloon, panel E: deformed configuration at the maximum pressure of 1.5 MPa, panel F: final state after balloon deflation). 68

3.5 Schematic drawing illustrating the projection method used to calculate the Projected Cell Area (PCA). 69

3.6 Comparison of the manufacturer data (crosses) with the simulation results (line). 70

3.7 Stent distortion after expansion in the MB and following subsequent balloon dilatation through a stent side-hole. The stent opening in front of the SB considerably enlarges due to this balloon inflation and the effect depends on the balloon size. 71

3.8 Projected stent cells prior to and after SB balloon dilatation. These 2D curves were used to determine the PCA. 73

3.9 View into the MB (from proximal side) showing the impact of the SB balloon dilatation on the MB lumen. The results strongly depend on the stent design, in contrast to the balloon size, which seems to have a minor effect. The horizontal line indicates the cut views depicted in Fig. 3.11. 74

3.10 Comparison of the distortion of the MultiLink stent observed in bench tests [87] (top panel) with the numerically predicted deformation of the MULTI-LINK Vision stent (bottom panel). 74

3.11 Cut view showing the stent strut positions. The circles indicate floating struts in the MB lumen. 75

4.1 Three-dimensional model of the lumen of the left coronary artery bifurcation obtained by rotational angiography. The luminal geometry consists of circular cross-sections. Sections A-D of the lumen were considered non-diseased, and at those locations, the circles were scaled by a factor of 1.6 according to the data published by Holzapfel et al. [12]. Two scaled circles (at sections A and B for the main branch, and at sections C and D for the SB) served as a starting point to generate the outer wall of that branch. All other luminal circles were scaled to a diameter based on a linear interpolation (or extrapolation) of the diameters at sections A and B in case of the main branch or sections C and D for the SB. 80

4.2 Outermost layer of the structured hexahedral discretization at the location of the bifurcation with an enlarged view of the indicated element. Local material orientations ($\mathbf{n}_1'$, $\mathbf{n}_2$, $\mathbf{n}_3$) are computed for every finite element based on its edges. 82

4.3 Illustration of the (local) mean fiber directions $\mathbf{M}$ and $\mathbf{M}'$ for the finite elements. The directions are depicted for a small portion of the superficial elements, located close to the bifurcation, as shown in Fig. 4.2. 83

4.4 Comparison between a part of the micro-CT-based Endeavor stent geometry (left) and the discretized model (right). A weld is also indicated in the left figure. 84

4.5 Longitudinal cross-sectional view of the unfolded balloon catheter (at 0 bar) with the related dimensions (Raptor balloon from Cordis, Johnson & Johnson; at nominal pressure the nominal diameter is 3.5 mm). 85

4.6 Illustration of the simulated stent insertion and deployment procedure: panel A – initial configuration; panel B – intermediate position during insertion; panel C – final position prior to expansion; panel D – partially inflated stent at a balloon pressure of 3 bar; panel E – configuration at the maximum pressure of 12 bar; panel F – final state after balloon deflation. 87

4.7 Unrolled model showing one end of the modified Cypher Select stent $\mathtt{CS}_{\mathrm{end}}$: The strut width w_1 of the proximal and distal ring segments is 90 µm, whereas all central ring segments have a strut width w_2 of 130 µm. For the original Cypher Select stent model, w_1 and w_2 are equal to 130 µm. . 88

4.8 Comparison of simulated uniaxial extensions of arterial strips in the axial and circumferential directions shows very good agreement with experimental data documented in [12]. 90

4.9 Comparison of simulated biaxial deformation of the media in terms of Cauchy stress/stretch and corresponding analytical results shows good agreement. 91

4.10 Comparison of the pre- and post-stenting luminal curvatures. Stent implantation results in vessel straightening here shown for the Cypher Select stent. 91

4.11 Comparison of the circumferential (Cauchy) stress distribution after implantation of the Cypher Select, the Endeavor and the Taxus Liberté stents, with maximal stresses of 0.38, 0.15 and 0.15 MPa from left to right. 92

4.12 Comparison of the circumferential (Cauchy) stress distributions caused by the implantation of the two modified (Cypher Select) stent designs, $\mathtt{CS}_{\mathrm{thin}}$ and $\mathtt{CS}_{\mathrm{end}}$, while the left image of Fig. 4.11 shows the analogue for the original Cypher Select stent: a reduction of the overall strut thickness ($\mathtt{CS}_{\mathrm{thin}}$) or of the strut width of the distal and proximal ring segments ($\mathtt{CS}_{\mathrm{end}}$) leads to a bisection of the maximal stresses around one stent end. 93

5.1 Stent cell requirements for different stenting strategies (the zone of interest is indicated with a dotted line). When performing provisional bifurcation stenting, the stent cells should be at least as large as the SB ostium (panel A). The same condition is valid for both the side and MB stent during crush stenting (panel B). The situation as shown in panel C is encountered during culotte stenting and in this case, the cells should be at least as large as the cross-section of the MB.. 99

5.2 The size of the ostium depends on the bifurcation angle and the SB and MB diameters. The ostium is described by a three-dimensional curve from which the circumference can be calculated. 101

5.3 Demonstration of the complete procedure to obtain a single cell of the Cypher stent. The cell circumference can then easily be calculated as the sum of the length of all planar line segments of this cell. 102

5.4 Comparison of microscopic images with the resulting planar representations of the cells. The microscopic images do not have the same scale. From top to bottom: Endeavor, PRO-Kinetic, Promus and Taxus Liberté. 103

5.5 The ostium circumference of a 3 mm parent vessel is shown as a function of the SB diameter and the bifurcation angle. . 104

5.6 The grey zones indicate the cases in which the ostium circumference is larger than the cell circumference when the stents are deployed in a 3 mm MB (for three different SB sizes). Therefore, it is highly likely that in these cases (i.e. cases within grey zone) the cells will not be sufficiently enlarged by balloon dilatation through the side. The Endeavor stent is not shown because the cells can be sufficiently enlarged in all cases. 105

5.7 Panel A shows the worst-case situation which was used in this work (no partial stent deployment in the SB). This situation requires larger cells (at least as large as ostium) than in case of partial stent deployment in the SB (panel B). 107

5.8 View into the SB after virtual implantation of three different DES in the MB. The number of struts at the SB ostium, which is indicated with a dotted line, is totally different for the three stent designs. Intuitively, it seems easier to advance a guide wire and a balloon catheter into the SB after implantation of the Cypher Select stent. 108

5.9 Illustration of the cylindrical, displacement driven expansion procedure for the Coroflex stent. The crimped stent is shown in the left panel, while the right panel depicts the deformed stent when the cylindrical tube has a diameter of 3 mm. . . . 109

5.10 Illustration of the procedure to determine the maximum inscribed circle for the Cypher stent. The black line represents an unrolled stent cell at a stent diameter of 3 mm. The generated regular grid of points is divided into the points within (green) and outside (red) the cell. From all inner points, the point lying at the maximum distance from the cell is selected. This point is the center of the maximum inscribed circle. The grid used to generate this figure is clearly not fine enough, since the circle only touches the cell at one location. 110

5.11 Comparison of the deformed cells of the five investigated stents at an inner stent diameter of 3 mm. The maximum inscribed circle and the corresponding diameter are drawn in red. 111

5.12 Comparison of the deformed cell of the Taxus Liberté stent at different stent diameters. The corresponding stent diameter is indicated below every cell. 112

5.13 Quantitative comparison of the impact of the stent diameter on the strut density which is here reflected by the diameter of the maximum inscribed circle. 113

6.1 Unrolled bifurcation stent geometry which is based on the Liberté design with an altered central strut pattern. One ring element in the central zone is indicated with a red line. The length of this red line or ring element is larger then the length of similar ring elements in the distal or proximal zone. Therefore, the central part can be expanded to a larger diameter which is necessary at the location of the bifurcation in order to provide at least partial support to the SB. 117

6.2 Non-inflated unfolded balloon geometries (left panel: standard non-compliant 72D PEBAX balloon, middle panel: compliant 63D PEBAX balloon, right panel: non-compliant bulge balloon). The scale of the different balloons is not exactly the same. 119

6.3 Reference bifurcation model. 119

6.4 Schematic overview of the different simulation steps. 122

6.5 The three depicted stent designs have a different strut width in the central stent region, but the distal and proximal ends are identical. The upper panel shows the design where the strut width has been reduced to 60 percent of the original width, whereas the middle panel shows the design with a reduction to 80 percent of the original width. The bottom panel depicts the original design as shown in Fig. 6.1 without reduced strut width. 124

6.6 Overview of the different bifurcation models (the abbreviations are explained in Table 6.3). 125

6.7 Schematic illustration of the maximal strut protrusion (MSP). The MSP is the maximal distance from the axis of the main vessel to a stent strut at the SB ostium minus the radius of the proximal main vessel. 126

6.8 Schematic illustration of the overdilatation coefficient (OC). The vertical line within the distal MB indicates the cross section used for the calculation of the overdilatation coefficient (OC). 126

6.9 Comparison of the experimental data with the numerical results for the non-compliant 72D PEBAX balloon. 127

6.10 Comparison of the experimental data (filled diamonds) with the numerical results (solid line corresponds with a Young's modulus of 465 MPa, the dashed line corresponds with a Young's modulus of 700 MPa). The balloon unfolding and stretching is shown on the right for the simulation with the Young's modulus of 700 MPa. 128

6.11 Comparison of the experimental data with the numerical results. The diameter refers to the maximum diameter of the bulge balloon. 128

6.12 Comparison of the experimental data with the numerical results. 129

6.13 Comparison of the experiment (left panel) with the numerical results (right panel). Due to a different initial position of the expanded stent in the experiment and in the simulation, it is difficult to identify the corresponding stent struts. 130

6.14 Comparison of the effect of postdilating the stent with a non-compliant bulge balloon (left side) or with a compliant balloon (right side). The upper panels show the stent deformation and the inflated balloons at 1.1 MPa. The final configuration after balloon deflation is depicted in the bottom panels. The circles indicate the floating stent struts (i.e. struts not in contact with the vessel wall). 131

6.15 Impact of strut width reductions in the central stent section (left panel: reduction to 60 percent of the original width, middle panel: reduction to 80 percent of the original width, right panel: original design). 132

6.16 Impact of the inflation pressure (left panel: reference simulation with inflation at 0.8 MPa, middle panel: inflation at 1.1 MPa, right panel: inflation at 1.4 MPa). 132

6.17 Impact of the balloon size (left panel: initial balloon diameter of 4 mm, middle panel: reference simulation with initial balloon diameter of 4.24 mm, right panel: initial balloon diameter of 4.5 mm). 132

6.18 Impact of the balloon compliance (top left panel: elastic modulus of 400 MPa, top right panel: elastic modulus of 500 MPa, bottom left panel: elastic modulus of 600 MPa, bottom right panel: reference simulation with an elastic modulus of 700 MPa). 133

6.19 Impact of the bifurcation geometry (top left panel: S50, bottom left panel: S80, top middle panel: reference simulation with M50, bottom middle panel: M80, top right panel: L50, bottom right panel: L80). 134

6.20 Maximal Strut Protusion (MSP) for all the simulations (D_o = original balloon diameter at zero pressure, E = Young's modulus) 134

6.21 Overdilatation coefficient (OC) for all the simulations (D_o = original balloon diameter at zero pressure, E = Young's modulus) 135

6.22 The stent struts are moving into the SB during deflation of the compliant balloon. 136

6.23 The compliant balloon should be positioned as precise as possible, because inaccuracies limit the strut protrusion and may damage the vessel wall outside the stented region. 137

6.24 The modified stent pattern has no effect when it is placed outside the bifurcation region. 137

List of Tables

2.1 Overview of the different models and their characteristics. Axial stent position refers to the position of the stent on the balloon catheter. 47

2.2 Influence of small positioning inaccuracies on the uniformity of the expansion. 54

3.1 Material properties for SS316L and L605 Co-Cr alloy. 66

3.2 Projected Cell Area (PCA) for the two investigated stents prior to and after SB balloon dilatation. Both the 2.5 and 3 mm balloon considerably increase the cell covering the SB, and this cell enlargement is maximal for the 3 mm balloon. . 72

4.1 Material parameters for the constitutive model (4.1)–(4.3) determined by Holzapfel et al. [12]. The data correspond to Specimen I documented in [12]. 81

4.2 Overview of the analyzed stents and their main characteristics. 84

4.3 Stent material properties for the Cypher Select and the Taxus Liberté, made from stainless steel (SS316L), and for the Endeavor, made from a stronger cobalt-chromium alloy (F562), see [135]. 85

4.4 Radial strength, defined to be the external pressure causing a sudden collapse of the stent structure, numerically determined for all stent designs, i.e. the original ones and the modified stents $\mathtt{CS}_{\text{thin}}$ and $\mathtt{CS}_{\text{end}}$. 94

5.1 Overview of the cell circumferences and the corresponding equivalent diameters. These are the maximum diameters of the strut openings that can be obtained upon inflation of a balloon through those openings. 101

6.1 The material properties of each balloon were calculated based on the provided pressure/diameter data. This calculation results in stress/strain data, which are approximated by a Young's modulus. However, the compliant balloon demonstrates a considerable non-linear behaviour, and therefore, the constitutive behaviour is approximated by a first Young's modulus in the low pressure range (i.e. 465 MPa) and a second Young's modulus in the high pressure range (i.e. 700 MPa). 120

6.2 Non-zero coefficients of the third order polynomial strain energy function used to describe the mechanical behaviour of the arterial wall (according to the ABAQUS conventions). . 121

6.3 Overview of the investigated bifurcation models (D_{PMB} = proximal MB diameter, D_{DMB} = distal MB diameter, D_{SB} = SB diameter). The model abbreviation is related to the model size (Small, Medium and Large) in combination with the bifurcation angle (50 or 80). The reference bifurcation model is indicated in bold (i.e. M50). 125

Bibliography

[1] S. Allender, P. Scarborough, V. Peto, M. Rayner, J. Leal, R. Luengo-Fernandez, and A. Gray. European cardiovascular disease statistics. 2008.

[2] S. Cook, A. Walker, O. Hügli, M. Togni, and B. Meier. Percutaneous coronary interventions in Europe: prevalence, numerical estimates, and projections based on data up to 2004. *Clin Res Cardiol*, 96:375–382, 2007.

[3] R. Ross. Atherosclerosis–an inflammatory disease. *N. Engl. J. Med.*, 340:115–126, 1999.

[4] A. Colombo, E. Bramucci, S. Saccà, R. Violini, C. Lettieri, R. Zanini, I. Sheiban, L. Paloscia, E. Grube, J. Schofer, L. Bolognese, M. Orlandi, G. Niccoli, A. Latib, and F. Airoldi. Randomized study of the crush technique versus provisional side-branch stenting in true coronary bifurcations: the CACTUS (Coronary Bifurcations: Application of the Crushing Technique Using Sirolimus-Eluting Stents) Study. *Circulation*, 119:71–78, 2009.

[5] I. Iakovou, L. Ge, and A. Colombo. Contemporary stent treatment of coronary bifurcations. *J. Am. Coll. Cardiol.*, 46:1446–1455, 2005.

[6] J. Ormiston, M. Webster, B. Webber, J. Stewart, P. Ruygrok, and R. Hatrick. The 'crush' technique for coronary artery bifurcation stenting: insights from micro-computed tomographic imaging of bench deployments. *JACC: Cardiovascular Intervention*, 1:351–357, 2008.

[7] J. T. Dodge, B. G. Brown, E. L. Bolson, and H. T. Dodge. Lumen diameter of normal human coronary arteries. Influence of age, sex, anatomic variation, and left ventricular hypertrophy or dilation. *Circulation*, 86:232–246, 1992.

[8] V. Dzavik, R. Kharbanda, J. Ivanov, D. J. Ing, S. Bui, K. Mackie, R. Ramsamujh, A. Barolet, L. Schwartz, and P. H. Seidelin. Predictors of long-term outcome after crush stenting of coronary bifurcation

lesions: importance of the bifurcation angle. *Am. Heart J.*, 152:762–769, 2006.

[9] S. Kaplan, P. Barlis, K. Dimopoulos, A. La Manna, O. Goktekin, A. Galassi, J. Tanigawa, and C. Di Mario. Culotte versus T-stenting in bifurcation lesions: immediate clinical and angiographic results and midterm clinical follow-up. *Am. Heart J.*, 154:336–343, 2007.

[10] C. D. Murray. The Physiological Principle of Minimum Work: I. The Vascular System and the Cost of Blood Volume. *Proc. Natl. Acad. Sci. U.S.A.*, 12:207–214, 1926.

[11] G. Finet, M. Gilard, B. Perrenot, G. Rioufol, P. Motreff, M. Gavit, and R. Prost. Fractal geometry of arterial coronary bifurcations: a quantitative coronary angiography and intravascular ultrasound analysis. *EuroInt.*, 3:490–498, 2007.

[12] G. A. Holzapfel, G. Sommer, C. T. Gasser, and P. Regitnig. Determination of layer-specific mechanical properties of human coronary arteries with nonatherosclerotic intimal thickening and related constitutive modeling. *Am. J. Physiol. Heart Circ. Physiol.*, 289:H2048–2058, 2005.

[13] H. C. Stary, D. H. Blankenhorn, A. B. Chandler, S. Glagov, W. Insull, M. Richardson, M. E. Rosenfeld, S. A. Schaffer, C. J. Schwartz, and W. D. Wagner. A definition of the intima of human arteries and of its atherosclerosis-prone regions. A report from the Committee on Vascular Lesions of the Council on Arteriosclerosis, American Heart Association. *Circulation*, 85:391–405, 1992.

[14] G. A. Holzapfel. Collagen in arterial walls: biomechanical aspects. In P. Fratzl, editor, *Collagen. Structure and mechanics*, pages 285–324. Springer-Verlag, 2008.

[15] Wikipedia: artery. `http://en.wikipedia.org/wiki/Artery` (accessed 23 November 2009).

[16] A. M. Malek, S. L. Alper, and S. Izumo. Hemodynamic shear stress and its role in atherosclerosis. *JAMA*, 282:2035–2042, 1999.

[17] A. Medina, J. Suréez de Lezo, and M. Pan. A new classification of coronary bifurcation lesions. *Rev Esp Cardiol*, 59:183, 2006.

[18] V. Legrand, M. Thomas, M. Zelisko, B. De Bruyne, N. Reifart, T. Steigen, D. Hildick-Smith, R. Albiero, O. Darremont, G. Stankovic, M. Pan, J. Flensted Lassen, Y. Louvard, and T. Lefèvre. Percutaneous coronary intervention of bifurcation lesions: state-of-the-art. Insights from the second meeting of the European Bifurcation Club. *EuroInt.*, 3:44–49, 2007.

[19] J. J. Fischer, H. Samady, J. A. McPherson, I. J. Sarembock, E. R. Powers, L. W. Gimple, and M. Ragosta. Comparison between visual assessment and quantitative angiography versus fractional flow reserve for native coronary narrowings of moderate severity. *Am. J. Cardiol.*, 90:210–215, 2002.

[20] N. H. Pijls, J. A. van Son, R. L. Kirkeeide, B. De Bruyne, and K. L. Gould. Experimental basis of determining maximum coronary, myocardial, and collateral blood flow by pressure measurements for assessing functional stenosis severity before and after percutaneous transluminal coronary angioplasty. *Circulation*, 87:1354–1367, 1993.

[21] N. H. Pijls, B. De Bruyne, K. Peels, P. H. Van Der Voort, H. J. Bonnier, J. J. Bartunek J Koolen, and J. J. Koolen. Measurement of fractional flow reserve to assess the functional severity of coronary-artery stenoses. *N. Engl. J. Med.*, 334:1703–1708, 1996.

[22] R. H. Goetz, M. Rohman, J. D. Haller, R. Dee, and S. S. Rosenak. Internal mammary-coronary artery anastomosis. A nonsuture method employing tantalum rings. *J. Thorac. Cardiovasc. Surg.*, 41:378–386, 1961.

[23] J. C. Palmaz, R. R. Sibbitt, S. R. Reuter, F. O. Tio, and W. J. Rice. Expandable intraluminal graft: a preliminary study. Work in progress. *Radiology*, 156:73–77, 1985.

[24] R. A. Schatz, J. C. Palmaz, F. O. Tio, F. Garcia, O. Garcia, and S. R. Reuter. Balloon-expandable intracoronary stents in the adult dog. *Circulation*, 76:450–457, 1987.

[25] P. W. Serruys, P. de Jaegere, F. Kiemeneij, C. Macaya, W. Rutsch, G. Heyndrickx, H. Emanuelsson, J. Marco, V. Legrand, and P. Materne. A comparison of balloon-expandable-stent implantation with balloon angioplasty in patients with coronary artery disease. Benestent Study Group. *N. Engl. J. Med.*, 331:489–495, 1994.

[26] D. L. Fischman, M. B. Leon, D. S. Baim, R. A. Schatz, M. P. Savage, I. Penn, K. Detre, L. Veltri, D. Ricci, and M. Nobuyoshi. A randomized comparison of coronary-stent placement and balloon angioplasty in the treatment of coronary artery disease. Stent Restenosis Study Investigators. *N. Engl. J. Med.*, 331:496–501, 1994.

[27] C. Kaiser, H. P. Brunner-La Rocca, P. T. Buser, P. O. Bonetti, S. Osswald, A. Linka, A. Bernheim, A. Zutter, M. Zellweger, L. Grize, and M. E. Pfisterer. Incremental cost-effectiveness of drug-eluting stents compared with a third-generation bare-metal stent in a real-world setting: randomised Basel Stent Kosten Effektivitats Trial (BASKET). *Lancet*, 366(9489):921–929, 2005.

[28] L. Mauri, T. S. Silbaugh, R. E. Wolf, K. Zelevinsky, A. Lovett, Z. Zhou, F. S. Resnic, and S. L. Normand. Long-term clinical outcomes after drug-eluting and bare-metal stenting in Massachusetts. *Circulation*, 118:1817–1827, 2008.

[29] B. Scheller, C. Hehrlein, W. Bocksch, W. Rutsch, D. Haghi, U. Dietz, M. Böhm, and U. Speck. Treatment of coronary in-stent restenosis with a paclitaxel-coated balloon catheter. *N. Engl. J. Med.*, 355:2113–2124, 2006.

[30] C. W. Hwang, D. Wu, and E. R. Edelman. Physiological transport forces govern drug distribution for stent-based delivery. *Circulation*, 104:600–605, 2001.

[31] R. Erbel, C. Di Mario, J. Bartunek, J. Bonnier, B. de Bruyne, F. R. Eberli, P. Erne, M. Haude, B. Heublein, M. Horrigan, C. Ilsley, D. Böse, J. Koolen, T. F. Lüscher, N. Weissman, and R. Waksman. Temporary scaffolding of coronary arteries with bioabsorbable magnesium stents: a prospective, non-randomised multicentre trial. *Lancet*, 369:1869–1875, 2007.

[32] F. Vogt, A. Stein, G. Rettemeier, N. Krott, R. Hoffmann, J. vom Dahl, A. K. Bosserhoff, W. Michaeli, P. Hanrath, C. Weber, and R. Blindt. Long-term assessment of a novel biodegradable paclitaxel-eluting coronary polylactide stent. *Eur. Heart J.*, 25:1330–1340, 2004.

[33] J.C. Squire. *Dynamics of Endovascular Stent Expansion.* PhD thesis, Massachusetts Institute of Technology, US, 2000.

[34] C. Rogers and E. R. Edelman. Endovascular stent design dictates experimental restenosis and thrombosis. *Circulation*, 91:2995–3001, 1995.

[35] A. Kastrati, J. Mehilli, J. Dirschinger, J. Pache, K. Ulm, H. Schühlen, M. Seyfarth, C. Schmitt, R. Blasini, F. J. Neumann, and A. Schömig. Restenosis after coronary placement of various stent types. *Am. J. Cardiol.*, 87:34–39, 2001.

[36] B. Meier, A. R. Gruentzig, S. B. King, Hollman J. Douglas, J. S., T. Ischinger, Aueron F., and K. Galan. Risk of side branch occlusion during coronary angioplasty. *Am. J. Cardiol.*, 53:10–14, 1984.

[37] B. S. George, R. K. Myler, S. H. Stertzer, D. A. Clark, G. Cote, R. E. Shaw, J. Fishman-Rosen, and M. Murphy. Balloon angioplasty of coronary bifurcation lesions: the kissing balloon technique. *Cathet Cardiovasc Diagn*, 12:124–138, 1986.

[38] T. Lefèvre, Y. Louvard, M. C. Morice, C. Loubeyre, J. F. Piéchaud, and P. Dumas. Stenting of bifurcation lesions: a rational approach. *J Interv Cardiol*, 14:573–585, 2001.

[39] J. Al Suwaidi, W. Yeh, H. A. Cohen, K. M. Detre, D. O. Williams, and D. R. Holmes. Immediate and one-year outcome in patients with coronary bifurcation lesions in the modern era (NHLBI dynamic registry). *Am. J. Cardiol.*, 87:1139–1144, 2001.

[40] T. Yamashita, T. Nishida, M. G. Adamian, C. Briguori, M. Vaghetti, N. Corvaja, R. Albiero, L. Finci, C. Di Mario, J. M. Tobis, and A. Colombo. Bifurcation lesions: two stents versus one stent–immediate and follow-up results. *J. Am. Coll. Cardiol.*, 35:1145–1151, 2000.

[41] A. Colombo, J. W. Moses, M. C. Morice, J. Ludwig, D. R. Holmes, V. Spanos, Y. Louvard, B. Desmedt, C. Di Mario, and M. B. Leon. Randomized study to evaluate sirolimus-eluting stents implanted at coronary bifurcation lesions. *Circulation*, 109:1244–1249, 2004.

[42] I. Iakovou, T. Schmidt, E. Bonizzoni, L. Ge, G. M. Sangiorgi, G. Stankovic, F. Airoldi, A. Chieffo, M. Montorfano, M. Carlino, I. Michev, N. Corvaja, C. Briguori, U. Gerckens, E. Grube, and A. Colombo. Incidence, predictors, and outcome of thrombosis after successful implantation of drug-eluting stents. *JAMA*, 293:2126–2130, 2005.

[43] N. Melikian, F. Airoldi, and C. Di Mario. Coronary bifurcation stenting. Current techniques, outcome and possible future developments. *Minerva Cardioangiol*, 52:365–378, 2004.

[44] T. Lefèvre, Y. Louvard, M. C. Morice, P. Dumas, C. Loubeyre, A. Benslimane, R. K. Premchand, N. Guillard, and J. F. Piéchaud. Stenting of bifurcation lesions: classification, treatments, and results. *Catheter Cardiovasc Interv*, 49:274–283, 2000.

[45] Y. Louvard, T. Lefèvre, and M. C. Morice. Percutaneous coronary intervention for bifurcation coronary disease. *Heart*, 90:713–722, 2004.

[46] B. K. Koo, K. W. Park, H. J. Kang, Y. S. Cho, W. Y. Chung, T. J. Youn, I. H. Chae, D. J. Choi, S. J. Tahk, B. H. Oh, Y. B. Park, and H. S. Kim. Physiological evaluation of the provisional side-branch intervention strategy for bifurcation lesions using fractional flow reserve. *Eur. Heart J.*, 29:726–732, 2008.

[47] D. Carrie, E. Karouny, S. Chouairi, and J. Puel. "T"-shaped stent placement: a technique for the treatment of dissected bifurcation lesions. *Cathet Cardiovasc Diagn*, 37:311–313, 1996.

[48] Y. Kobayashi, A. Colombo, T. Akiyama, B. Reimers, G. Martini, and C. di Mario. Modified "T" stenting: a technique for kissing stents in bifurcational coronary lesion. *Cathet Cardiovasc Diagn*, 43:323–326, 1998.

[49] G. Pavlakis, F. de Man, B. Hamer, P. Doevendans, and P. R. Stella. Registry on a new T technique for bifurcation coronary lesions: the Utrecht-'T'-experience. *EuroInt.*, 3:262–268, 2007.

[50] F. Burzotta, H. C. Gwon, J. Y. Hahn, E. Romagnoli, J. H. Choi, C. Trani, and A. Colombo. Modified T-stenting with intentional protrusion of the side-branch stent within the main vessel stent to ensure ostial coverage and facilitate final kissing balloon: the T-stenting and small protrusion technique (TAP-stenting). Report of bench testing and first clinical Italian-Korean two-centre experience. *Catheter Cardiovasc Interv*, 70:75–82, 2007.

[51] L. Ge, F. Airoldi, I. Iakovou, J. Cosgrave, I. Michev, G. M. Sangiorgi, M. Montorfano, A. Chieffo, M. Carlino, N. Corvaja, and A. Colombo. Clinical and angiographic outcome after implantation of drug-eluting stents in bifurcation lesions with the crush stent technique: importance of final kissing balloon post-dilation. *J. Am. Coll. Cardiol.*, 46:613–620, Aug 2005.

[52] A. R. Galassi, A. Colombo, M. Buchbinder, C. Grasso, S. D. Tomasello, G. P. Ussia, and C. Tamburino. Long-term outcomes of bifurcation lesions after implantation of drug-eluting stents with the "mini-crush technique". *Catheter Cardiovasc Interv*, 69:976–983, Jun 2007.

[53] B. Chevalier, B. Glatt, T. Royer, and P. Guyon. Placement of coronary stents in bifurcation lesions by the "culotte" technique. *Am. J. Cardiol.*, 82:943–949, Oct 1998.

[54] E. Schampaert, S. Fort, A. G. Adelman, and L. Schwartz. The V-stent: a novel technique for coronary bifurcation stenting. *Cathet Cardiovasc Diagn*, 39:320–326, Nov 1996.

[55] S. K. Sharma. Simultaneous kissing drug-eluting stent technique for percutaneous treatment of bifurcation lesions in large-size vessels. *Catheter Cardiovasc Interv*, 65:10–16, 2005.

[56] Y. Kobayashi, A. Colombo, M. Adamian, T. Nishida, I. Moussa, and J. W. Moses. The skirt technique: A stenting technique to treat a lesion immediately proximal to the bifurcation (pseudobifurcation). *Catheter Cardiovasc Interv*, 51:347–351, 2000.

[57] M. Pan, J. S. de Lezo, A. Medina, M. Romero, J. Segura, D. Pavlovic, A. Delgado, S. Ojeda, F. Melián, J. Herrador, I. Ureña, and L. Burgos. Rapamycin-eluting stents for the treatment of bifurcated coronary lesions: a randomized comparison of a simple versus complex strategy. *Am. Heart J.*, 148:857–864, 2004.

[58] T. K. Steigen, M. Maeng, R. Wiseth, A. Erglis, I. Kumsars, I. Narbute, P. Gunnes, J. Mannsverk, O. Meyerdierks, S. Rotevatn, M. Niemelä, K. Kervinen, J. S. Jensen, A. Galløe, K. Nikus, S. Vikman, J. Ravkilde, S. James, J. Aarøe, A. Ylitalo, S. Helqvist, I. Sjögren, P. Thayssen, K. Virtanen, M. Puhakka, J. Airaksinen, J. F. Lassen, and L. Thuesen. Randomized study on simple versus complex stenting of coronary artery bifurcation lesions: the Nordic bifurcation study. *Circulation*, 114:1955–1961, 2006.

[59] M. Ferenc, M. Gick, R. P. Kienzle, H. P. Bestehorn, K. D. Werner, T. Comberg, P. Kuebler, H. J. Büttner, and F. J. Neumann. Randomized trial on routine vs. provisional T-stenting in the treatment of de novo coronary bifurcation lesions. *Eur. Heart J.*, 29:2859–2867, 2008.

[60] M. Pan, J. Suárez de Lezo, A. Medina, M. Romero, E. Hernández, J. Segura, J. R. Castroviejo, D. Pavlovic, F. Melian, A. Ramírez, and J. C. Castillo. Simple and complex stent strategies for bifurcated coronary arterial stenosis involving the side branch origin. *Am. J. Cardiol.*, 83:1320–1325, 1999.

[61] J. Al Suwaidi, P. B. Berger, C. S. Rihal, K. N. Garratt, M. R. Bell, H. H. Ting, J. F. Bresnahan, D. E. Grill, and D. R. Holmes. Immediate and long-term outcome of intracoronary stent implantation for true bifurcation lesions. *J. Am. Coll. Cardiol.*, 35:929–936, 2000.

[62] L. Thuesen, H. Kelbaek, L. Kløvgaard, S. Helqvist, E. Jørgensen, S. Aljabbari, L. R. Krusell, G. V. Jensen, H. E. Bøtker, K. Saunamäki, J. F. Lassen, and A. van Weert. Comparison of sirolimus-eluting and bare metal stents in coronary bifurcation lesions: subgroup analysis of the Stenting Coronary Arteries in Non-Stress/Benestent Disease Trial (SCANDSTENT). *Am. Heart J.*, 152:1140–1145, 2006.

[63] M. Pan, J. Suárez de Lezo, A. Medina, M. Romero, A. Delgado, J. Segura, S. Ojeda, F. Mazuelos, E. Hernandez, F. Melian, D. Pavlovic, F. Esteban, and J. Herrador. Drug-eluting stents for the treatment of bifurcation lesions: a randomized comparison between paclitaxel and sirolimus stents. *Am. Heart J.*, 153:1–7, 2007.

[64] A. Hoye, C. A. G. van Mieghem, A. T. L. Ong, J. Aoki, G. A. Granillo, M. Valgimigli, K. Tsuchida, G. Sianos, E. McFadden, W. J. van der

Giessen, P. J. de Feyter, R. T. van Domburg, and P. W. Serruys. Treatment of de novo bifurcation lesions: comparison of Sirolimus- and Paclitaxel-eluting stents. *EuroInt.*, 1:24–30, 2005.

[65] J. S. Jensen, A. Galløe, J. F. Lassen, A. Erglis, I. Kumsars, T. K. Steigen, R. Wiseth, I. Narbute, P. Gunnes, J. Mannsverk, O. Meyerdierks, S. Rotevatn, M. Niemelä, K. Kervinen, K. Nikus, S. Vikman, J. Ravkilde, S. James, J. Aarøe, A. Ylitalo, S. Helqvist, I. Sjögren, P. Thayssen, K. Virtanen, M. Puhakka, J. Airaksinen, L. Thuesen, L. Thuesen, J. F. Lassen, J. Aarøe, P. Thayssen, H. Kelbaek, S. Helqvist, J. S. Jensen, A. Galløe, S. James, I. Sjögren, T. Steigen, J. Mannsverk, O. Meyerdierks, P. Gunnes, S. Rotevatn, R. Wiseth, K. Nikus, S. Vikman, J. Hartikainen, M. Niemelä, K. Kervinen, K. Virtanen, J. Airaksinen, A. Ylitalo, A. Erglis, I. Kumsars, L. Thuesen, J. F. Lassen, J. Ravkilde, L. R. Krusell, H. E. Bøtker, J. S. Jensen, A. Galløe, J. Aarøe, S. Helqvist, H. Kelbaek, E. Jørgensen, K. Saunamäki, P. Thayssen, K. N. Hansen, I. Sjögren, S. James, F. Schersten, B. Lindvall, G. Olivecrona, L. Hellsten, L. Lundgren, C. M. Pripp, B. Samad, T. Kellerth, T. Steigen, J. Mannsverk, P. Gunnes, O. Meyerdierks, R. Wiseth, S. Rotevatn, K. Endresen, M. Niemelä, K. Kervinen, K. Nikus, S. Vikman, A. Ylitalo, K. Virtanen, M. Puhakka, J. Airaksinen, A. Erglis, I. Kumsars, H. R. Hansen, H. Bargsteen, D. Frydensberg, M. Esbjerg, L. S. Mortensen, H. Højdahl, K. Thygesen, and J. Ravkilde. Safety in simple versus complex stenting of coronary artery bifurcation lesions. The nordic bifurcation study 14-month follow-up results. *EuroIntervention*, 4:229–233, 2008.

[66] A. Latib, A. Colombo, and G. M. Sangiorgi. Bifurcation stenting: current strategies and new devices. *Heart*, 95:495–504, 2009.

[67] M. Stuart. Bifurcation stenting: the next generation. *Windhover's Review of Emerging Medical Ventures*, 11:17–24, 2006.

[68] A. Abizaid, J. de Ribamar Costa, V. J. Alfaro, F. Feres, R. Staico, L. A. Mattos, G. Maldonado, and J. E. Sousa. Bifurcated stents: giving to Caesar what is Caesar's. *EuroInt.*, 2:518–529, 2007.

[69] E. Grube, L. Buellesfeld, F. J. Neumann, S. Verheye, A. Abizaid, D. McClean, R. Mueller, A. Lansky, R. Mehran, R. Costa, U. Gerckens, B. Trauthen, and P. J. Fitzgerald. Six-month clinical and angiographic results of a dedicated drug-eluting stent for the treatment of coronary bifurcation narrowings. *Am. J. Cardiol.*, 99:1691–1697, 2007.

[70] S. Verheye and B. Trauthen. Axxess Biolimus A9 eluting bifurcation stent system. *EuroInt.*, 2:506–508, 2007.

[71] T. Lefèvre, J. Ormiston, G. Guagliumi, H. P. Schultheiss, L. Quilliet, B. Reimers, P. Brunel, W. Wijns, H. J. Buettner, F. Hartmann, S. Veldhof, K. Miquel, X. Su, and W. J. van der Giessen. The Frontier stent registry: safety and feasibility of a novel dedicated stent for the treatment of bifurcation coronary artery lesions. *J. Am. Coll. Cardiol.*, 46:592–598, 2005.

[72] W. van der Giessen. Abbott bifurcation system. Presented at the European Bifurcation Club meeting 2008 in Prague. Available at `http://www.bifurc.net/medtools.php?adm=DIAPORAMA&page=studbibli&thm=`, (accessed 5 May 2009).

[73] Website Abbott Vascular, `http://www.abbottvascular.com/av_dotcom/url/content/en_US/10.10.330.10:10/general_content/Abtdiv_General_Content_0000104.htm`, (accessed 5 May 2009).

[74] B. Garcia Del Blanco, P. Brenot, T. Royer, G. Marti, I. Otaegui, I. Ferreira, R. Ffalu, J. Angel, J. Candell, and D. Garcia-Dorado. Clinical and procedural evaluation of the Nile Croco dedicated stent for bifurcation - six month clinical follow-up results of the Nile Croco registry. *Interventional Cardiology*, 3:46–50, 2008.

[75] J. Ormiston, M. Webster, S. El-Jack, D. McNab, and S. S. Plaumann. The AST petal dedicated bifurcation stent: first-in-human experience. *Catheter Cardiovasc Interv*, 70:335–340, 2007.

[76] M. Paquin. The Sideguard ostium protection device: the next generation in bifurcation stenting. *Cath Lab Digest*, 14, Jul 2006.

[77] R. Mueller. A novel side branch solution to bifurcation disease. Presented at the European Bifurcation Club meeting 2008 in Prague. Available at `http://www.bifurc.net/medtools.php?adm=DIAPORAMA&page=studbibli&thm=`, (accessed 5 May 2009).

[78] R. J. Solar. The Y-Med sideKick stent delivery system for the treament of coronary bifurcation and ostial lesions. Presented at Cardiovascular Revascularization Therapies (CRT) 2007 in Washington DC. Available at `http://www.crtonline.org/flash.aspx?PAGE_ID=4328`, (accessed 5 May 2009).

[79] R. J. Solar. SideKick: a new concept and device for bifurcation stenting. Presented at Cardiovascular Revascularization Therapies (CRT) 2005 in Washington DC. Available at `http://www.crtonline.org/flash.aspx?PAGE_ID=1337`, (accessed 5 May 2009).

[80] J. C. Laborde, N. Borenstein, L. Behr, and S. Ramcharitar. Stentys coronary stent system. *EuroInt.*, 3:162–165, 2007.

[81] S. Verheye, E. Grube, S. Ramcharitar, J. Schofer, B. Witzenbichler, J. Kovac, K. E. Hauptmann, P. Agostoni, M. Wiemer, T. Lefèvre, P. W. Serruys, and R. J. van Geuns. First-in-man (FIM) study of the Stentys bifurcation stent - 30 days results. *EuroInt.*, 4:566–571, 2009.

[82] A. V. Kaplan and H. R. Davis. Tryton side-branch stent. *EuroInt.*, 2, 2006.

[83] A. V. Kaplan, S. Ramcharitar, Y. Louvard, R. Mueller, H. R. Davis, M.-C. Morice, P. W. Serruys, and E. Grube. Tryton I, First-In-Man (FIM) study: acute and 30 day outcome. A preliminary report. *EuroInt.*, 3:54–59, 2007.

[84] Y. Onuma, R. Mueller, S. Ramcharitar, R.-J. van Geuns, Y. Louvard, M.-A. Morel, M.-C. Morice, R. Davis, A. V. Kaplan, T. Lefèvre, E. Grube, and P. W. Serruys. Tryton I, First-In-Man (FIM) study: six month clinical and angiographic outcome, analysis with new quantitative coronary angiography dedicated for bifurcation lesions. *EuroInt.*, 3:546–552, 2008.

[85] T. Lefèvre. Invatec Twin Rail bifurcation stent. On behalf of the Desire investigators. Presented at Transcatheter Cardiovascular Therapeutics (TCT) 2005 in Washington DC. Available at `http://www.tctmd.com/Show.aspx?id=68990`, (accessed 5 May 2009).

[86] S. G. Carlier, W. J. van der Giessen, D. P. Foley, M. J. Kutryk, B. J. Rensing, M. L. Carleton, and P. W. Serruys. Stenting with a true bifurcated stent: acute and mid-term follow-up results. *Catheter Cardiovasc Interv*, 47:361–396, 1999.

[87] J. A. Ormiston, M. W. Webster, P. N. Ruygrok, J. T. Stewart, H. D. White, and D. S. Scott. Stent deformation following simulated side-branch dilatation: a comparison of five stent designs. *Catheter Cardiovasc Interv*, 47:258–264, Jun 1999.

[88] J. A. Ormiston, E. Currie, M. W. Webster, P. Kay, P. N. Ruygrok, J. T. Stewart, R. C. Padgett, and M. J. Panther. Drug-eluting stents for coronary bifurcations: insights into the crush technique. *Catheter Cardiovasc Interv*, 63:332–336, 2004.

[89] J. A. Ormiston, M. W. Webster, S. El Jack, P. N. Ruygrok, J. T. Stewart, D. Scott, E. Currie, M. J. Panther, B. Shaw, and B. O'Shaughnessy. Drug-eluting stents for coronary bifurcations: bench testing of provisional side-branch strategies. *Catheter Cardiovasc Interv*, 67:49–55, Jan 2006.

[90] T. Kinoshita, Y. Kobayashi, J. De Gregorio, M. Nameki, N. Kuroda, Y. Yamamoto, A. Miyazaki, and Y. Masuda. Difference in security

of stent jail between Palmaz-Schatz, NIR, and Multi-Link stents: the effect of balloon inflation through stent struts. *Catheter Cardiovasc Interv*, 48:230–234, 1999.

[91] Y. Murasato. Impact of three-dimensional characteristics of the left main coronary artery bifurcation on outcome of crush stenting. *Catheter Cardiovasc Interv*, 69:248–256, Feb 2007.

[92] Y. Murasato, M. Horiuchi, and Y. Otsuji. Three-dimensional modeling of double-stent techniques at the left main coronary artery bifurcation using micro-focus X-ray computed tomography. *Catheter Cardiovasc Interv*, 70:211–220, 2007.

[93] M. Perry, S. Oktay, and J. C. Muskivitch. Finite element analysis and fatigue of stents. *Min Invas Ther and Allied Technol*, 11(4):165–171, 2002.

[94] M. De Beule. *Finite element stent design.* PhD thesis, Ghent University, Belgium, 2008.

[95] W. Wu, D. Z. Yang, Y. Y. Huang, M. Qi, and W. Q. Wang. Topology optimization of a novel stent platform with drug reservoirs. *Med Eng Phys*, 30:1177–1185, 2008.

[96] L. H. Timmins, C. A. Meyer, M. R. Moreno, and J. E. Moore. Effects of stent design and atherosclerotic plaque composition on arterial wall biomechanics. *J. Endovasc. Ther.*, 15:643–654, 2008.

[97] F. J. Gijsen, F. Migliavacca, S. Schievano, L. Socci, L. Petrini, A. Thury, J. J. Wentzel, A. F. van der Steen, P. W. Serruys, and G. Dubini. Simulation of stent deployment in a realistic human coronary artery. *Biomed Eng Online*, 7:23, 2008.

[98] C. J. Slager, J. J. Wentzel, J. C. Schuurbiers, J. A. Oomen, J. Kloet, R. Krams, C. von Birgelen, W. J. van der Giessen, P. W. Serruys, and P. J. de Feyter. True 3-dimensional reconstruction of coronary arteries in patients by fusion of angiography and IVUS (ANGUS) and its quantitative validation. *Circulation*, 102:511–516, 2000.

[99] H. Zahedmanesh and C. Lally. Determination of the influence of stent strut thickness using the finite element method: implications for vascular injury and in-stent restenosis. *Med Biol Eng Comput*, 47:385–393, 2009.

[100] A. Kastrati, J. Mehilli, J. Dirschinger, F. Dotzer, H. Schuhlen, F. J. Neumann, M. Fleckenstein, C. Pfafferott, M. Seyfarth, and A. Schomig. Intracoronary stenting and angiographic results: strut thickness effect on restenosis outcome (ISAR-STEREO) trial. *Circulation*, 103:2816–2821, 2001.

[101] D. E. Kiousis, A. Wulff, and G. A. Holzapfel. Experimental studies and numerical analysis of the inflation and interaction of vascular balloon catheter-stent systems. *Ann. Biomed. Eng.*, 37:315–330, 2009.

[102] D. Gastaldi, S. Morlacchi, R. Nichetti, C. Capelli, G. Dubini, L. Petrini, and F. Migliavacca. Modelling of the provisional side-branch stenting approach for the treatment of atherosclerotic coronary bifurcations: effects of stent positioning. *Biomech Model Mechanobiol*, 2010.

[103] A. Betriu, M. Masotti, A. Serra, J. Alonso, F. Fernández-Avilés, F. Gimeno, T. Colman, J. Zueco, J. L. Delcan, E. García, and J. Calabuig. Randomized comparison of coronary stent implantation and balloon angioplasty in the treatment of de novo coronary artery lesions (START): a four-year follow-up. *J. Am. Coll. Cardiol.*, 34:1498–1506, 1999.

[104] P. W. Serruys, M. J. Kutryk, and A. T. Ong. Coronary-artery stents. *N. Engl. J. Med.*, 354:483–495, 2006.

[105] M. J. Eisenberg and K. J. Konnyu. Review of randomized clinical trials of drug-eluting stents for the prevention of in-stent restenosis. *Am. J. Cardiol.*, 98:375–382, Aug 2006.

[106] M. Joner, A. V. Finn, A. Farb, E. K. Mont, F. D. Kolodgie, E. Ladich, R. Kutys, K. Skorija, H. K. Gold, and R. Virmani. Pathology of drug-eluting stents in humans: delayed healing and late thrombotic risk. *J. Am. Coll. Cardiol.*, 48:193–202, 2006.

[107] A. Farb, G. Sangiorgi, A. J. Carter, V. M. Walley, W. D. Edwards, R. S. Schwartz, and R. Virmani. Pathology of acute and chronic coronary stenting in humans. *Circulation*, 99:44–52, 1999.

[108] C. Rogers, D. Y. Tseng, J. C. Squire, and E. R. Edelman. Balloon-artery interactions during stent placement: a finite element analysis approach to pressure, compliance, and stent design as contributors to vascular injury. *Circ. Res.*, 84:378–383, 1999.

[109] Y. Ikari, K. Hara, T. Tamura, F. Saeki, and T. Yamaguchi. Luminal loss and site of restenosis after Palmaz-Schatz coronary stent implantation. *Am. J. Cardiol.*, 76:117–120, 1995.

[110] C. Dumoulin and B. Cochelin. Mechanical behaviour modelling of balloon-expandable stents. *J Biomech*, 33:1461–1470, Nov 2000.

[111] L. B. Tan, D. C. Webb, K. Kormi, and S. T. Al-Hassani. A method for investigating the mechanical properties of intracoronary stents using finite element numerical simulation. *Int. J. Cardiol.*, 78:51–67, 2001.

[112] C. Lally, F. Dolan, and P. J. Prendergast. Cardiovascular stent design and vessel stresses: a finite element analysis. *J Biomech*, 38:1574–1581, 2005.

[113] G. A. Holzapfel and R. W. Ogden, editors. *Mechanics of Biological Tissue*. Springer-Verlag, Heidelberg, 2006.

[114] F. Auricchio, M. Di Loreto, and E. Sacco. Finite element analysis of a stenotic artery revascularization through a stent insertion. *Computer Methods in Biomechanics and Biomedical Engineering*, 4:249–263, 2001.

[115] F. Migliavacca, L. Petrini, V. Montanari, I. Quagliana, F. Auricchio, and G. Dubini. A predictive study of the mechanical behaviour of coronary stents by computer modelling. *Med Eng Phys*, 27:13–18, 2005.

[116] M. De Beule, R. Van Impe, B. Verhegghe, P. Segers, and P. Verdonck. Finite element analysis and stent design: Reduction of dogboning. *Technol Health Care*, 14:233–241, 2006.

[117] W. Q. Wang, D. K. Liang, D. Z. Yang, and M. Qi. Analysis of the transient expansion behavior and design optimization of coronary stents by finite element method. *J Biomech*, 39:21–32, 2006.

[118] M. De Beule, P. Mortier, R. Van Impe, B. Verhegghe, P. Segers, and P. Verdonck. Plasticity in the Mechanical Behaviour of Cardiovascular Stents during Stent Preparation (crimping) and Placement (expansion). *Key Engineering Materials*, 340-341:847–852, 2007.

[119] Centre for X-ray Tomography from Ghent University. `www.ugct.ugent.be`.

[120] B. P. Murphy, P. Savage, P. E. McHugh, and D. F. Quinn. The stress-strain behavior of coronary stent struts is size dependent. *Ann Biomed Eng*, 31:686–691, Jun 2003.

[121] M. De Beule, P. Mortier, J. Belis, R. Van Impe, B. Verhegghe, and P. Verdonck. Plasticity as a lifesaver in the Design of Cardiovascular Stents. *Key Engineering Materials*, 340-341:841–846, 2007.

[122] S. Timoshenko, editor. *Strength of Materials (Part I: Elementary Theory and Problems)*. D. Van Nostrand, New York, 1955.

[123] D. Laroche, S. Delorme, T. Anderson, and R. DiRaddo. Computer prediction of friction in balloon angioplasty and stent implantation. In M. Harders and G. Székely, editors, *Biomedical Simulation*, pages 1–8. Springer, 2008.

[124] J. de Ribamar Costa, G. S. Mintz, S. G. Carlier, R. A. Costa, K. Fujii, K. Sano, M. Kimura, J. Lui, G. Weisz, I. Moussa, G. Dangas, R. Mehran, A. J. Lansky, E. M. Kreps, M. Collins, G. W. Stone, J. W. Moses, and M. B. Leon. Intravascular ultrasonic assessment of stent diameters derived from manufacturer's compliance charts. *Am. J. Cardiol.*, 96:74–78, 2005.

[125] G. J. Hall and E. P. Kasper. Comparison of element technologies for modeling stent expansion. *J Biomech Eng*, 128:751–756, 2006.

[126] M. De Beule, P. Mortier, S. G. Carlier, B. Verhegghe, R. Van Impe, and P. Verdonck. Realistic finite element-based stent design: the impact of balloon folding. *J. Biomech.*, 41:383–389, 2008.

[127] P. Mortier, M. De Beule, S. G. Carlier, R. Van Impe, B. Verhegghe, and P. Verdonck. Numerical study of the uniformity of balloon-expandable stent deployment. *J. Biomech. Eng.*, 130:021018, 2008.

[128] A. G. Radaelli, L. Augsburger, J. R. Cebral, M. Ohta, D. A. Rüfenacht, R. Balossino, G. Benndorf, D. R. Hose, A. Marzo, R. Metcalfe, P. Mortier, F. Mut, P. Reymond, L. Socci, B. Verhegghe, and A. F. Frangi. Reproducibility of haemodynamical simulations in a subject-specific stented aneurysm model–a report on the Virtual Intracranial Stenting Challenge 2007. *J Biomech*, 41:2069–2081, 2008.

[129] B. C. Masschaele, V. Cnudde, M. Dierick, P. Jacobs, L. Van Hoorebeke, and L. Vlassenbroeck. UGCT: new X-ray radiography and tomography facility. *Nucl Instrum Methods A*, 580:266–269, 2007.

[130] pyFormex. `www.pyformex.org`.

[131] L. Antiga. *Patient-specific modeling of geometry and blood flow in large arteries.* PhD thesis, Politecnico Di Milano, Italy, 2002.

[132] D. E. Kiousis, T. C. Gasser, and G. A. Holzapfel. A numerical model to study the interaction of vascular stents with human atherosclerotic lesions. *Ann. Biomed. Eng.*, 35:1857–1869, 2007.

[133] F. J. Harewood and P. E. McHugh. Modeling of size dependent failure in cardiovascular stent struts under tension and bending. *Ann Biomed Eng*, 35:1539–1553, 2007.

[134] W. Wu, M. Qi, X. P. Liu, D. Z. Yang, and W. Q. Wang. Delivery and release of nitinol stent in carotid artery and their interactions: a finite element analysis. *J Biomech*, 40:3034–3040, 2007.

[135] P. Poncin and J. Proft. Stent tubing: understanding the desired attributes. *Proceedings of the Materials and Processes for Medical Devices Conference, Anaheim, USA*, 2003.

[136] P. J. Prendergast, C. Lally, S. Daly, A. J. Reid, T. C. Lee, D. Quinn, and F. Dolan. Analysis of prolapse in cardiovascular stents: a constitutive equation for vascular tissue and finite-element modelling. *J Biomech Eng*, 125:692–699, Oct 2003.

[137] D. Stoeckel, S. Bonsignore, and S. Duda. A survey of stent designs. *Minim Invasive Ther Allied Technol*, 11:137–147, 2002.

[138] J. W. Moses, M. B. Leon, J. J. Popma, P. J. Fitzgerald, D. R. Holmes, C. O'Shaughnessy, R. P. Caputo, D. J. Kereiakes, D. O. Williams, P. S. Teirstein, J. L. Jaeger, and R. E. Kuntz. Sirolimus-eluting stents versus standard stents in patients with stenosis in a native coronary artery. *N. Engl. J. Med.*, 349:1315–1323, 2003.

[139] Philips Medical Systems Nederland B.V., Best, The Netherlands. `http://www.healthcare.philips.com`.

[140] R. McNeel & Associates. *Rhinoceros – NURBS modeling for Windows, Version 4.0 User's Guide.* Seattle, Washington, 2008.

[141] Fluent Inc. *Gambit Version 2.3 User's Guide.* Lebanon, New Hampshire, 2006.

[142] G. A. Holzapfel and H. W. Weizsäcker. Biomechanical behavior of the arterial wall and its numerical characterization. *Comp. Biol. Med.*, 28:377–392, 1998.

[143] G. A. Holzapfel. *Nonlinear Solid Mechanics. A Continuum Approach for Engineering.* John Wiley & Sons, Chichester, 2000.

[144] G. A. Holzapfel and R. W. Ogden. On planar biaxial tests for anisotropic nonlinearly elasitc solids. A continuum mechanical framework. *Math. Mech. Solids*, doi:10.1177/1081286507084411, 2008.

[145] D. E. Kiousis, S. F. Rubinigg, M. Auer, and G. A. Holzapfel. A methodology to analyze changes in lipid core and calcification onto fibrous cap vulnerability: The human atherosclerotic carotid bifurcation as an illustratory example. *J. Biomech. Eng.*, 131:121002, 2009.

[146] A. L. McKelvey and R. O. Ritchie. Fatigue-crack growth behavior in the superelastic and shape-memory alloy nitinol. *Metall. Mater. Trans. A*, 32A:731–743, 2001.

[147] G. A. Holzapfel, M. Stadler, and C. A. Schulze-Bauer. A layer-specific three-dimensional model for the simulation of balloon angioplasty using magnetic resonance imaging and mechanical testing. *Ann. Biomed. Eng.*, 30:753–767, 2002.

[148] W. Wu, W. Q. Wang, D. Z. Yang, and M. Qi. Stent expansion in curved vessel and their interactions: a finite element analysis. *J. Biomech.*, 40:2580–2585, 2007.

[149] R. Rieu, P. Barragan, C. Masson, J. Fuseri, V. Garitey, M. Silvestri, P. Roquebert, and J. Sainsous. Radial force of coronary stents: a comparative analysis. *Catheter. Cardiovasc. Interv.*, 46:380–391, 1999.

[150] S. P. Gorman, D. S. Jones, M. C. Bonner, M. Akay, and P. F. Keane. Mechanical performance of polyurethane ureteral stents in vitro and ex vivo. *Biomaterials*, 18:1379–1383, 1997.

[151] R. Liao, N. E. Green, S. Y. Chen, J. C. Messenger, A. R. Hansgen, B. M. Groves, and J. D. Carroll. Three-dimensional analysis of in vivo coronary stent–coronary artery interactions. *Int. J. Cardiovasc. Imaging.*, 20:305–313, 2004.

[152] J. J. Wentzel, D. M. Whelan, W. J. van der Giessen, H. M. van Beusekom, I. Andhyiswara, P. W. Serruys, C. J. Slager, and R. Krams. Coronary stent implantation changes 3-D vessel geometry and 3-D shear stress distribution. *J. Biomech.*, 33:1287–1295, 2000.

[153] M. Gyöngyösi, P. Yang, A. Khorsand, and D. Glogar. Longitudinal straightening effect of stents is an additional predictor for major adverse cardiac events. Austrian Wiktor Stent Study Group and European Paragon Stent Investigators. *J. Am. Coll. Cardiol.*, 35:1580–1589, 2000.

[154] V. Deplano, C. Bertolotti, and P. Barragan. Three-dimensional numerical simulations of physiological flows in a stented coronary bifurcation. *Med. Biol. Eng. Comput.*, 42:650–659, 2004.

[155] P. Mortier, M. De Beule, D. Van Loo, B. Verhegghe, and P. Verdonck. Finite element analysis of side branch access during bifurcation stenting. *Med. Eng. Phys.*, 31:434–440, 2009.

[156] G. A. Holzapfel and R. W. Ogden, editors. *Biomechanical Modelling at the Molecular, Cellular and Tissue Levels.* Springer-Verlag, Wien – New York, 2009.

[157] G. A. Holzapfel, M. Stadler, and T. C. Gasser. Changes in the mechanical environment of stenotic arteries during interaction with stents: Computational assessment of parametric stent design. *J. Biomech. Eng.*, 127:166–180, 2005.

[158] S. S. El Jack, S. R. Dixon, C. L. Grines, and W. W. O'Neill. Bifurcation stenting: unnecessary challenge or a last frontier in intervention. *J. Interven. Cardiol.*, 19:S27–S39, 2006.

[159] L. Vlassenbroeck, M. Dierick, B. Masschaele, V. Cnudde, L. Van Hoorebeke, and P. Jacobs. Software tools for quantification of X-ray microtomography. *Nucl Instrum Methods A*, 580:442–445, 2007.

[160] P. Gheeraert, M. De Buyzere, and Y. Taeymans. A user-friendly and fast online system to optimize camera positions for angioplasty of bifurcation lesions. *Proceedings of Transcatheter Cardiovascular Therapeutics, September 15-19, Washington DC, USA*, 2003.

[161] M. Pan, J. S. de Lezo, A. Medina, M. Romero, J. Segura, A. Ramirez, D. Pavlovic, E. Hernandez, S. Ojeda, and C. Adamuz. A stepwize strategy for the stent treatment of bifurcation lesions. *Catheter. Cardiovasc. Interv.*, 55:50–57, 2002.

[162] D. Scheinert, S. Scheinert, J. Sax, C. Piorkowski, S. Bräunlich, M. Ulrich, G. Biamino, and A. Schmidt. Prevalence and clinical impact of stent fractures after femoropopliteal stenting. *J. Am. Coll. Cardiol.*, 45:312–315, 2005.

[163] G. Stankovic, O. Darremont, M. Ferenc, D. Hildick-Smith, J. F. Lassen, Y. Louvard, R. Albiero, M. Pan, and T. Lefèvre. Percutaneous coronary intervention for bifurcation lesions: 2008 consensus document from the fourth meeting of the European Bifurcation Club. *EuroInt.*, 5:39–49, 2009.

Publications

Publications in international journals

First author

- P. Mortier, M. De Beule, S. G. Carlier, R. Van Impe, B. Verhegghe, and P. Verdonck. Numerical study of the uniformity of balloon-expandable stent deployment. *Journal of Biomechanical Engineering*, 130(021018):1-7, 2008.

- P. Mortier, M. De Beule, D. Van Loo, B. Masschaele, P. Verdonck, and B. Verhegghe. Automated generation of a finite element stent model. *Medical and Biological Engineering and Computing*, 46:1169-1173, 2008.

- P. Mortier, D. Van Loo, M. De Beule, P. Segers, P. Verdonck, and B. Verhegghe. Comparison of drug-eluting stent cell size using micro-CT: important data for bifurcation stent selection. *EuroIntervention*, 4:391-396, 2008.

- P. Mortier, M. De Beule, D. Van Loo, P. Verdonck, and B. Verhegghe. Finite element analysis of side branch access during bifurcation stenting. *Medical Engineering & Physics*, 31:434-440, 2009.

- P. Mortier, G. A. Holzapfel, M. De Beule, D. Van Loo, Y. Taeymans, P. Segers, P. Verdonck, and B. Verhegghe. A novel simulation strategy for stent insertion and deployment in curved coronary bifurcations: comparison of three drug-eluting stents. *Annals of Biomedical Engineering*, 38:88-99, 2010.

- P. Mortier, and P. Verdonck. Stent design matters: insights from virtual bench testing. *Expert Review of Cardiovascular Therapy*, submitted.

Co-author

- M. De Beule, P. Mortier, J. Belis, R. Van Impe, B. Verhegghe, and P. Verdonck. Plasticity as a lifesaver in the design of cardiovascular stents. *Key Engineering Materials*, 340-341:841-846, 2007.
- M. De Beule, P. Mortier, R. Van Impe, B. Verhegghe, P. Segers, and P. Verdonck. Plasticity in the mechanical behavior of cardiovascular stents during stent preparation (crimping) and placement (expansion). *Key Engineering Materials*, 340-341:847-852, 2007.
- M. De Beule, P. Mortier, S. G. Carlier, B. Verhegghe, R. Van Impe, and P. Verdonck. Realistic finite element-based stent design: The impact of balloon folding. *Journal of Biomechanics*, 41:383-389, 2008.
- A. G. Radaelli, L. Augsburger, J. R. Cebral, M. Ohta, D. A. Rüfenacht, R. Balossino, G. Benndorf, D. R. Hose, A. Marzo, R. Metcalfe, P. Mortier, F. Mut, P. Reymond, L. Socci, B. Verhegghe, and A. F. Frangi. Reproducibility of haemodynamical simulations in a subject-specific stented aneurysm model - A report on the Virtual Intracranial Stenting Challenge 2007. *Journal of Biomechanics*, 41:2069-2081, 2008.
- M. De Beule, S. Van Cauter, P. Mortier, D. Van Loo, R. Van Impe, P. Verdonck, and B. Verhegghe. Virtual optimization of self-expandable braided wire stents. *Medical Engineering & Physics*, 31:448-453, 2009.
- M. Conti, M. De Beule, P. Mortier, D. Van Loo, P. Verdonck, F. Vermassen, P. Segers, F. Auricchio, and B. Verhegghe. Nitinol embolic protection filters: Design investigation by finite element analysis. *Journal of Materials Engineering and Performance*, 18:787-792, 2009.
- G. De Santis, P. Mortier, M. De Beule, P. Segers, P. Verdonck, and B. Verhegghe. Patient specific computational fluid dynamics: Structured mesh generation from coronary angiography. *Medical and Biological Engineering and Computing*, submitted.

Abbreviations and symbols

Abbreviations

3D	three-dimensional
AS	asymmetry coefficient
AST	advanced stent technologies
BMS	bare metal stent
C3D8R	three-dimensional 8-node brick reduced integration element
CA	coronary angiography
CAD	computer aided design
CAE	computer aided engineering
CoCr	cobalt-chromium
CS	Cypher Select design variant
CT	computed tomography
DB	dogboning coefficient
DES	drug eluting stent
DMB	distal main branch
FEA	finite element analysis
FFR	fractional flow reserve
IVUS	intravascular ultrasound
L50	large bifurcation model with a 50 degrees bifurcation angle
L80	large bifurcation model with a 80 degrees bifurcation angle
LAD	left anterior descending artery
LCA	left coronary artery
LCX	left circumflex artery
LDL	low density lipoprotein
LM	left main artery
M3D3	3-node triangular membrane element

M3D4	4-node quadrilateral membrane element
M3D4R	4-node quadrilateral membrane reduced integration element
M50	medium sized bifurcation model with a 50 degrees bifurcation angle
M80	medium sized bifurcation model with a 80 degrees bifurcation angle
MACE	major adverse cardiac events
MADS	main, across, distal, side
MB	main branch
MC	medical center
MSP	maximal strut protrusion
NURBS	non-uniform rational B-splines
OC	overdilatation coefficient
PCA	projected cell area
PMB	proximal main branch
QCA	quantitative coronary analysis
R3D4	4-node bilinear rigid quadrilateral element
RCA	right coronary artery
REF	reference simulation
S50	small bifurcation model with a 50 degrees bifurcation angle
S80	small bifurcation model with a 80 degrees bifurcation angle
SB	side branch
SKS	simultaneous kissing stents
SS316L	316-L stainless steel
TAP	T-stenting and small protrusion technique
VUMAT	user-defined material in ABAQUS/Explicit

Symbols

$\mathbf{C}$	right Cauchy-Green tensor
$\overline{\mathbf{C}}$	modified right Cauchy-Green tensor
D	diameter
E	Young's modulus
$\bar{I}$	invariant
J	volume ratio
k	material parameter
L	length
$\mathbf{M}$	unit vector indicating collagen fiber direction
$\mathbf{M'}$	unit vector indicating collagen fiber direction

$\mathbf{n}$	local material orientation
p	pressure
R	radius
w	width

Greek Symbols

α	bifurcation angle or angle between the collagen fiber reinforcement and the cirumferential direction
κ	penalty parameter
μ	micro or material parameter
$\overline{\Psi}$	volume preserving part of the strain energy function
ρ	material parameter

Subscripts

$aniso$	anisotropic
DMB	distal main branch
end	modified end rings
f	final
i	intermediate
iso	isotropic
max	maximum
min	minimum
o	original
pre	prior to a certain operation
$post$	after a certain operation
PMB	proximal main branch
SB	side branch
$thin$	reduced strut thickness

Units

atm	atmosphere
bar	bar
Fr	french
GPa	gigapascal
hz	Hertz

inch	inch
kPa	kilopascal
μm	micrometer
m	meter
min	minute
mm	millimeter
MPa	megapascal
N	Newton
Pa	Pascal
sec	second
V	Volt
W	Watt